UNIVERSIDAD DEL PAIS VASCO
EUSKAL HERRIKO UNIBERTSITATEA
Departamento de Física de Materiales
Materialen Fisika Saila

---

# Modelization of plasmonic nanoantennas for optical microscopy and surface enhanced spectroscopy

**Aitzol García-Etxarri**

**Work developed under the supervision of**

**Javier Aizpurua and Pedro Miguel Echenique**

---

Phd Thesis

---

# CONTENTS

**1 Introduction** **5**

1.1 Antennas: a historical overview . . . . . 6

1.2 The most elementary antenna: the electric dipole . . . . . 9

1.2.1 Radiation regions . . . . . 12

1.2.2 Dipolar emitters . . . . . 16

1.3 The electromagnetic spectrum . . . . . 17

1.4 Optical antennas: factors influencing the response . . . . . 20

1.4.1 Plasmons . . . . . 21

1.4.2 The role of the skin depth . . . . . 27

1.5 Applications of optical antennas . . . . . 34

**2 Resonant plasmonic and vibrational coupling in a tailored nanoantenna for infrared detection** **37**

2.1 Antenna design . . . . . 41

2.2 Antenna-vibrational coupling . . . . . 43

2.3 Experimental evidence: . . . . . 47

**3 Plasmonic concave/convex surfaces for field-enhancement: the plasmonic indented nanocone** **53**

3.1 Ingredients of the field enhancement . . . . . 54

3.2 Plasmonic indented nanocone . . . . . 59

**4 Near-field imaging of plasmonic antennas** **67**

4.1 Vectorial mapping of the plasmonic near-field produced by nanoantennas 73

4.2 "Probe-sample" interaction in scattering-type near-field optical microscopy 80

4.2.1 Experimental evidence of interacting regimes . . . . . 80

4.2.2 Weak and strong coupling regimes . . . . . 81

4.2.3 Spectral analysis . . . . . 85

4.2.4 Simple model: dipole-dipole interaction . . . . . 87

**5 Control of the optical response of nanoantennas** **89**

5.1 Probe assisted opto-mechanical control of the optical response in plasmonic nanoantennas . . . . . 90

5.2 Controlling the response of plasmonic nanoantennas through gap-loading 92

5.2.1 Control of the far-field response through gap loading . . . . . 94

5.2.2 Connection with circuit theory . . . . . 94

5.2.3 Controlling the near-field response of gap antennas . . . . . 97

**A The Boundary Element Method (BEM)** **105**

**Bibliography** **110**

# CHAPTER 1

# INTRODUCTION

Electromagnetic antennas are defined by Constantine A. Balanis as "system components that are designed to radiate or receive electromagnetic waves [1]". These devices have played a key enabling role in the development of a variety of revolutionary applications like cellular phones, radar systems, etc. State of the art antenna based commercial communication systems make use of electromagnetic waves that range from ultra-low frequencies to the tera Hertz region of the spectrum. Electromagnetic fields at optical frequencies, have been traditionally controlled by means of geometrical optical components such as lenses, mirrors, fiber optics, etc. These system components base their working principles on the wave nature of light and hence they cannot manipulate electromagnetic fields at sub-wavelength scale.

Recent research advances at the field of nanophotonics have generated an important interest in optical antennas. These structures, recently defined by L. Novotny as "devices designed to efficiently convert free-propagating optical radiation to localized energy, and vice versa" [2], take advantage of their characteristic sizes and the nature of their associated electromagnetic excitations (surface plasmons), and offer

the possibility of overcoming the diffraction limit and thus controlling the light at the nanoscale.

This sub-wavelength, nanoscale, control of optical fields, is leading to new technological applications such as field enhanced spectroscopies [3,4] sub-wavelength near-field optical microscopy, boosting the efficiency of photochemical or photophysical detectors, plasmonic circutry and new medical diagnosis and therapy tools, among others. Because of the working principle similarities between optical antennas and radio frequency antennas, several outgoing studies attempt to extend and adapt the established radio wave antenna and micro wave antenna theories to the optical frequency regime [5–8]. Within this spirit of connecting both frequency ranges, let me introduce a brief historical overview of antennas and radiation based systems before exploring the working principles of optical antennas

## 1.1 Antennas: a historical overview

The history of antennas can be traced back to the unification of electricity and magnetism by James Clerk Maxwell in 1873, but this unification would had not been possible without the previous independent discoveries of the laws governing the electricity and magnetism and their relationships.

In 1750, Benjamin Franklin proposed his famous kite experiment to prove that lightning is electricity. This experiment was lately conducted on 1752 first by Thomas-Franois Dalibard and later by Benjamin Franklin himself. With this experiment he determined the existence of positive and negative electric charges and stablished the principle of conservation of charge. 30 years later, in 1780, Charles Agustin de Coulomb invented the torsion balance and measured electric charges for the first time. In 1800 when Alessandro Volta invented the battery. This instrument permitted Hans Chris-

tian Oersted in 1819 to establish a current on a wire and discover that a magnetic needle is deflected when an electric current varies in a nearby wire. With this experiment he demonstrated the first connection between electricity and magnetism. Before this discovery electricity and magnetism were considered two independent phenomena. In 1820, André Marie Amperè inspired by Oersted's observation, designed a set of experiments with which he extended these observations and established the theoretical relationship between electric current-flow and magnetism (Ampere's law).

Some years later in 1831 Michael Faraday found that a time varying magnetic field could also induce an electric current, establishing then the inverse relationship between magnetism and electricity (Faraday's law).

All these discoveries permitted James Clerk Maxwell to establish the interdependence of the electricity and the magnetism that he published in the first unified theory of electromagnetism in 1873 in his book "A Treatise on Electricity and Magnetism" [9].

Maxwell's equations in a differential form (SI units) are expressed like this:

$$\nabla \cdot D = \rho \tag{1.1}$$

$$\nabla \cdot H = 0 \tag{1.2}$$

$$\nabla \times E = -\mu \partial H / \partial t \tag{1.3}$$

$$\nabla \times H = J + \partial D / \partial t \tag{1.4}$$

being $E$ the electric field, $B$ the magnetic field, $D = \varepsilon E$ the displacement vector, $H = B/\mu$, $\varepsilon$ the permittivity of the medium and $\mu$ the magnetic susceptibility of the medium. $\rho$ is the free charge, and $J$ the free current.

Applying vector identities to maxwell equations, it is possible to reach the following relationship for the electric and magnetic fields in vacuum:

$$\nabla^2 E = \mu_0 \varepsilon_0 \frac{\partial^2 E}{\partial t^2} \tag{1.5}$$

$$\nabla^2 B = \mu_0 \varepsilon_0 \frac{\partial^2 B}{\partial t^2} \tag{1.6}$$

These two equations are equivalent to the differential equation that describes the propagation of a wave:

$$\nabla^2 f = \frac{1}{v} \frac{\partial^2 f}{\partial t^2} \tag{1.7}$$

being $v$ the propagation velocity of the wave.

By comparison,

$$v = \frac{1}{\sqrt{\mu_0 \varepsilon_0}} = c \tag{1.8}$$

where we can define $c$ as the speed of light.

On the one hand, Maxwell's equations completed the connection between electricity and magnetism. On the other hand, they showed that electric and magnetic fields can adopt the form of propagating waves. Furthermore, as the propagation speed of these waves resulted to be the speed of light, the equations proved the electromagnetic wave nature of light.

In spite the tremendous importance of these equations and their consequences, there was a great skepticismto accept them until professor Heinrich Rudolph Hertz demonstrated the first wireless electromagnetic system in 1886. His experiment consisted in a very primitive RLC circuit that, when discharged, produced an oscillatory current that circulated along a wire of a length comparable to the wavelength of the current. The main challenge of the system was to discharge the RLC circuit in order to launch

the oscillating current. Hertz solved this problem by feeding the circuit with a high voltage generator, and connecting its output to a set of two spheres placed very close to each other. When the voltage difference on the spheres reached a critical value, a spark was created between them, discharging the circuit and producing the oscillatory current. That current, when circulating along the wire, radiated an electromagnetic wave. In order to detect this radiation, Hertz employed a loop antenna as the receiving system. He set another couple of closely spaced spheres in this loop. When an incoming electromagnetic wave induced a current on the antenna, the spheres got charged and an observable spark was generated on the gap. Thanks to all this advancements, Gugliermo Marconi, in 1901, was able to perform the first transatlantic transmission from England to Canada.

Since that moment on, wireless communications evolved rapidly, developing similar approaches and ideas for higher frequencies and adapting their capabilities to the specific necessities of different applications. During the last century, specific design rules have been adopted for antenna design. Nowadays, antennas design constitutes an entire area of study within electrical engineering. In order to introduce some basic concepts in the field, the next section will be dedicated to the study of the most simple radiator element, the elementary electric dipole.

## 1.2 The most elementary antenna: the electric dipole

An elementary oscillating electric dipole is a set of two closely spaced positive and negative electric charges that oscillate in time at a certain frequency $\omega$. We assume a harmonic dependence of the oscillation of the potentials and fields $\approx e^{i\omega t}$, therefore, the vector potential associated to such a system for a concrete frequency $\omega$ in the frequency

domain can be expressed as [10]:

$$\mathbf{A}(r) = -ik\frac{e^{ik_\mu r}}{r}\mathbf{p} \tag{1.9}$$

being k the magnitude of the wavevector in vacuum, $k_\mu$ the magnitude of the wavevector on the embedding medium $\mu$, $r$ the distance between the position of the dipole and the evaluation point and $\mathbf{p}$ the dipole moment of the dipole.

From now on all the expressions are refereed to a particular frequency $\omega$.

The scalar potential $\phi$ can be deduced from the vector potential $\mathbf{A}$ through,

$$\phi(r) = \frac{1}{ik\varepsilon\mu}\nabla\mathbf{A}(r) \tag{1.10}$$

being $\varepsilon$ and $\mu$ the permittivity and the permeability of the embedding medium.

The electric fields induced by an electric point dipole can be now calculated from the potentials as:

$$\mathbf{E}(r) = ik\mathbf{A}(r) - \nabla\phi \tag{1.11}$$

On the other hand, the magnetic field induced by the same dipole can be calculated as,

$$\mathbf{H}(r) = \frac{1}{\mu}\nabla\times\mathbf{A} \tag{1.12}$$

From these expressions we can obtain the value of the electric and magnetic fields:

$$\mathbf{E}(r) = \frac{1}{\varepsilon}\frac{e^{ik_\mu r}}{r^3}\left[(k_\mu^2 r^2 + ik_\mu r - 1)\mathbf{p} + (\mathbf{r}\cdot\mathbf{p})\frac{-k_\mu^2 r^2 - 3ik_\mu r + 3}{r^2}\mathbf{r}\right] \tag{1.13}$$

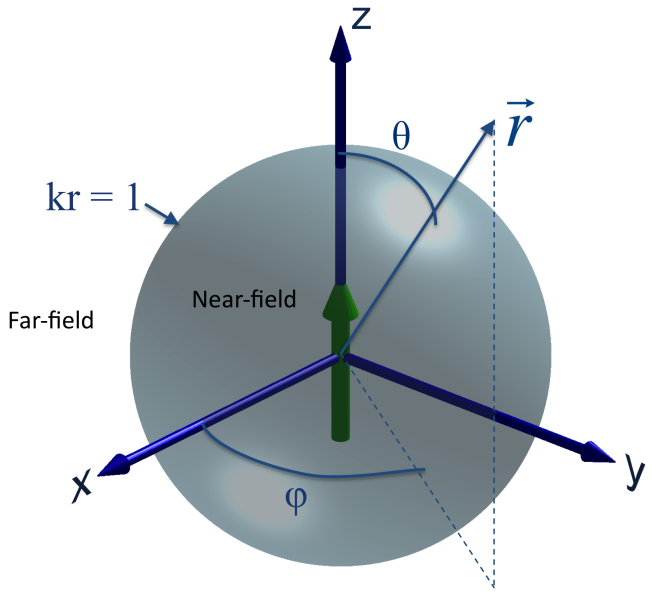


Figure 1.1: Framework adopted in this section. The green arrow indicates the $z$ oriented point electric dipole. The gray sphere symbolizes the radian sphere ($kr = 1$), separating the far-field and the near-field regions. $\vec{r} \equiv \mathbf{r}$ is the position vector. The spherical coordinate system is also shown.

and

$$\mathbf{H}(r) = \frac{1}{Z}\frac{k^2}{\varepsilon}\frac{e^{ik_\mu r}}{r^2}\left[\left(1+\frac{i}{kr}\right)\mathbf{r}\times\mathbf{p}\right] \tag{1.14}$$

being $Z$ the impedance of the medium defined as:

$$Z = \sqrt{\frac{\varepsilon}{\mu}} \tag{1.15}$$

To simplify the problem, we consider the particular case of a dipole located at the origin and oriented on the $z$ direction ($\mathbf{p} = p_z\hat{u_z}$) as scketched in Fig.1.1 and express $\mathbf{r}$ and $\mathbf{p}$ in spherical coordinates. We obtain for the fields in spherical coordinates $E_r$, $E_\theta$ and $E_\varphi$:

$$E_r(r) = p_z\frac{2icos(\theta)}{\varepsilon}\frac{e^{ik_\mu r}}{r}k_\mu^2\left[\frac{1}{ik_\mu^2 r^2}-\frac{1}{k_\mu r}\right] \tag{1.16}$$

$$E_\theta(r) = p_z \frac{sin(\theta)}{\varepsilon} \frac{e^{ik_\mu r}}{r} k_\mu^2 \left[ \frac{1}{k_\mu^2 r^2} + \frac{1}{ik_\mu r} - 1 \right] \tag{1.17}$$

and,

$$E_\varphi(r) = 0 \tag{1.18}$$

and similarly for the spherical coordinates of the magnetic field $H_r$, $H_\theta$ and $H_\varphi$:

$$H_r(r) = H_\theta(r) = 0 \tag{1.19}$$

$$H_\varphi(r) = Z p_z \frac{sin(\theta)}{\varepsilon} \frac{e^{ik_\mu r}}{r} k_\mu^2 \left[ \frac{-i}{k_\mu r} - 1 \right] \tag{1.20}$$

### 1.2.1 Radiation regions

The electric and magnetic fields for the infinitesimal dipole described by equations 1.16-1.18 and 1.19-1.20 , are valid for any point of the space except at the position of the dipole itself, where it diverges. A closer look at these equations reveals the interesting properties of the radiation of such a source.

At a first glance it can be easily observed that the expressions present two asymptotical trends with very different behaviour:

- Far-field ($kr >> 1$):

  When taking the $kr >> 1$ limit, the expressions for the fields can be reduced to:

$$E_\theta(r) \simeq -p_z \frac{sin(\theta)}{\varepsilon} \frac{e^{ik_\mu r}}{r} k_\mu^2 \tag{1.21}$$

$$H_\varphi(r) \simeq -Z p_z \frac{sin(\theta)}{\varepsilon\sqrt{\mu}} \frac{e^{ik_\mu r}}{r} k_\mu^2 \tag{1.22}$$

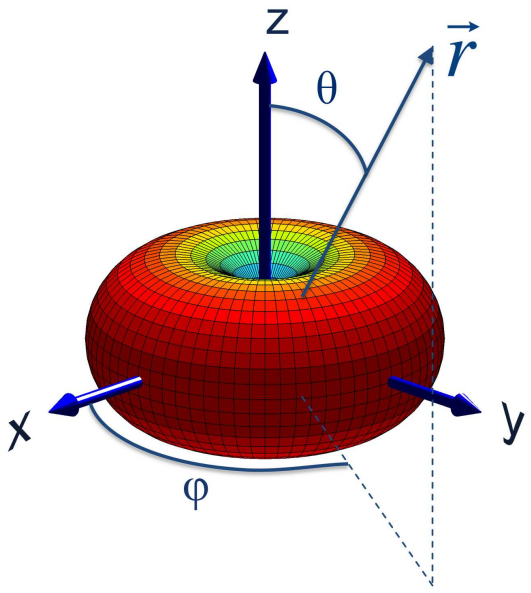


Figure 1.2: Radiation pattern of an electric point dipole located at the origin of coordinates and oriented on the z axis. $\vec{r} \equiv \mathbf{r}$ is the possition vector.

$$E_\varphi(r) = E_r = H_r(r) = H_\theta(r) = 0 \tag{1.23}$$

This region of space is usually know as the *far-field* region. For this region, the $E_r$ term vanishes and the $E_\theta$ is the only component that survives for the electric field. This means that the radiated electric field is transversal and linearly polarized in this region of the space. The magnetic field, on the other hand is polarized on the $\varphi$ direction, being, obviously, perpendicular to the electric field.

If we now observe the angular dependence of the electromagnetic fields of 1.21 and 1.22, we can see how the radiation is simmetric with respect to $\varphi$ while it presents a $sin(\theta)$ dependence for $\theta$. Fig.1.2 shows a 3 dimensional representation of the total electric field for this region of the space.

- Near-field ($kr << 1$):

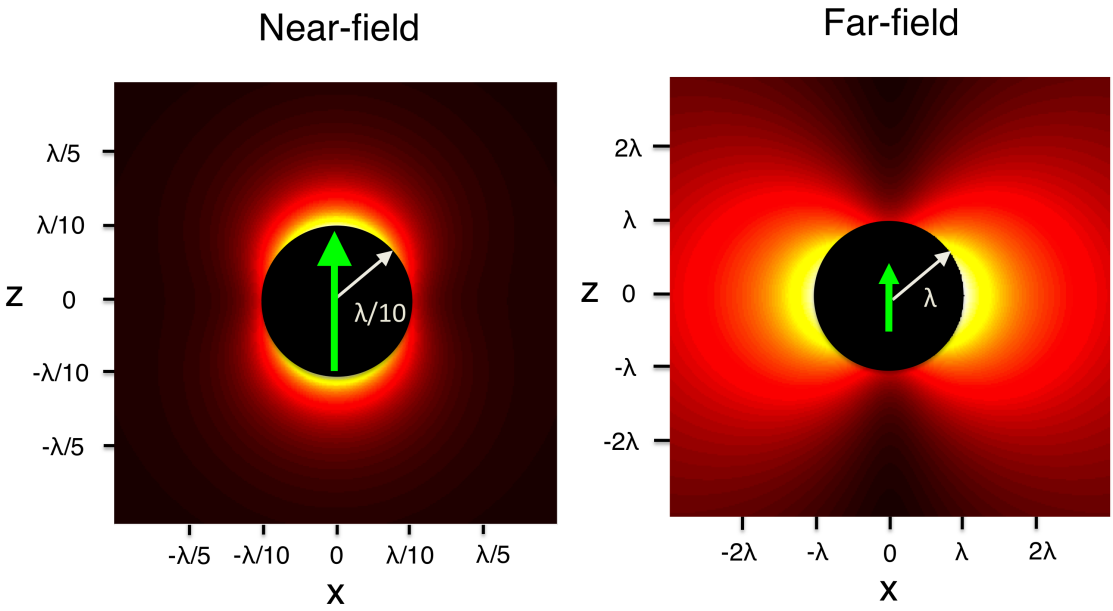


Figure 1.3: Cross section on the XZ plane of the total electric fields induced by a point dipole located at the origin and oriented along the z direction (see Fig.1.1) for a) The near-field region ($kr < 1$) and b) the far-field region ($kr > 1$)

If we now consider the $kr << 1$ limit, the expresions of the fields can be reduced to:

$$E_r(r) \simeq p_z \frac{2cos(\theta)k_\mu}{\varepsilon}\frac{e^{ik_\mu r}}{r^3} \tag{1.24}$$

$$E_\theta(r) \simeq_z \frac{sin(\theta)}{\varepsilon}\frac{e^{ik_\mu r}}{r^3} \tag{1.25}$$

$$H_\varphi(r) \simeq -iZp_z \frac{sin(\theta)}{\varepsilon\sqrt{\mu}}\frac{e^{ik_\mu r}}{r^2}k_\mu \tag{1.26}$$

$$E_\varphi(r) = H_r(r) = H_\theta(r) = 0 \tag{1.27}$$

This region is referred to as the *near-field* region. In this volume of the space the magnetic fields are much weaker than the electric fields, since they follow an $1/r^2$ dependence while the electric field increases as $1/r^3$. Furthermore, on

equations 1.24 and 1.25 we can observe how the electric field has two different components, one transversal ($E_\theta$) and the other longitudinal ($E_r$) to the orientation of the dipole. The transverse component of the electric field has a $sin(\theta)$ dependence on $\theta$ while the longitudinal one varies with $cos(\theta)$. The presence of both contributions and their different spatial behavior indicates that the distribution of the electric fields in this region is way different to the one present in the far-field region of the space. Fig.1.3 shows the electric field distributions for both regions of the space on a XZ cross section across the position of the dipole. We can easily observe how the field distribution differs in both cases. Close to the position of the dipole, in its near-field region (Fig.1.3a), the electric field is strongly localized on the extremities of the dipole while at larger distances, on the far-field region (Fig.1.3b), the field spreads transverse to the dipole axis (as shown in the radiation pattern in Fig.1.2).

Fig1.4 shows the dependence of the transverse field with respect to $kr$. It can be observed how the transition from the near-field to the far-field occurs for $kr = 1$. For that value, as it can be deduced from equation 1.17 the contributions of the far-field and near-field compensate and only the $1/(ik_\mu r^2)$ term survives. This space between the near-field and far-field recieves the name of *radian sphere* [1].

In classical antenna theory, there is an interest in the transmission and reception of EM waves, thus, the far-field properties of the radiating systems are essential aspects of study. The working principles beyond many antenna based emerging applications at infrared (IR) and visible frequencies instead are strongly based near-field properties of antennas. As a consequence, the study of the nanoscale near-field properties of nanoantennas has become of crucial importance on the field of nanophotonics.

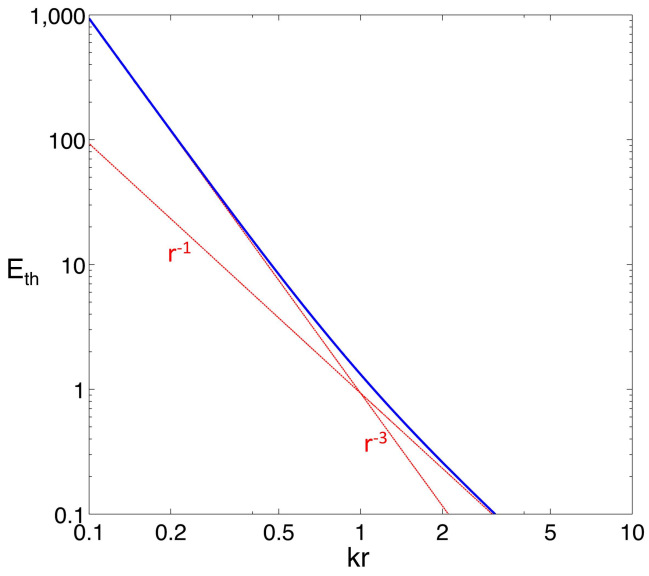


Figure 1.4: Radial decay of the transversal fields of the dipole ($E_\theta$. The graph represents the absolute value of the transversal fields calculated as the magnitude of the sum of terms inside the brackets in equation 1.17

.

### 1.2.2 Dipolar emitters

The infinitesimal dipole is a good approximation of the electromagnetic response of very small dielectric objects ($\sim \lambda/100$) and it can also simulate well the emission and absorption properties of certain molecules, atoms and quantum dots. In order to describe the electromagnetic response of such systems employing a dipolar approximation, a quantity connecting the applied electric field $\mathbf{E}$ to the resulting dipolar moment $\mathbf{p}$ is needed. That quantity receives the name of electric polarizability $\alpha$ and it is defined as the ratio of the induced dipole moment $\mathbf{p}$ to the applied electric field $\mathbf{E}$.

$$\mathbf{p}(\omega) = \alpha(\omega)\mathbf{E}(\omega) \tag{1.28}$$

The value of the polarizability $\alpha(\omega)$ is a measure of the potential of an object to separate its charges. For instance, for the concrete case of a dielectric sphere in vacuum,

$\alpha(\omega)$ can be expressed as

$$\alpha_0(\omega) = \varepsilon a^3 \frac{\varepsilon - 1}{\varepsilon + 2} \tag{1.29}$$

where $a$ is the radius of the sphere, and $\varepsilon$ is its permittivity. If the sphere is non absorbing ($Im(\varepsilon) = 0$), the expression of the polarizability diverges for a value of the dielectric function $\varepsilon = -2$. In order to avoid this singularity, Draine's radiative correction must be taken into account [11, 12]. With this correction the polarizability reads as follows,

$$\alpha(\omega) = \alpha_0(\omega) \left(1 - i\frac{k_\mu^3}{6\pi}\alpha_0(\omega)\right)^{-1} \tag{1.30}$$

Nevertheless, the exact response of bigger objects can not be approximated by these formalism. In order to analyze these systems other methods need to be employed. For certain geometries, specially the ones where the perfect metal approximation is still valid and only one of the sizes is much larger than the rest, analytical integral approaches can be adopted, employing infinitesimal dipoles as differential radiating elements. If the permittivity of the material can not be considered to be infinite or/and the relative sizes of the structure are comparable, Maxwell's equations need to be numerically solved. There exist several numerical methods to calculate the electromagnetic response of any structure. All the numerical calculations presented in this thesis had been calculated through the Boundary Element Method (BEM). The details of this numerical method will be further introduced on appendix A.

## 1.3 The electromagnetic spectrum

Electromagnetic radiation is classified by its characteristic frequency or wavelength. The range of all possible frequencies of radiation receives the name of *electromagnetic*

*spectrum*. Fig.1.5 shows a typical representation of this concept.

The utilization of radiation-based systems started in the beginning of $19^{th}$ century with the discovery of the radio. These first attempts to exploit the electromagnetic radiation made use of low frequency electromagnetic waves. From that moment, radiation based technologies evolved to higher frequencies covering the a progressively larger part of the electromagnetic spectrum.

Every frequency range has its own characteristic properties and results more appropriate for certain applications. For example, earth's atmosphere presents a transmission window on the frequency range of the GHz-s. Thus, this regime results to be ideal for satellite earth communications and this frequencies are nowadays employed for applications such as the GPS, TV satellite broadcasting, etc. Other frequency ranges result to be more suitable for other applications. In order to avoid overlapping between the use of ranges of the spectrum and to establish some guidelines on the appropriateness of certain wavelengths for concrete uses, the International Telecommunication Union (ITU) tabulates the electromagnetic spectrum dividing it into frequency sets which are known as frequency bands.

Up to date, antenna based commercial technologies exploit the electromagnetic spectrum up to the THz regime. Recent technological advances are permitting to go one step further in this race towards the controlled radiation and reception of waves of progressively higher frequencies, and nowadays it is experimentally possible to exploit the IR and visible part of the spectrum.

Even though antennas have been traditionally related to communication systems as transducers of electricity to propagating electromagnetic light, the special properties of the light-matter interaction in the optical range induced to reframe this concept. Metals are extremely lossy for these frequencies, because of the small values of their permittivities for these wavelengths. That makes impossible the propagation of elec-

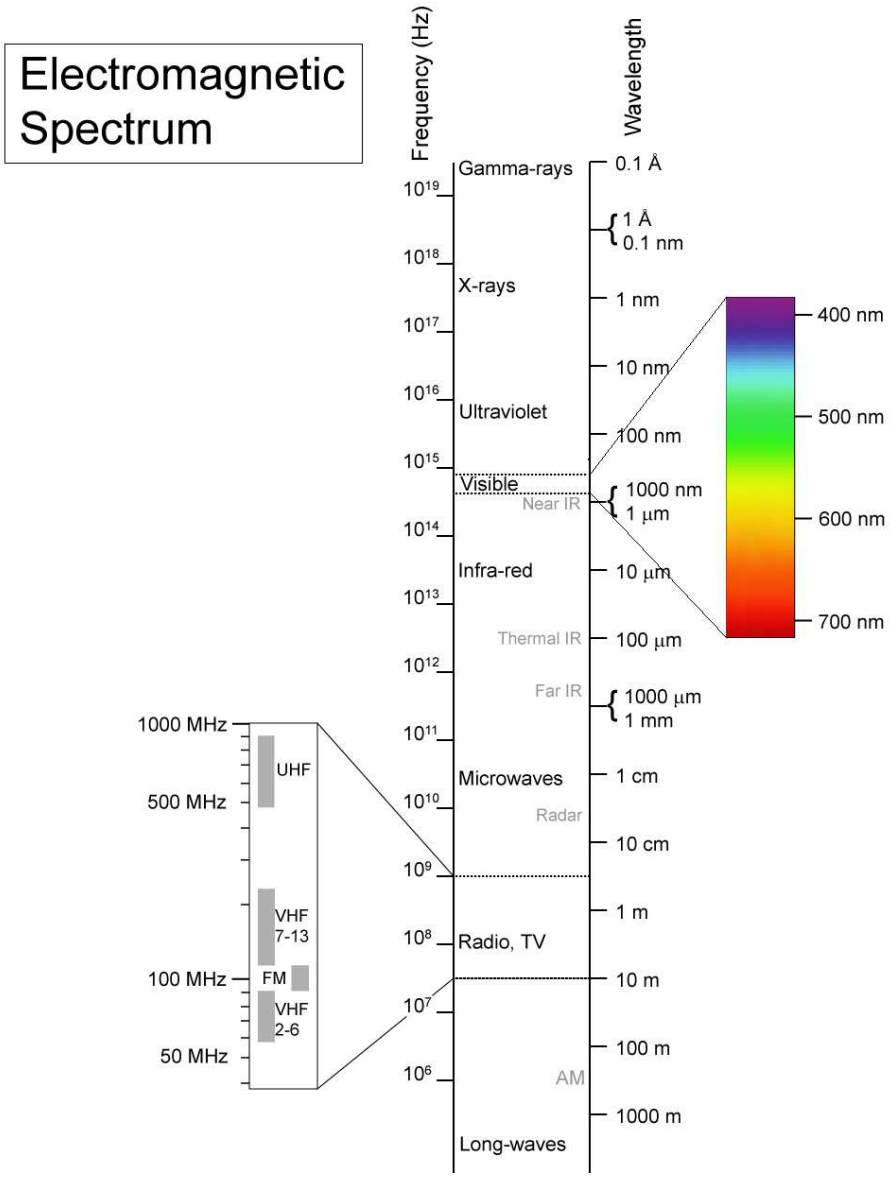


Figure 1.5: Band division of the electromagnetic spectrum (from: *Creative Commons)*

tric signals of such large frequencies through metallic wires. This localized energy can be then guided through different mechanisms, or it can be employed for specific applications as field enhanced spectroscopies, microscopies etc. as we will develope in Section1.5.

## 1.4 Optical antennas: factors influencing the response

Optical antennas are strongly analogous to their radio-frequency and microwave counter paths. Nevertheless, there are crucial differences in their physical properties and scaling behavior. Most of these differences arise from the fact that the permittivity of metals is not infinite at optical frequencies. This makes the metals not to behave as perfect conductors but rather as strongly correlated plasmas described as a free electron gas. This fact affects the electromagnetic response of metallic objects in two different but related ways:

- The first consequence of the finite permittivity is that the skin depth of metallic objects near a surface does not tend to zero. This alters the canonical response of nanoscale metallic objects because the penetration of the electric fields can be comparable to the characteristic sizes of the objects in many cases. The consequences of this effect will be further studied in Section 1.4.2.

- On the other hand, as we will study in the next Section, the plasma response of the electronic cloud resonates at specific wavelengths. Besides their intrinsic interest as physical phenomena, these resonances, known as plasmons, present characteristic properties that modify and boost the response of metallic objects at the optical wavelength range.

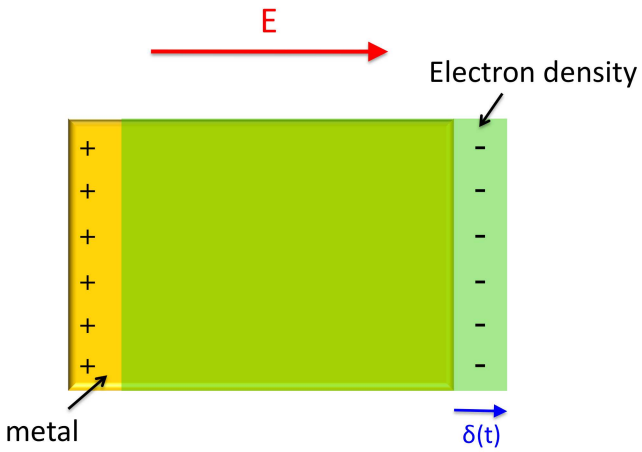


Figure 1.6: Schematics of the bulk plasmon oscillation in a metal

### 1.4.1 Plasmons

The motion of the electron gas in metals can be described by a classical equation of dynamics where the electron cloud follows an harmonic oscillatory behavior. If we consider the metal as a three-dimensional crystal of positive ions and a free electron gas moving on the periodic potential created by the ions, when an electric or electromagnetic excitation is applied to the metal, the electron cloud will react to the corresponding electric field displacing from its equilibrium position. On the other hand, the positive ionic background induces a restoring force attracting the electron cloud back to its original position. The action of those two forces will cause an oscillation of the electron gas around the equilibrium position (see schematics on Fig 1.6).

The mechanical equation of the displacement of the electron gas, following this harmonic oscillation, can be expressed as:

$$nm_e \frac{d^2}{dt^2}\delta(t) = -enE(t) = -4\pi n^2 e^2 \delta(t) \tag{1.31}$$

Where $\delta(t)$ is the displacement of the electron gas, $n$ is the conduction electron density,

$e$ is the elementary charge and $m_e$ is the electron mass.

We can deduce from the previous equation that there is a natural frequency for the electron cloud, that we will refer to as the bulk plasma frequency $\omega_p$:

$$\omega_p = \sqrt{\frac{4\pi n_e e^2}{m_e}} \tag{1.32}$$

which basically depends on the electronic density of the metal.

The dielectric response of a free-electron gas can be obtained classically by describing the polarization of an homogeneous medium composed of atoms with free electrons. In this case the typical Lorentz oscillator response becomes what is known as Drude-like response:

$$\varepsilon = 1 - \frac{{\omega_p}^2}{\omega(\omega + i\Gamma)} \tag{1.33}$$

with the response depending on the plasma frequency $\omega_p$ and the damping $\Gamma$ of the metal given manly by the relaxation of the electron gas motion into lattice vibrations or phonons.

Coupling light to plasmon excitations in matter is only possible for special geometries of the material. For instance, when a metal-dielectric surface is introduced, solutions to Maxwell's Equations can be obtained when applying the proper boundary conditions. Since the permittivity of the metal and the dielectric medium are of opposite signs, there exist solutions supporting collective excitations of the free electron plasma propagating along the surface. These excitations, known as surface plasmon polaritons (SPP-s) are evanescent in the direction normal to the surface. Fig. 1.7a shows an schematic sketch of such solutions.

In an electrostatic approximation, the dispersion relation of SPP-s can be expressed as:

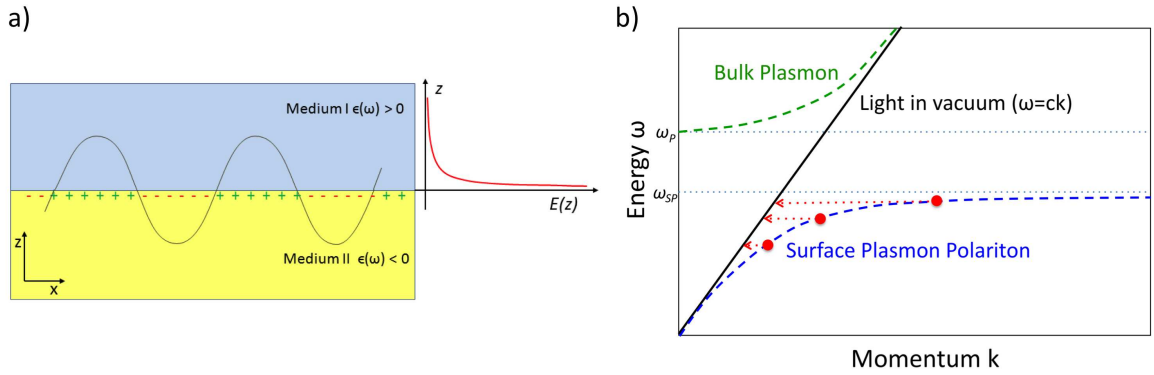


Figure 1.7: a) Schematics of SPP at an interface separating two semi infinite regions with two dielectric functions of different sign, propagating along x direction and confined in z direction. b) Energy ($\omega$) versus momentum ($k$) dispersion line of the propagating surface plasmon polariton (blue-dashed line). The bulk plasma frequency $\omega_p$ and the surface plasmon energy $\omega_s = \omega_p/\sqrt{2}$ are marked as dotted horizontal lines. Closing the boundaries of the surface provides momentum (shown through red-dashed lines) allowing the localized surface plasmons (LSP) to couple to the light line ($\omega = ck$).

$$\omega_{SPP} = c\sqrt{\frac{\varepsilon_2 + \varepsilon_1}{\varepsilon_2\varepsilon_1}}k \tag{1.34}$$

where $\varepsilon_1$ and $\varepsilon_2$ are the permittivity of the dielectric and the metal respectively. The dispersion curve of SPP-s is shown in Fig. 1.7b.

The energy of such excitations lays on the visible part of the electromagnetic spectrum for the case of metal-dielectric interfaces. However, the excitation of surface plasmons on a flat semi-infinite metal surface with light is not possible because energy and momentum cannot be conserved simultaneously. This is shown schematically by the solid and blue-dashed dispersion lines for light and the surface plasmon respectively in Fig 1.7. However, there are several ways to provide the additional momentum needed for momentum conservation so that the surface plasmon can couple to incident light. One way is to modify the planar metal surface by means of indentations or gratings that can provide "lattice" momentum to ensure momentum conservation.

Momentum conservation is also possible when light is coupled to the plasmon excita-

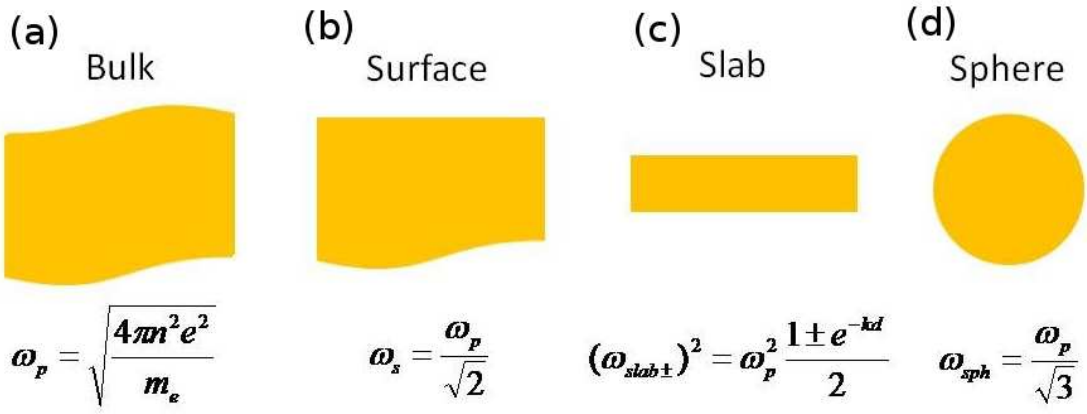


Figure 1.8: Plasmon energies for different metallic systems. Schematics and energy of (a) the bulk plasmon. (b) the surface plasmon on the electrostatic approximation. (c) the plasmonic modes for a metallic slab on vacuum on the electrostatic approximation, $k$ is the wave vector and $d$ the slab thickness. (d) the sphere plasmon on the electrostatic approximation.

tions of small metal particles. Here, the finite geometry provides the extra momentum needed for momentum conservation. Discrete excitations, known as metal nanoparticle plasmons, that can couple effectively to light are possible, as schematically shown by the red-dashed lines in Fig 1.7. So, Together with propagating solutions of SPPs, we can find localized modes at closed boundaries such as in nanoparticles, often addressed as localized surface plasmons (LSP). Their characteristic energies depend strongly on the geometry of the particle, the size, the environment and the coupling to other structures. These localized resonances at optical frequencies are what is known as optical antenna resonances. Therefore, the plasmonic resonances of nanoparticles and the concept of antenna modes merge together at optical frequencies.

The dielectric formalism provides an adequate framework to describe the optical response metallic systems. In general, one can find surface mode solutions for any system, by applying proper boundary conditions to the potentials and the fields at the interfaces. In small structures, where the dimensions of the object are smaller that the

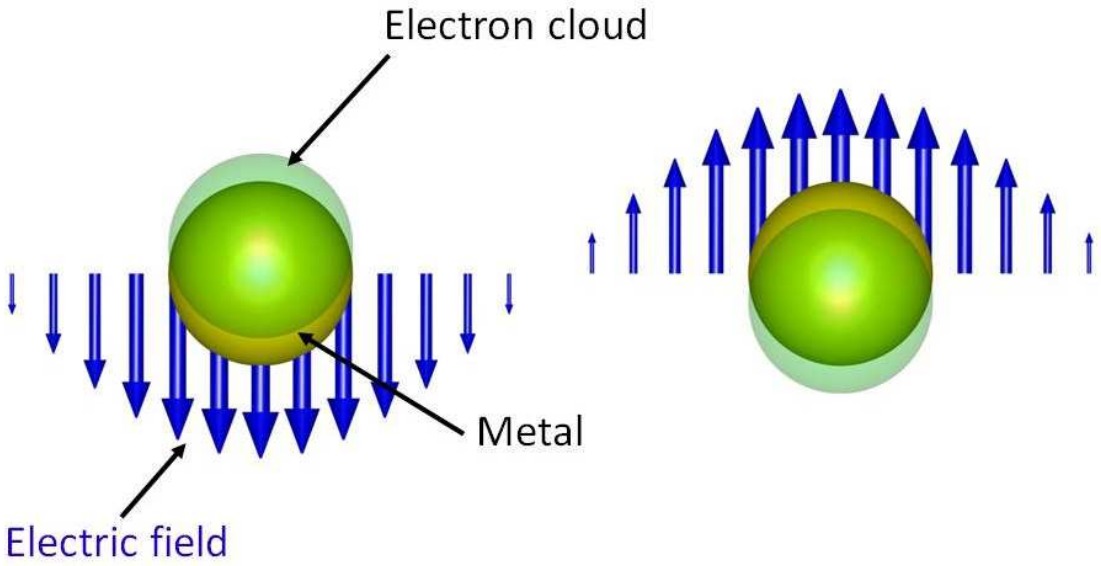


Figure 1.9: Schematics of the localized surface plasmon (LSP) excitation in a metallic sphere.

wavelength of light, the energies of the plasmonic resonances can be obtained by solving Laplace's equation within the electrostatic approximation. Fig 1.8 summarizes the plasmonic resonant energy for three different systems with use of this approximation. For example, the energy of the localized surface plasmon resonance (sketched in Fig. 1.9)of a small metallic sphere for instance can be easily deduced through the expression of its polarizability. As it was already shown in Section 1.2.2, since the polarizability of a small, absorbing sphere is

$$\alpha_0(\omega) = \varepsilon a^3 \frac{\varepsilon - 1}{\varepsilon + 2} \tag{1.35}$$

it presents a resonance when $\varepsilon = -2$. From Drude's expression for the dielectric function of a metal (Eq.1.33), if $\Gamma = 0$:

$$\varepsilon = 1 - \frac{{\omega_p}^2}{\omega_{sph}^2} = -2 \tag{1.36}$$

where $\omega_{sph}$ is the energy of the dipolar surface plasmon excitation of the sphere. Then,

$$\omega_{sph} = \frac{\omega_p}{\sqrt{3}} \tag{1.37}$$

as it is summarized in Fig 1.8d.

### Special properties of surface plasmons

LSP-s exhibit some distinct and special properties which have generated promising prospects in a variety of fields of science and technology. We summarize some of these properties:

- *Localization of the electromagnetic fields:* The fields induced by surface plasmons decay exponentially as we move away from the interface where they are excited. Thus, all the electromagnetic effects induced by those fields are reduced to a small region close to the surface (typically some nanometers). Complementarily, plasmons have shorter wavelength compared to the incoming source that excites them. As a consequence of these two effects, it is possible to concentrate light on regions smaller than the diffraction limit.

  Thanks to this property, for example greater resolution can be achieved if plasmons are used for imaging purposes. The use of plasmon excitations for subwavelength optical microscopy will be studied in Chapter 4. On the other hand, this feature is also essential for spectroscopic applications where a small amount of molecules located near a surface con be sufficient for the detection purpose.

- *Field enhancement:* The plasmonic resonances induce charge pile up at the surface of the metals and those charges induce electromagnetic fields on the surroundings of the surface. Therefore, the fields are enhanced compared to electro-

magnetic fields in free space. The mechanisms which maximize the field enhancement will be detailed in Chapter 3. This field enhancement is a key property for many photonic applications, such as spectroscopy and sensing. The use of field enhancement to boost the sensitivity of spectroscopy techniques as SERS and SEIRA will be further studied in Chapter 2

- *Tunability:* Plasmons have also the capability of tuning the energy of their resonances through the modification of both the geometry and/or the coupling between different systems [13–15]. This opens up the door to engineer the optical spectral response in optically active systems to optimize the properties of plasmons for the requirements of a particular application. Chapter 5 will introduce two different mechanisms for the control of the optical response of metallic nanoantennas.

  In addition, plasmons are extremely sensitive to the environment that surrounds them. Thus, a small change on the dielectric function of the surrounding medium can produce large spectral shifts on the far-field radiation of the system.

### 1.4.2 The role of the skin depth

Inside any perfect metallic structure, being the permittivity infinite, the electric fields should tend to zero, and consequently the current density should flow only at the boundaries of the structure. The finite permittivity of metals at visible and IR frequencies allows the electric fields, and thus the current density to penetrate some tens of nanometers inside the metals. This fact in addition to the effects induced by the excitation of surface plasmons that where discussed on the previous section, modifies the optical response of metallic structures at this frequency range.

In a general case, the current density $J$ inside an infinitely thick plane conductor

decreases exponentially from the surface with depth d, as follows:

$$J = J_s e^{-r/\delta} \tag{1.38}$$

being $J_s$ the value of the current density at the surface of the conductor, $r$ the penetration distance and $\delta$ the skin depth of the metal.

The skin depth of a metal is defined as the depth inside the material at which the current density decays to a value of $1/e$ ($\sim 0,37$) of the value of the current density at the interface ($J_s$). This skin depth can be calculated as:

$$\delta(\omega) = \sqrt{\frac{1}{2\sigma\omega\mu_0}} \tag{1.39}$$

where, $\delta(\omega)$ is the skin depth, $\mu_0$ is the magnetic susceptivility in vacuum, and $\sigma$ is the conductivity of the material calculated from the experimental dielectric function $\varepsilon$ following Drude's formalism, as follows:

$$\varepsilon(\omega) = 1 + i\frac{\sigma(\omega)}{\varepsilon_0\omega} \tag{1.40}$$

So, the expression for the conductivity within this model is:

$$\sigma(\omega) = -i\varepsilon_0\omega(\varepsilon(\omega) - 1) \tag{1.41}$$

In Fig. 1.10 the spectral dependence of the skin depth for the case of gold, calculated through Eq. 1.39 is shown. For very large wavelengths the dielectric function of the metal follows a $\varepsilon \propto 1/\omega^2$ tendency (see Eq.1.33). Hence, the conductivity results to be proportional to $\omega$ and the skin depth increases linearly with the wavelength. In the visible range of the spectrum, the finite value of the permitivitty does not permit any approximation and the spectral details of the dielectric function determine the value

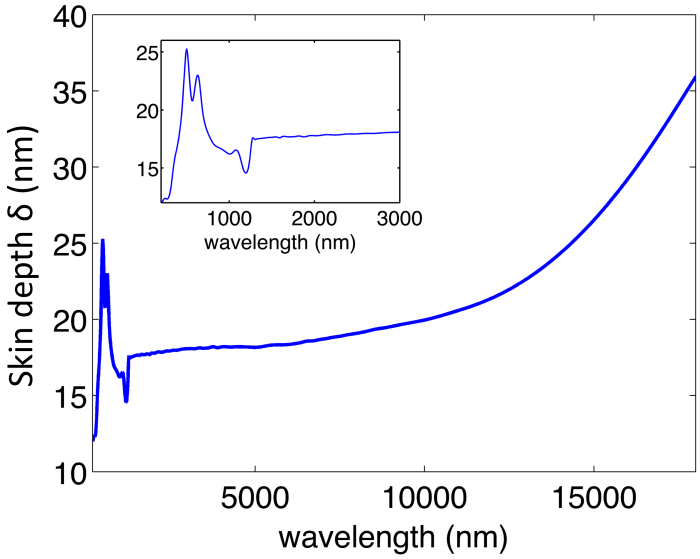


Figure 1.10: Espectral dependence of the skin depth for gold, calculated through Eq. 1.39. Inset: Zoom over the visible and near-IR part of the spectrum.

of the skin depth.

The dimensions of optical antennas are tipicaly in the nanoscale and comparable to the values of the skin depth shown in Fig.1.10. As a consequence, the optical response of these structures will differ from the standard one. We will address this issue by comparing the behavior of almost perfect metallic rod like antennas of 400 nm length and variable width with gold antennas of the same dimensions where experimental dielectric function taken from Palik [16] will be employed. For the calculations of the almost perfect metallic case, a dielectric function of $\varepsilon = -2842 + 1339i$ will be considered (which is the value of the experimental dielectric function of gold for $\lambda$=20$\mu$ m).

In Fig. 1.11 we show a comparison of the extinction cross section spectrum of a relatively thick gold nanoantenna of width w = 200 nm and the response of an almost perfect metallic antenna of the same dimensions. Being the radius of the rod (100 nm) significantly larger than the skin depth for the resonant wavelength ($\delta \sim 18nm$), no

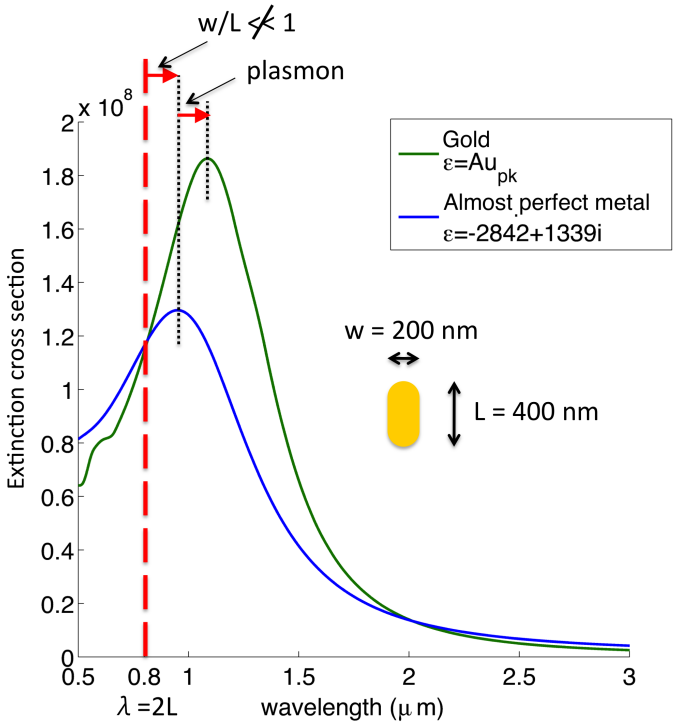


Figure 1.11: Comparison of the optical response of an almost perfect metallic antenna ($\varepsilon = -2842 + 1339i$, L = 400nm, w = 200 nm) with respect to the response of a reallistic antenna ($\varepsilon = Au_{pk}$) of the same dimensions. The red dashed line indicates the possition of the $\lambda/2$ resonance for an antenna of L = 400 nm. The resonance shift between the resonance predicted by antenna theory ($\lambda = 2L$) and the almost perfect metallic antenna resonance is due to the comparable dimensions of the length and the width of the considered antenna. The shift between the resonances of the realistic gold antenna and the almost perfect metallic antenna is due to the excitation of surface plasmons in the nanostructure.

skin depth effects are expected. The resonance of the realistic gold antenna is red-shifted with respect to the resonance of the almost perfect metallic one due to the excitation of surface plasmons at the nanostructure.

If $w/L << 1$, antenna theory predicts a first order resonance for perfect metallic antennas for a wavelength of $\lambda = 2L$ (dashed red line in Fig. 1.11). The discrepancy between the resonant frequency of the quasy-perfect metallic antenna and the resonance predicted by antenna theory (Fig. 1.11) is due to the non negligible width of the antenna

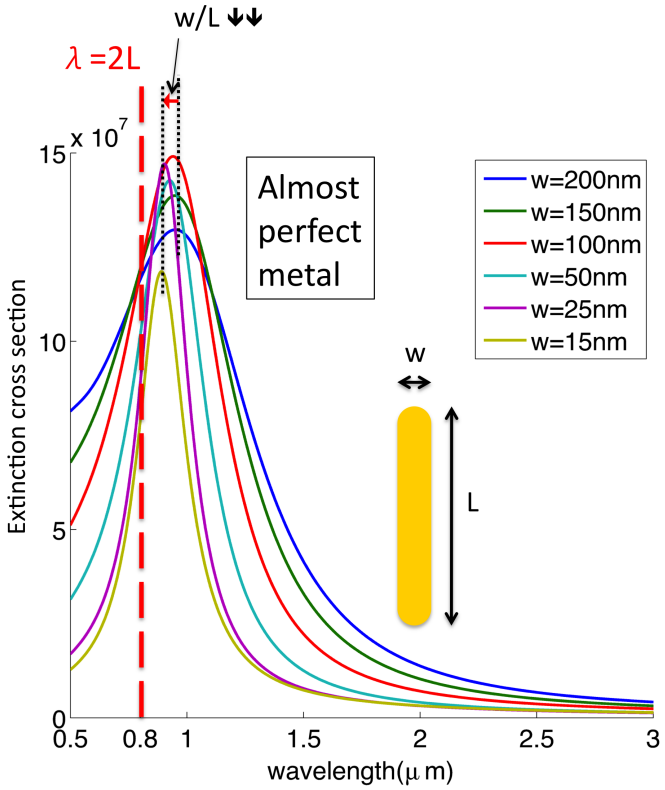


Figure 1.12: Optical response of a set of almost perfect metallic antennas with L = 400 nm for several widths. As the ratio w/L decreases, the dipolar resonance of the antenna approaches the $\lambda/2$ resonance predicted by antenna theory.

w with respect to its length L. The results presented in Fig. 1.12 verify this hypothesis. In this case we study the response of a set of almost perfect metallic antennas eith length L = 400 nm number of widths w. As the ratio between w and L decreases, the resonance of the antenna approaches the $\lambda/2$ resonance predicted by antenna theory.

In order to study the effect of the skin depth in realistic nanoantennas, we show the far-field extiction spectra of a set of gold antennas of L = 400 nm for a set of decreasing widths. The results are summarized of Fig. 1.13. The skindepth for the IR part of the spectrum is about 18nm (Fig. 1.10). Significant effects due to the non-negligible penetration of the electric fields are expected to arise only for antennas with widths smaller than 36 nm. Fig. 1.13 shows how antennas with widths $w \geq$50 nm

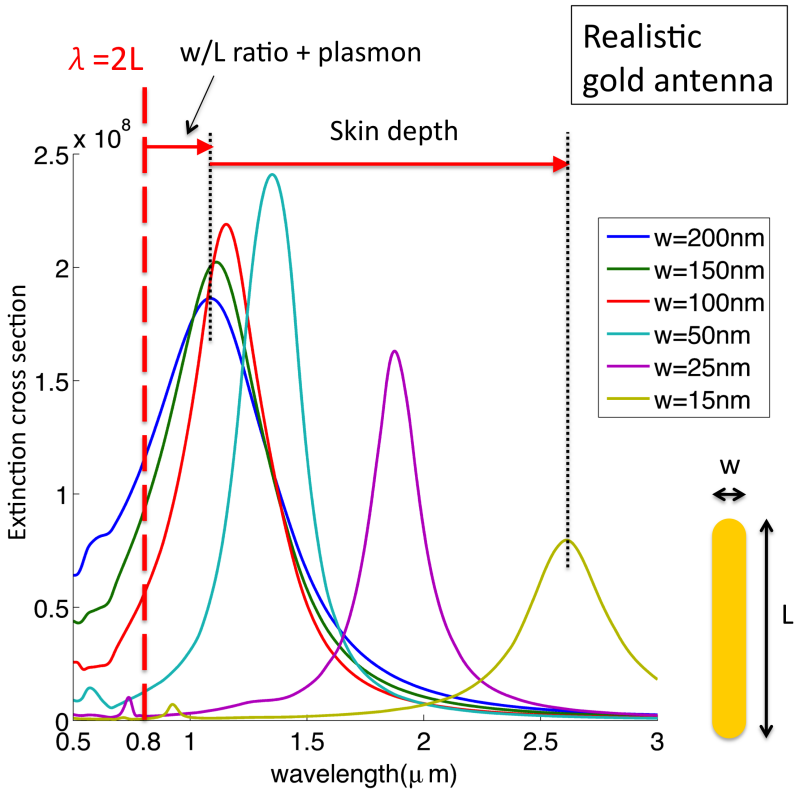


Figure 1.13: Optical response of a set of realistic gold antennas with L = 400 nm for a variety of widths w. As the ratio w/L decreases, the dipolar resonance of the antenna is strongly red shifted due to the non negligible penetration of the electric field inside the antenna.

present a slight red shift for decreasing widths. For thinner antennas indeed, the shift is dramatically enhanced.

To conclude, we calculate the current density distribution inside the antennas by applying Ohm's law:

$$\mathbf{J} = \sigma \mathbf{E} \tag{1.42}$$

being $\mathbf{E}$ the electric field induced inside the structure.

In the antennas presented here, since w$<<\lambda$ we can consider that only $m = 0$ (axially simmetric) modes are effectively excited, therefore $\mathbf{E} = E_z$, being $E_z$ the electric field oriented in the direction of the antenna axis. In that case $\mathbf{J} = J_z =$

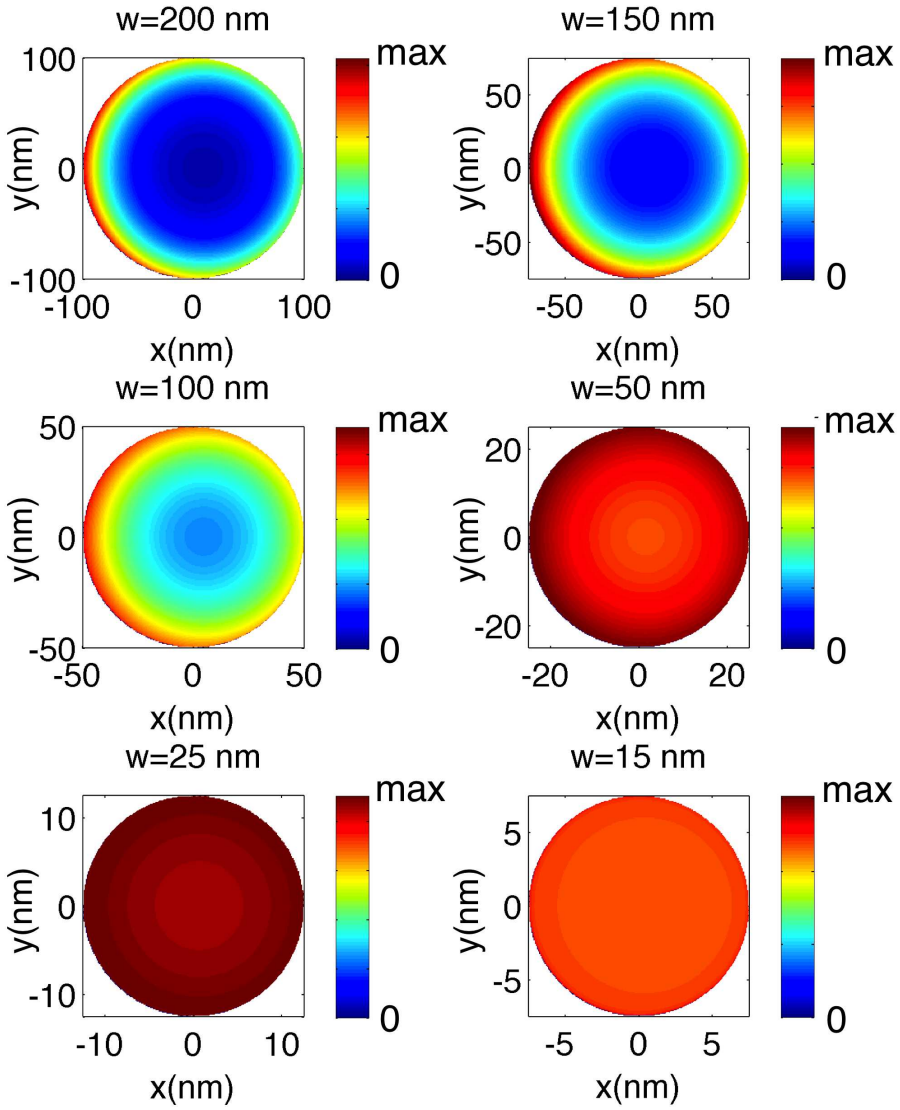


Figure 1.14: Maps of the current density (in arbitrary units) induced inside the set of antennas studied in Fig. 1.13 for the dipolar resonance. Cross sections at the center of the antennas are presented. For $w < 50nm$ the current density is no longer confined at the boundaries of the structure. Therefore the energies of the resonances are strongly modified (see corresponding spectra in Fig. 1.13).

$\sigma E_z$. Fig. 1.14 presents a set of calculations of the current densities excited inside the antennas studied in Fig. 1.13 at their dipolar resonance. Cross sections of the current density across the center of the antennas are plotted. In this set of calculations we can observe how the current density flows manly at the boundaries of the structure for widths $w \geq 50$ nm. For thinner antennas, the current density penetrates the rods and thus the modal distribution of the associated electric field changes dramatically. As a consequence, the energies of these new modes are strongly modified inducing the intense red-shifts shown in Fig. 1.13.

This set of calculations demostrates that the effect of plasmons and the penetration of the fields modifies the optical response of nanoantennas and therefore an accurate and exact modeling of the response is needed when exact spectral features are needed. This is one of the reasons of the need of this work.

## 1.5 Applications of optical antennas

The properties of surface plasmons that we introduced in Section 1.4.1 can serve as the basis for many novel technological applications or to boost the efficiency of well established spectroscopic techniques.

A considerable amount of research has been devoted to the propagation of optical signals by means of plasmon guides and interconnectors aiming for fully integrated optical circuits. In this thesis we will focus our attention on the applications derived from the excitation of localized surface nanoparticle plasmons (LSP-s), also called antenna resonances as mentioned before, that are of great interest in field-enhanced spectroscopy and microscopies. As mentioned in the previous section, these applications rely mainly on four beneficial aspects of LSP: (i) the confinement of the electromagnetic fields, (ii) the field enhancement associated to the localization, (iii) the sensitivity of the response

to environmental changes, and (iv) the tunability of the spectral response.

We can cite some applications within the context of this thesis:

- *Surface-enhanced spectroscopy:* the confinement and enhancement of the electromagnetic fields associated to plasmons, can be extremely beneficial for different spectroscopic techniques such as Raman and infrared spectroscopy because their signals rely on the intensity of the electromagnetic fields involved. When nanoparticles are used for this enhancing purposes, these techniques are described as field enhanced spectroscopy. Surface-enhanced Raman scattering (SERS) [3,4,17] and Surface-enhanced Infrared (IR) Absorption (SEIRA) [18] are among the most commonly used nowadays. [19]

  In the case of Raman spectroscopy, the sensitivity of the technique increases with the fourth power of the field since both the incoming and the outgoing fields are enhanced at the position where the molecules are located, therefore the enhanced field coming from plasmonic nanoparticles (nanoantennas) can enhance dramatically the sensitivity of the spectroscopy. On the other hand, as the fields are strongly localized, this effect permits to detect fewer molecules. Under certain circumstances it has been possible to detect even single molecules. [3, 4, 17]

  In direct infrared absorption spectroscopy, the sensitivity depends directly on the intensity of the field, i.e. on the second power of the amplitude instead of the fourth power, but even if the sensitivity increases less than for SERS, the benefits of the field enhancement have permitted to detect very small quantities of molecules, giving complementary information to the SERS signal. In one of the studies summarized in this thesis we demonstrate that an enhancement of five orders of magnitude on the sensitivity of SEIRA techniques can be achieved with the use of a single plasmonic nanoantenna as an active element (See Chapter2

and reference [20]).

- *Near-field optical microscopy:* In order to develop and optimize the applications mentioned here, it is essential to know not only the properties of the far-field radiation of the structures involved but also the near-field response (both in amplitude and phase). Scattering-type near-field optical microscopy (s-SNOM) [21] is one of the most appropriate techniques to obtain experimental information about the near-field response of metallic nanoparticles. This technique is a versatile optical imaging tool which overcomes the diffraction limit thanks to the confining capabilities of surface plasmons. Maps of the near-field distribution of nanoscale structures can be obtained by detecting the light scattered from a sharp probing tip oscillating above the surface of a sample. The details of the technique will be further explained on Chapter 4.

  On the other hand, the interaction between the microscope's probe and the sample can be exploited for new applications as the control of the optical response of plasmonic systems as will be further elaborated in this work (Chapter 5).

- *Sensing applications:* It has already been pointed out how surface plasmons are extremely sensitive to the environment. Changes in the surrounding medium of a plasmonic nanoparticle induce important spectral shifts on the position of the far-field resonance peaks. Those shifts can be easily detected by ordinary spectroscopy techniques, setting the basis of plasmon-assisted sensing techniques. [22]

  As the binding of molecules to a nanoparticle will change the local refractive index around the particle and thus the peak position, it is possible to develop biosensors employing these shifting properties of LSPs.

# CHAPTER 2

# RESONANT PLASMONIC AND VIBRATIONAL COUPLING IN A TAILORED NANOANTENNA FOR INFRARED DETECTION

Vibrational spectroscopy of molecules is of general importance in natural sciences, medicine and technology. Direct infrared observation of molecular vibrations from a reduced number of molecules is a current challenge in all these fields. The respective sensitivity can be increased several orders of magnitude with use of surface-enhanced scattering techniques such as surface enhanced Raman scattering (SERS) [3, 17, 23, 24] and surface enhanced infrared (IR) absorption (SEIRA). [25–32] The enhancement factor in these techniques essentially depends on the capacity of the environment to enhance the local electromagnetic fields. In SERS, the electromagnetic field enhancement is effective for both the incoming and the scattered radiation, and usually the local field enhancement profits from plasmon cavity modes with resonant wavelengths in the visible. [4] For direct excitation of vibrational modes, as it is the case in SEIRA, the electromagnetic field enhancement requires resonant excitation in the IR, because the

absorption scales with the intensity of the local field created at the molecules position. Until now, not more than three orders of magnitude of direct vibration signal enhancement have been achieved in typical SEIRA experiments [25–32] where a metal-particle ensemble is used as substrate. Its spectral response is strongly broadened by the mutual particle interaction and, additionally, by inhomogeneous particle geometries. The measured SEIRA signal is collected from a macroscopic area (typically $mm^2$) and represents an average over a variety of different sites with different near-field enhancement factors at spectral positions far away from the frequencies of the molecular vibrations.

IR and visible antennas lead to strong field enhancement of the near-field and their resonance frequencies can be easily engineered through the modification of their lengths and widths. Thus, they are much better candidates than regular grained surfaces to boost the sensitivity of SEIRA and SERS experiments. Fig. 2.1 illustrates the principle of an antenna boosting the capabilities of the SERS and SEIRA techniques. The nanoantenna is first tailored to hold a plasmonic resonance at the required wavelengths (visible for SERS and IR for SEIRA). Then, the molecules under study are placed on the vicinity of the resonant system. Since the Raman and vibrational absorption processes are proportional to the excitation field, the signal of the vibrations will be increased in certain areas close to the nanoantenna (hot-spots) where the near-field is maximum.

For Raman spectroscopies, this enhancing process will be beneficial not only for the excitation of the molecule but also for the radiation of the re-emited photons of lower energy, since the antenna will also serve as an enhancer of the scattering of the outgoing photon. The enhancing factor of the process $M_{sers}$ can be then written as,

$$M_{SERS} = \left|\frac{E_{local}(\lambda_0)}{E_0(\lambda_0)}\right|^2 \left|\frac{E_{local}(\lambda_R)}{E_0(\lambda_R)}\right|^2 \tag{2.1}$$

being $E_{local}$ the near-field generated by the antenna, $E_0$ the incoming field, $\lambda_0$ the

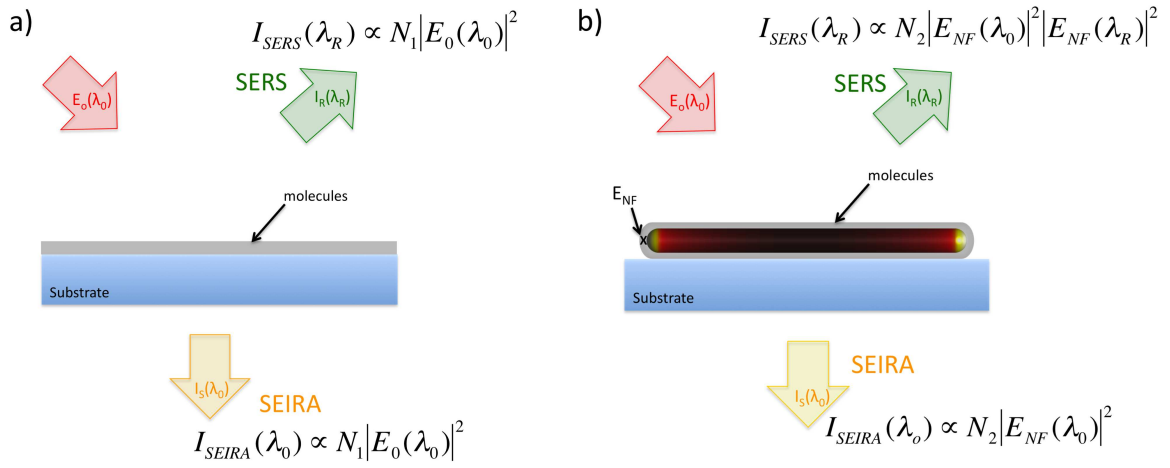


Figure 2.1: Schematics of a) Raman and IR absorption spectroscopy. One monolayer of molecules is deposited on top of a transparent substrate. The monolayer is then excited with light of wavelength $\lambda_0$ (visible for Raman spectroscopy and IR for absorption spectroscopy. $I_{SERS}(\lambda_R)$ and $I_{SEIRA}(\lambda_0)$ are the intensity of the collected Raman and IR absorption signals respectively. $\lambda_R$ is the wavelength of the Raman signal. $N_1$ is the number of efficiently excited molecules. b) Antenna enhanced SERS and SEIRA spectroscopy. One monolayer of molecules is deposited on top of a resonant structure laying on top of a transparent substrate. The antenna and the molecules are then excited with light of wavelength $\lambda_0$ (visible for Raman spectroscopy and IR for absorption spectroscopy. $E_{NF}$ is the enhanced near-field at the extremities of the antenna. $E_{NF}$ can be about two orders of magnitude greater that $E_0$ in a standard situation. $N_2$ is the number of efficiently excited molecules.

wavelength of the incoming field and $\lambda_R$ the wavelength of the outgoing field.

As a rough approximation, it can be considered that $\lambda_R - \lambda_0 << \lambda_0$. Then $E_{local}(\lambda_R) \sim E_{local}(\lambda_0)$ and the enhancing factor for SERS can be approximated as the fourth power of the local field enhancement around the particles.

$$M_{SERS} \sim \left| \frac{E_{local}(\lambda_0)}{E_0(\lambda_0)} \right|^4 \tag{2.2}$$

The field enhancement is a local magnitude that depends on the particular point of evaluation. The calculation of the Raman enhancement by an ensemble of molecules distributed over an extended area of a nanoastrucutre would require an integration over all positions to obtain the average enhancement.

In the case of SEIRA the nanoantenna effect will act once. Being this spectroscopy based on an absorption process the is no re-radiation of any photons. Therefore, the enhancing factor fin SEIRA configurations can be expressed as,

$$M_{SEIRA} = \left| \frac{E_{local}(\lambda_0)}{E_0(\lambda_0)} \right|^2 \tag{2.3}$$

Even if the enhancement factors for SEIRA are less spectacular than the ones that can be achieved for SERS, in this chapter we will show that the effect of the resonant coupling of an individual plasmonic infrared nanoantenna with the vibrational excitation of the molecules gives rise to a different type of resonant SEIRA with unprecedented signal enhancement of five orders of magnitude, which means attomol sensitivity.

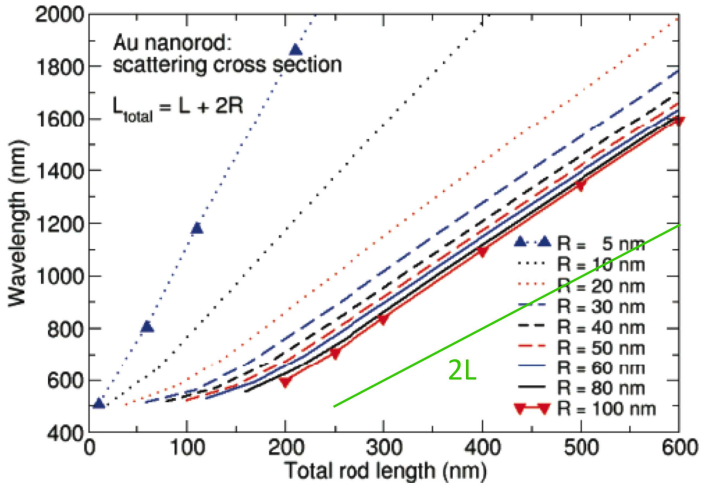


Figure 2.2: Chart showing the dependence of the dipolar resonance wavelength on $L_{tot}$ for different R. Resonance wavelengths were extracted from far-field scattering calculations. Adapted from [15]

## 2.1 Antenna design

We first focus on the design of the antenna configuration that will produce antennaa resonances at eht spectral position of the vibrational fingerprints. We focus on metallic rods made of gold that hold modified $\lambda/2$ dipolar resonances. To achieve a completely resonant situation, the length and width of the nanoantenna have to be tailored to hold a plasmonic resonance exactly matching the spectral position of the vibrational fingerprints. As it was already explained on Section 1.4, due to the finite negative dielectric value of the dielectric response of gold in the IR, antenna resonant wavelengths $\lambda_r$ result to be shifted compared to the ideal case, *i.e.* antenna resonances in the $\mu m$ range of the spectrum appear at slightly shorter lengths $L$ than the ideal half-wave dipole antenna length: $L < \lambda_r/2$. [15, 33–35] Fig. 2.2 shows a chart with the different dipolar resonances of gold nanoantennas for different lenghts (L) and widths (w) embedded in vacuum. The presence of a substrate also modifies the position of the resonances.

In our case, an antenna of about 1.5 $\mu$m length and 100 nm width, embedded on an

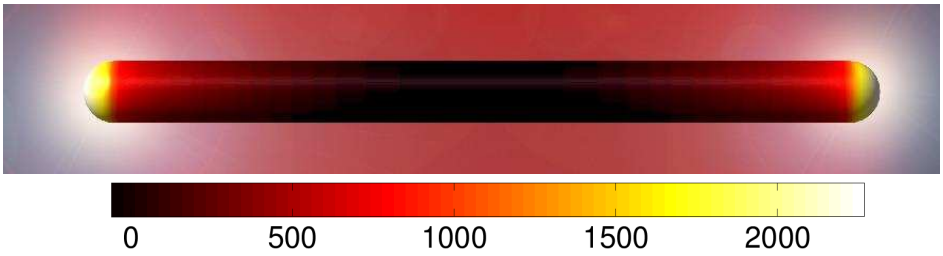


Figure 2.3: Calculation of the near-field intensity 1 nm above the surface of a gold nanowire (in vacuum, length $L = 1.31\mu m$, diameter $D = 100nm$) at the fundamental antenna resonance ($\lambda_r = 3.41\mu m$). The color scale indicates the magnitude of the enhancement from bright at the wire ends (maximum enhancement) to dark in the middle of the wire (lower enhancement).

effective medium that accounts for the substrate polarizabilty ($n_{eff}$= 1.22) resonates at the frequency of the vibrational lines of the molecules that we will want to study. Fig. 2.3 depicts the calculated enhancement of the near-field electromagnetic intensity around such a nanoantenna (length L = 1.31 $\mu$m) at its fundamental dipole-like resonance wavelength ($\lambda_r \approx 2.6$L). The infrared plasmon field of the antenna resonance produces an exceptionally large intensity enhancement at the antenna ends. [36] In our case, this intensity is mainly localized at nanometer distance from the antenna ends and can reach up to four orders of magnitude, as theoretically determined and indicated in Fig. 2.3. This enhancement is quite general in this type of configurations.

It is possible to use this localized IR field to enhance the spectral signature of molecular vibrations. Experimentally one layer of octadecanthiol (ODT, $CH_3(CH_2)_{16}CH_2SH$) was used as model adsorbate. ODT molecules can be were adsorbed on individual gold NWs (see Fig 2.4) and the IR transmittance can be measured with an IR-micro spectroscopy set-up [33]. The long-chained ODT molecules form a self-assembled monolayer (SAM) with the molecular axis slightly inclined with respect to the surface normal [37] (see Fig 2.4). The layer has a homogeneous thickness of 2.4 nm. [38] ODT exhibits several IR active vibration modes in the 3 $\mu m$ wavelength range. For our investi-

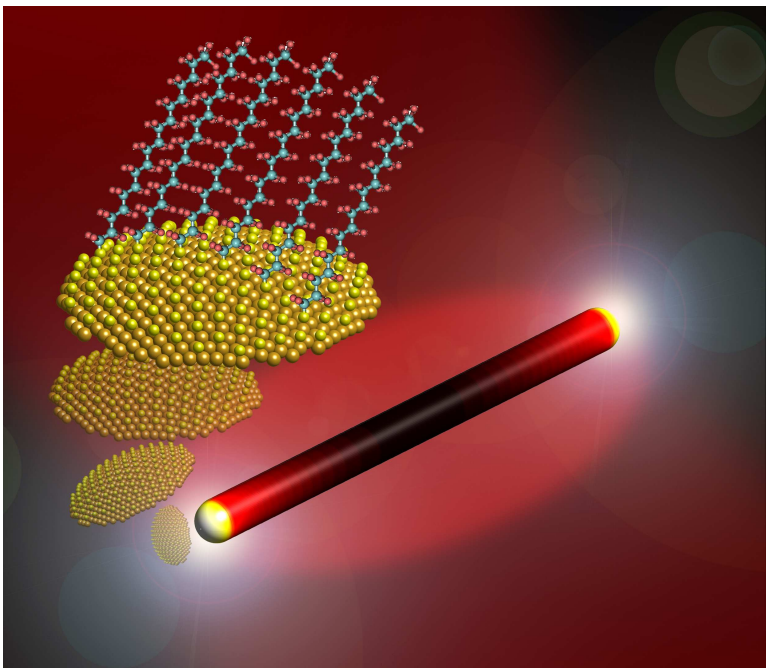

Figure 2.4: Sketch of the concept. A monolayer of ODT is adsorbed on top of an individual gold nanoantenna. The IR transmittance is measured with an IR-micro spectroscopy set-up.

gation, the strongest absorption modes of the $CH_2$ group antisymmetric (2916-2936 $cm^{-1}$) and symmetric (2850-2863 $cm^{-1}$) stretching vibrations [39] are considered, as obtained from infrared reflection absorption spectroscopy (IRRAS) of bulk ODT, with the identification of the corresponding modes as shown in Fig. 2.5 .

## 2.2 Antenna-vibrational coupling

In order to study the antenna-molecule configuration, we perform a set of simulations of the system where the full electromagnetic interaction of the antenna and the ODT layer is considered. The calculations were performed by means of the boundary element method (BEM) [40,41] to solve Maxwell's equations exactly for the scattering of a gold nanoantenna covered with a molecular layer. We use IR bulk dielectric functions to

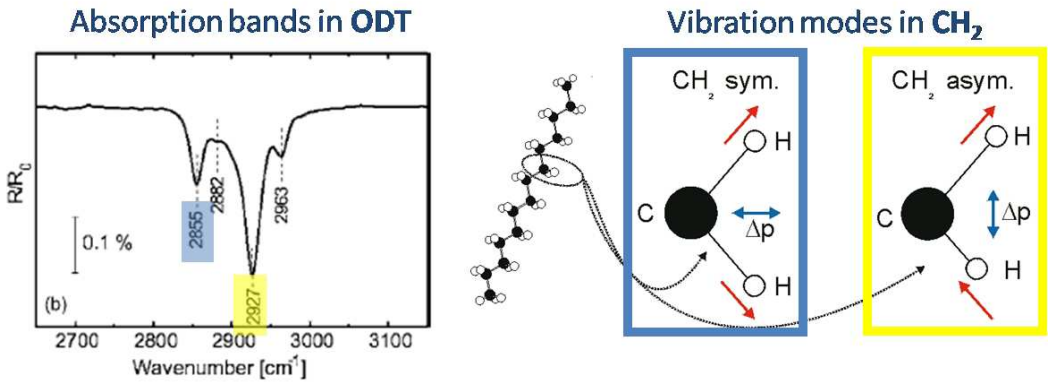


Figure 2.5: Infrared reflection spectroscopy ($R/R_o$) of bulk octadecanthiol, showing the main absorption peaks. The main vibrational modes are identified in the schematics to the right (blue: symmetric mode, yellow: antisymmetric mode)

characterize the response of gold, [16] and a Lorentz oscillator model with a dielectric background to characterize the vibrational response of the ODT layer:

$$\varepsilon(\omega) = \varepsilon_\infty + \sum_{j=1}^{4} \frac{\omega_{strength,j}^2}{\omega_{res,j}^2 - \omega^2 - i\omega\gamma_j} \tag{2.4}$$

where we assume 4 modes ($j = 1, ..., 4$), $\varepsilon_\infty = 1$ is the dielectric background, $\omega_{strength}$ is the oscillator strength, $\gamma_j$ is the damping of the $j$ mode and $\omega_{res}$ is the resonance frequency. In this case the oscillator parameters were obtained from a fit to the experimental IRRAS [42] presented in Fig. 2.5, and the parameters with the corresponding dielectric function for ODT assumed in our calculations are shown in Fig. 2.6.

The results for the extinction cross section of an ODT-covered nanoantenna using oscillator strength parameters from an IRRAS fit with the background value $\varepsilon_b = 1$ are shown in Fig. 2.7. A significant vibrational contrast is reached only for a relative thick ODT layer. A similar contrast in theory and experiment would be obtained for a single monolayer with ODT oscillator parameters that were calculated from IRRAS assuming a higher $\varepsilon_b$. This points to an interesting physical phenomenon at metal

**ODT vibrational parameters**

| Vibration mode | Resonance frequency $\omega_{res}$ [cm$^{-1}$] | Damping $\gamma$ [cm$^{-1}$] | Strength $\omega_{res}$ |
|---|---|---|---|
| $CH_2$ Symmetric stretch | 2855 | 14.53 | 20.65 |
| $CH_3$ Symmetric stretch | 2882 | 41.54 | 18.84 |
| $CH_2$ Antisymmetric stretch | 2927 | 25.02 | 41.18 |
| $CH_3$ Symmetric stretch | 2963 | 11.45 | 12.03 |

**ODT dielectric function**

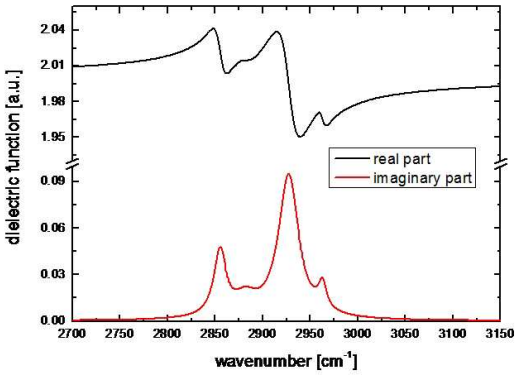


Figure 2.6: (Left) Set of parameters (resonance frequency, damping and oscillator strength) obtained to fit the IRRAS spectra of Fig. 2.5. (Right) Model dielectric function characterizing the ODT used in the model calculations.

interfaces. The anisotropy of the molecular monolayer does not significantly modify the contrast obtained with the use of an isotropic dielectric function. Also the detailed antenna end shape (semi-spherical or more flat) does not give significant effect on the IR resonance. Chemical effects as dynamic charge transfer [43, 44] can be excluded to have any relevance for the measured response, because the $CH_2$ groups producing the signal are not directly bound to the gold.

Fig. 2.7 shows relative extinction cross sections for individual gold NWs of different lengths covered with a layer of ODT. As observed in the spectra, the good match of the antenna resonance to the C-H stretching vibration lines is crucial for the appearance of the vibrational signal. The vibrational signal slightly decays as the resonance is slowly detuned (for L=1.38 $\mu$m, and L= 1.22 $\mu$m), and cannot be detected for the strongly detuned case (Fig. 2.7, curve for an antenna with L = 1.7 $\mu$m ). For electric field perpendicular to the wire no vibrational lines could be observed.

Interestingly, the lineshape of the vibrational signal clearly differs from a typical Lorentzian absorption band. Lineshape changes are known, *e.g.* from SEIRA on metal-

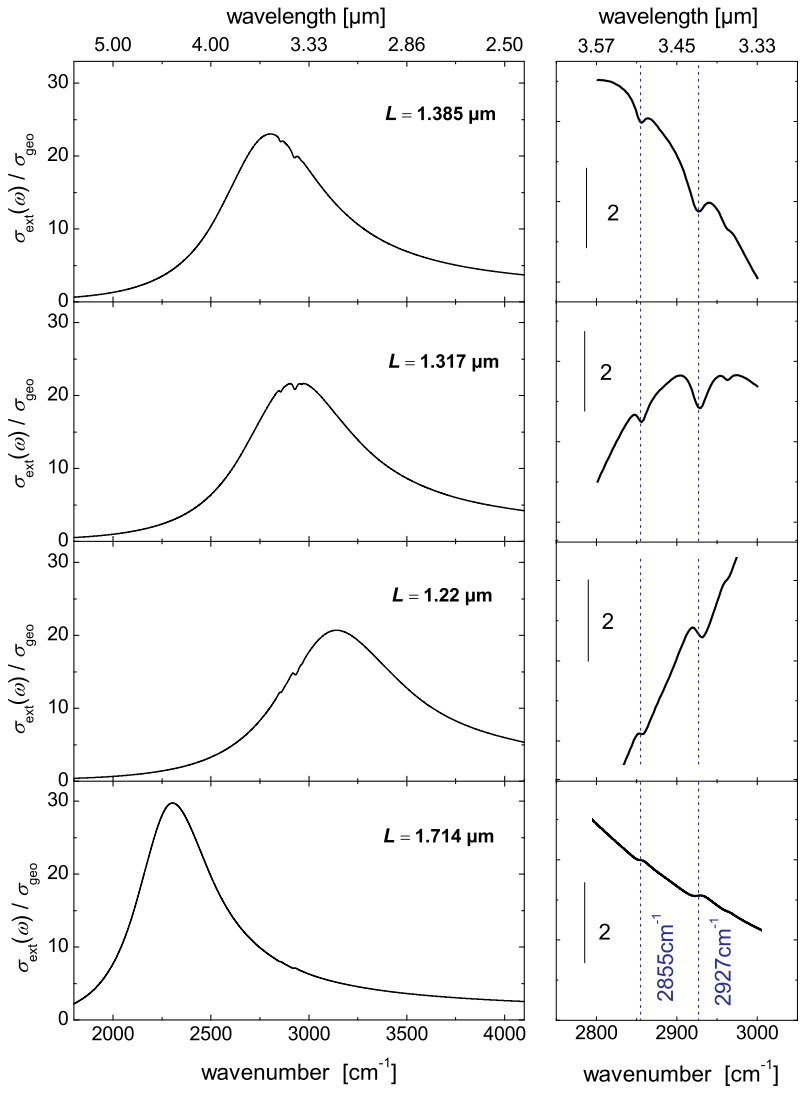


Figure 2.7: Calculated optical extinction $\sigma_{ext}$ normalized to the geometrical cross section $\sigma_{geom}$ for gold wires with $D = 100$ nm, covered with 100 nm ODT layer, for the antenna lengths $L$ indicated in the insets, and surrounded by vacuum. The BEM calculations are performed for polarization along the long wire axis. To the right, zoom into the vibrational bands. ODT vibrational frequencies on smooth gold surface are marked with dotted lines. Lineshape modification is observed as the plasmonic antenna is detuned.

island films where the asymmetry of the vibration signal is related to the spectral shape of the plasmon response of the metal-particle ensemble. [45, 46] In this study, the lineshape of the adsorbate signal results from an interaction between the electromagnetic field from the antenna resonance and the spectrally much narrower field associated with the vibrational dipoles of the molecules. The spectral shift for different nanoantennae produces differences in the coupling that transform the spectral lineshape accordingly. This situation is a clear analogy to the quantum mechanical interaction between a discrete state and a continuum of states producing Fano profiles. [47] Depending whether the antenna resonance and the vibrations are exactly matching or not, the Fano-type profile goes from a dip to an asymmetric lineshape, respectively.

As shown in Fig. 2.7, the overall extinction cross section produced by the antenna for an exactly resonant situation ($L = 1.317\mu m$) shows several dips, *i.e.* zones of smaller extinction at the vibration frequencies, which can be interpreted as a result of an antiphase interaction of both kinds of excitation (vibrational and plasmonic). The dips in the spectrum corresponds to a resonant situation where the interaction between the broadband and narrowband resonances is maximum, therefore producing a Fano-like antiresonance (dip), whereas a more asymmetric Fano-like profile is obtained as we depart from resonance (weaker interaction). [20, 47] Note that the sign of the derivative of the asymmetric lineshape profiles depend on the energy location of the antenna resonance to with respect to the vibrational energies of the molecules.

## 2.3 Experimental evidence:

IR micro-spectroscopy of individual gold nanowires has been experimentally performed by Annamarie Pucci's group in Heidelberg University performed at the IR beamline of the synchrotron light source ANKA (Angströmsource Karlsruhe) at the Forschungszen-

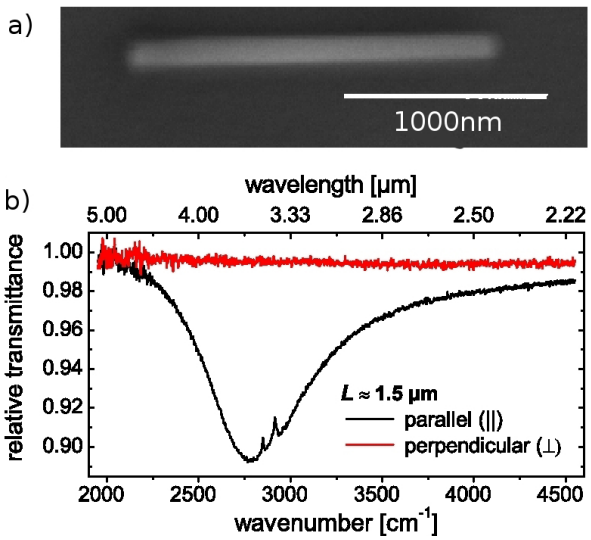


Figure 2.8: (a) Scanning electron micrograph of a gold wire with similar dimensions as used in this study. (b) Relative IR transmittance in the spectral region of the fundamental resonance of a gold wire with one ODT monolayer for parallel ($\|$) and perpendicular polarization ($\perp$). A $CaF_2$ substrate is used. The broadband plasmonic resonance is observed around $\lambda_r \approx 3.6\mu m(\|)$. Data obtained by Prof. Pucci's group at the University of Heidelberg.

trum Karlsruhe. [33] The probe-area diameter of the spectroscopy experiment was of 8 $\mu m$. The wires (diameter $D = 100$ nm, prepared by electrochemical deposition in etched ion-track membranes, supported by a transparent substrate) consist of only a few crystalline grains and their tip shape results from a relative smooth grain boundary. [48] The IR transmittance spectrum (at normal incidence, divided by the spectrum of the bare substrate) of an individual metal NW prepared with a length of a few microns (see Fig. 2.8(a)) shows a broad plasmonic feature for parallel ($\|$) polarization of the IR radiation, associated with the fundamental half-wave dipole-like antenna mode (see Fig. 2.8(b)). This resonance, also known as the longitudinal fundamental plasmonic mode, is suppressed for perpendicular polarization ($\perp$) of the incoming IR radiation (red line in Fig. 2.8(b)) and the respective transmittance change to the bare substrate is not detected.

For ideal antennas on a substrate, the wavelength $\lambda_r$ of the fundamental antenna resonance of a wire with length $L$ and diameter $D << L$ can be roughly approximated with the relation $\lambda_r/n_{eff} = 2L$ using an effective refractive index $n_{eff}$ that accounts for the substrate polarizability. [33] As pointed out in the introduction, the exact wavelength of the plasmon resonance in vacuum is furthermore shifted due to the non-perfect perfect conductive nature of gold at IR frequencies, the actual aspect ratio and the non-neglegible skin depth compared to the diameter of the NW, thus, in our case, an about 1.5 $\mu m$ long nanoantenna on $CaF_2$ ( $n_{eff}$= 1.22 ) shows the resonant peak at $\lambda_r \approx$ 3590 nm (2800 $cm^{-1}$), in agreement with full electromagnetic calculations [15,33].

The extinction cross section of the individual wire obtained from the broad feature of reduced intensity in the transmittance curve in Fig. 2.8(b) turned out to be enhanced with respect to the geometrical cross section, which clearly indicates the activation of an intense nearfield in the vicinity of the wire (simple shadowing does not give a measurable transmittance change). The experimental cross section ratio calculated here is a far-field result and represents an average value over a large interval of distances from the wire surface.

The resonant coupling between the fundamental NW resonance and the ODT bands was studied for NWs with different lengths, *i.e.* resonance frequencies showing different spectral shifts with respect to the $CH_2$ frequencies from the ODT. The experimental results are shown on Fig. 2.9: For an antenna resonantly matching its plasmonic broadband resonance with vibrational narrowbands of molecules (L=4 $\mu$m in Fig. 2.9), maximum contrast is obtained with strong dips in the spectrum. These antiresonance features appear exactly at the vibration frequencies. As mentioned above, as the length of the antennae is increased or reduced, the broadband plasmonic resonance is spectrally shifted to the red or to the blue with respect to the vibrations, producing a change in the phase interaction (modification of the coupling strength in terms of Fano

interaction) and progressively decreasing vibrational signals with clearly asymmetric profiles. These experimental lineshapes correspond to Fano-like profiles of intermediate interaction described in the previous section. The asymmetry of the lineshapes is reversed when the broadband plasmonic resonance is located to the right or to the left of the vibrations. For a completely detuned antenna (L=1.7 $\mu$m), the asymmetric vibrational contrast is almost vanished, in agreement with the theoretical calculations.

The vibration signal is increased up to 1%, as derived from the difference between maximum and minimum transmittance of the vibration feature. By comparison to IR reflection absorption spectra (IRRAS) from a SAM of ODT on a smooth gold surface [26] the vibration signal size for the best match turns out to be about 330000 times bigger than it would be for the same amount of molecules directly on the substrate (without antenna). It is important to note that the signal comes mainly from the area of the tip-ends of the NW, where the strongest field enhancement is produced (see Fig.2.3), corresponding to about 150 000 molecules (less than one attomol). This enhancement results in an increment of 5 orders of magnitude in sensitivity compared to previous state of the art sensitivity within SEIRA configurations setting up a new approach in the field of molecular sensing.

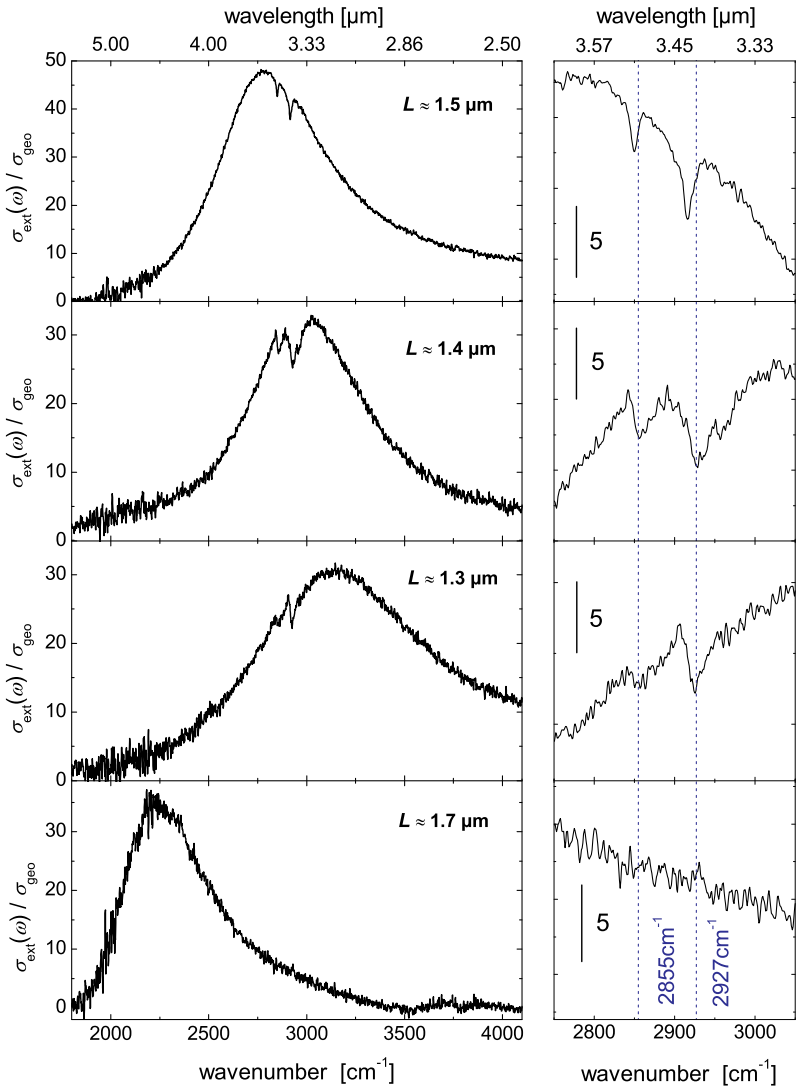


Figure 2.9: Experimental extinction-cross sections $\sigma_{ext}$ (normalized to the geometrical cross section $\sigma_{geo}$) for four ODT-coated wires with different lengths $L$ (as indicated in the insets, $D = 100$ nm) on a $CaF_2$ substrate. The spectra are obtained from IR [33] with a noise level that slightly varied depending on the incoming IR intensity. To the right, the zoom to the vibrational signals. The ODT vibration frequencies on a smooth gold surface [26] are marked with dotted lines. Maximum contrast is obtained for resonant coupling. Curves obtained by Prof. Pucci's group at the University of Heidelberg

# CHAPTER 3

# PLASMONIC CONCAVE/CONVEX SURFACES FOR FIELD-ENHANCEMENT: THE PLASMONIC INDENTED NANOCONE

Designing and engineering effective near-field scanning plasmonic nanostructures is a challenging topic of research to improve field-enhanced microscopy and spectroscopy. Different structures, mainly based on the coupling between metallic nanoparticles (interparticle coupling) creating electromagnetic hot spots, such as dimers [49] or plasmonic lenses [50], have been proposed and adopted to obtain very large field enhancements of up to 1000 times the incident electromagnetic field amplitude. These huge enhancements are required to push the limits of detection and specificity in molecular spectroscopies [4] [18] and biosensing [51, 52]. With regard to field-enhancements produced by isolated nanostructures, the results are less spectacular. Usually, field-enhancements of 10 times in amplitude are obtained in these cases.

Electromagnetic field enhancement in the proximity of metallic surfaces is an intrinsic property of surface plasmons excited at the surfaces at certain resonant frequencies.

This enhancement is a consequence of the localization of the fields in the transversal direction at the perpendicular metal-dielectric interface. Further field localization of the fields in the parallel direction of the interface can be typically achieved by means of modifications of the geometry of the surfaces or by coupling with other structures. Actually, the strong dependence of the optical response on the characteristics of the particular geometry and the coupling make the optimization of the field enhancement a challenging task in nanooptics. We summarize in the next section the most relevant effects that lead to an increase of the field-enhancement. Some of the effects cannot be isolated, and very often different effects are expressed jointly, however, it is useful to identify them here separately for conceptual clarity. We will apply and explain later how these effects merge and assist to obtain field enhancements of 3 orders of magnitude. The results of the optical response of the different nanostructures, both in the far-field and in the near-field are obtained with use of the Boundary Element Method (BEM) to solve Maxwell's equations. The details of this calculation method are summarized in Appendix A.

## 3.1 Ingredients of the field enhancement

To gain insights about the nature of each effect we willsupport our numerical calculations with results from a simpler non-retarded analytical model. Let us assume the generic polarizability tensor $\alpha_{jj}$ of an ellipsoidal particle (P) of volume V in a medium (M) [53]:

$$\alpha_{jj}(\omega) = \frac{V\varepsilon_0}{L_j}\frac{\varepsilon_p(\omega) - \varepsilon_M(\omega)}{\varepsilon_p(\omega) - \varepsilon_M(\omega) + \varepsilon_M(\omega)/L_j} = \alpha_0 f(\omega) \tag{3.1}$$

where $\varepsilon_p/\varepsilon_M/\varepsilon_0$ are the dielectric functions of the particle/medium/vacuum respectively, and Lj is the so called depolarization factor, corresponding to the direction of

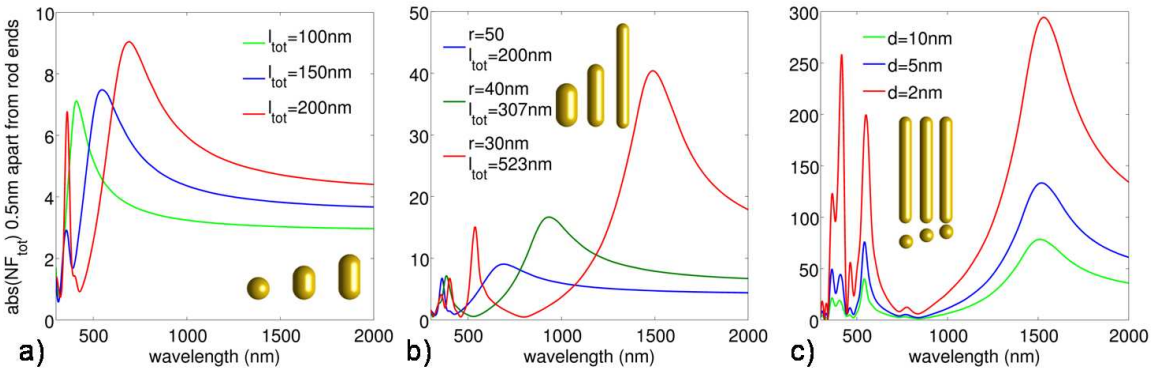


Figure 3.1: Evolution of the near-field amplitude spectra 1 nm above the surface of one of the extremities of a silver nanorod (in vacuum), when changing different parameters of the system. a) Volume: Modification of the length and volume of the system. b) Sharpness: Modification of the length keeping the volume of the system constant. c) Coupling: System composed of a rod and a sphere, modifying the separation distance between the rod and the sphere.

the component j of the applied field that only depends on the shape of the particle.

For illustration purposes we will use a Drude dielectric function for the metal particle within the non-retarded analytical model.

$$\varepsilon_p = 1 - \frac{\omega_p^2}{\omega(\omega + i\Gamma)} \tag{3.2}$$

being $\omega_p$ the bulk plasma frequency of the metal and $\Gamma$ the Drude damping. For the surrounding medium $\varepsilon_0 = 1$. The field enhancement (when large) is proportional to the absolute value of $\alpha$. Linearizing around the peak value Eq. 3.1, the field enhancement can be expressed as:

$$E \propto \frac{V\varepsilon_0}{L_j} \frac{\sqrt{L_j}/2}{[(\sqrt{L_j} - \Omega)^2 + (\Gamma'/2)^2]^{1/2})} \tag{3.3}$$

where $\Omega = \omega/\omega_p$ and $\Gamma' = \Gamma/\omega_p$. Separating the static polarizability prefactor and the resonant part with resonance frequency $\omega_p\sqrt{L_j}$, notice that the enhancement depends on both the shape of the object through $L_j$ as well as the characteristic length scale of the object related to $V$, as we will now describe in more detail.

*Size effects:* The field enhancement achieved through the excitation of surface plasmons is a direct consequence of the induced surface charge density spread over the supporting surface geometry. Enlarging the volume of a nanostructure produces an increment on the induced charge density on the system, thus increasing the oscillator strength of the induced dipoles and therefore the local field enhancement associated with the larger accumulation of surface charge. This effect enters naturally through the presence of the volume V of the particle in Eq. 3.1. We show this effect in Fig. 3.1a, where we calculate the near-field spectra in the proximity of silver nanorods of different size 1 nm away from the edge of the nanorods. It is clear how the maximum field enhancement is increased as the length of the nanorod is increased.

*Lightning rod effect:* The field enhancement obtained by enhancing the volume of the structure can still be increased through further localization of the near-field response with the use of sharper geometry ends that produce even larger localized near-field responses. The reason behind this effect relies on the lightning rod effect. Large variations of the surface curvature produce a large potential gradient in a very reduced area, therefore large field values, very concentrated at the sharp area, are produced.

The static polarizability $\alpha_0 = \frac{V\varepsilon_0}{L_j}$ contains the lightning rod effect in terms of the depolarization factor $L_j$ in the denominator. That is, as the shape of the object gets sharper, which for the prolate spheroid happens when the major axis $a$ is much larger than the minor axis $b = c$, the static polarizability increases accordingly. As the spheroid becomes more elongated along the $j$ direction, as shown in Fig. 3.1b, $L_j$ approaches zero. For a prolate ellipsoid the depolarization factor $L_j$ can be expressed as: [54]

$$L_a \approx \frac{b^2c^2}{a^2b^2 + a^2c^2 + b^2c^2} \tag{3.4}$$

When written in this form, it is helpful to connect the depolarization factor with a well-defined measure of the sharpness of a surface, i.e. its curvature. For a surface with principal radii of curvature, $\rho_1$ and $\rho_2$, at a regular point of a surface we can define the mean curvature $H = \frac{1}{2}(\frac{1}{\rho_1} + \frac{1}{\rho_2})$ and the Gaussian, or total, curvature $K = \frac{1}{\rho_1 \rho_2}$ at that point.

We can now express the depolarization $L_a$ of Eq. 3.4 in terms of the Gaussian curvature $K_{a,b,c}$ at the endpoints of the ellipsoid in the direction of the coordinate axes.

$$L_a \approx \frac{a^2/K_a}{a^2/K_a + b^2/K_b + c^2 K_c} \tag{3.5}$$

For a very elongated ellipsoid $K_a = (\frac{a}{bc})^2 \gg K_{b,c}$, and we can write:

$$L_a \approx \frac{1}{2b^2 K_a} \tag{3.6}$$

Hence we can express the enhancement from the lightning rod effect as being directly proportional to the Gaussian curvature.

We show now this effect in Fig. 3.1b, by modifying the thickness of one rod, making it sharper. To avoid a reduction of the global induced charge density on the structure, we elongate the rod and transform it into a thinner or longer rod while mantaining the total volume of the structure constant. In this way, we avoid the interplay of volume effects in this description of the lightning rod effect. We can observe in the near-field spectra of Fig. 3.1b how the enhancement increases as the radius of one of the coupled rods decreases and thus the Gaussian curvature increases.

*Coupling:* Coupling of the electromagnetic response of a nanostructure to adjacent metallic systems is known to produce field localization and correspondingly enhancement of the near-field at the region in-between the structures [4, 14, 49, 55]. We show

in Fig. 3.1c this effect by coupling a 523 nm long silver rod with 30 nm rarius and a 30 nm radius silver sphere. We calculate the near-field 1nm below the rod's lower apex for different separation distances d (d=10 nm, 5 nm and 2 nm). An increase of the near-field maximum can be observed as the separation distance becomes smaller. This effect is connected with the appearance of a coupled bonding plasmon that belongs to the whole system arising from the symmetric coupling of the dipolar plasmons of each nanostructure. [56] Tipically, by means of this effect, the amplitude of the field enhancement can be increased about an order of magnitude with respect to that of the isolated systems [55]. It is interesting to note how in this case, the spectral response is not red shifted when the particles are approached as it could be expected. Being the sphere much smaller than the rod, even if the local near-field response is coupled, the rod dominates the spectral response of the system for the separation distances considered, thus making the expected red shift due to the coupling between the structures negligible.

Some optimization strategies based on a combination of some or all of these effects have been applied recently to obtain large field enhancements. We can cite among others the case of bowtie antennas [57], where a combination of interparticle coupling and sharp ends produce large enhancements in the plasmonic antenna gap, or the case of the plasmonic lense [50] where three particles of different size are brought together combining effects of size, coupling and sharpness of the structures to produce huge field enhancements. All these studies suggest the use of discrete structures to obtain the enhancing effect. In this chapter we propose the use of a continuous structure based on a metallic cone where we will induce size effects, coupling effects, and lightning rod effects by means of the presence of concave and covex deformations of the surfaces at the metallic apex of the cone. We call this structure a plasmonic indented nanocone. The alternation of concave and convex surface deformations force alternating changes

in the sign of the surface charge density that are the equivalent to those produced in the coupling of discrete nanostructures, leading to an increase of the electric field, providing similar enhancing power.

## 3.2 Plasmonic indented nanocone

We introduce in this section a novel nanostructure that merges simultaneously all the concepts mentioned above in a single conitous nanostructure: an indented nanoconical tip. We will consider that the structure is mad of silver. We will assume dielectric data from the literature to characterize the optical response. [16]

In this situation, a big metallic cone acts as a surface charge density reservoir that can localize very efficiently part of that surface charge at the cone apex [58]. Fig. 3.2a shows the optical extinction cross section of a single cone of aperture angle of $30^o$ and radius of curvature of 10 nm. Fig. 3.2b shows the NF spectra of the structure 1nm below the cone apex. W observe that the highest NF enhancement for such a structure occurs at $\lambda = 379$ nm. The surface charge density associated with this localized plasmon mode and the near-field produced at the cone apex are shown in Fig.3.2c and Fig. 3.2d respectively. Field enhancements of around 60 times the field amplitude can be obtained in the proximity of this conical structure with use of a realistic radius of curvature for the cone apex of the order of 10 nm.

The typical enhancement produced at a standard metallic cone apex can be further optimized by engineering the induced charge density profile on the structure. Optical properties in metallic edged (concave) and wedged (convex) geometries offer the possibility to modify the symmetry of the surface charge density of the lowest plasmonic modes [59]. A concave surface presents a symmetric profile for the surface charge density piling up charge at the edge whereas a wedge structure (complementary geometry)

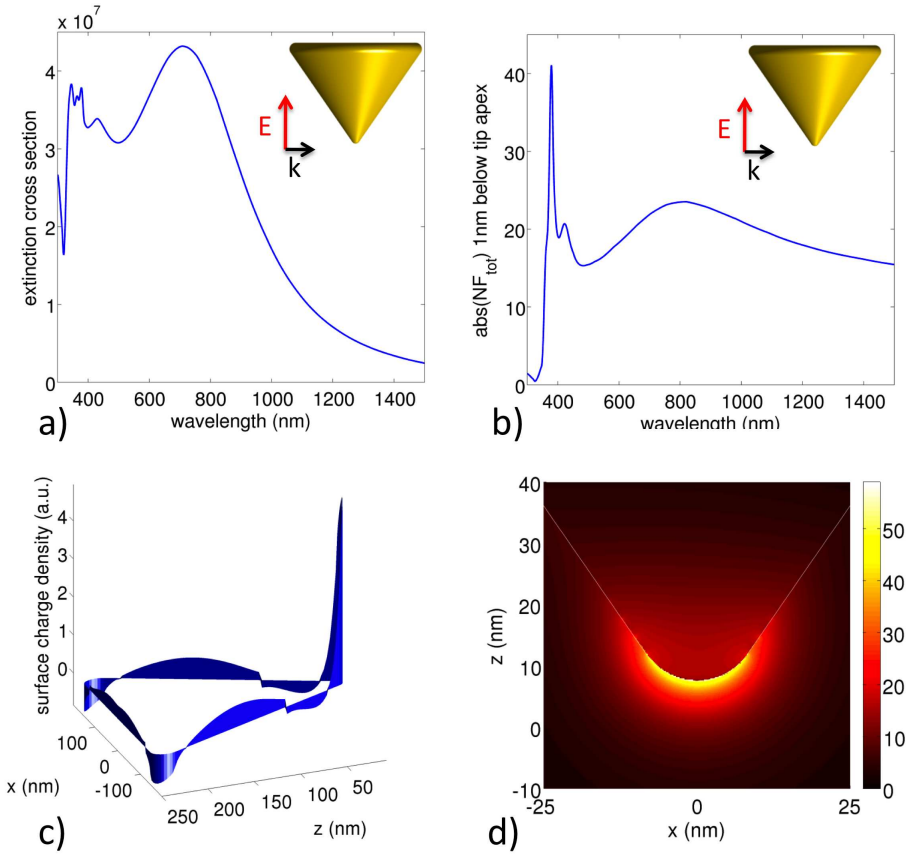


Figure 3.2: a) Extinction cross section of a silver cone with incident light as displayed in the inset. b) Near-field spectra of a silver cone calculated 1nm bellow the cone appex. c) Surface charge density profile of the cone for $\lambda = 379$ nm d) Near-field distribution of the cone for normal incident light of $\lambda = 379$ nm polarized along the cone axis.

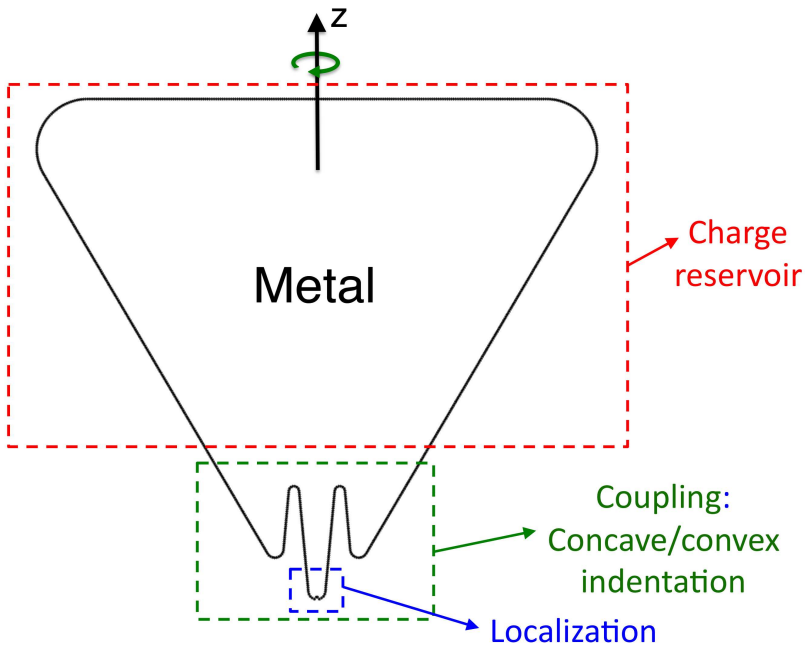


Figure 3.3: Cross section of the geometry of the plasmonic indented nanocone. The combination of the three field enhancement ingredients (a big surface charge reservoir, the localization of the charge density at the edges and the coupling of plasmons), permits the creation of a filed enhancement of $\approx 800$ at the tip apex (see Fig. 3.4)

produces an antisymmetric profile of the surface charge density producing a node of the charge at the wedge.

The combination of a concave and convex surface inevitably produces a change of the sign of the surface charge density at one type of surface with respect to the other for the lowest energy mode. This produces a dipolar coupled mode where the node of the dipole is located at the wedge.

It is possible to create in this way areas where the surface charge density is forced to change sign and oscillate in antiphase within the same continuous structure. A structure of concave and convex surfaces would permit to exploit both the aspect of localization due to the presence of the edges and wedges, as well as the aspect of coupling in the same closed geometry. Furthermore, the symmetry of the convex

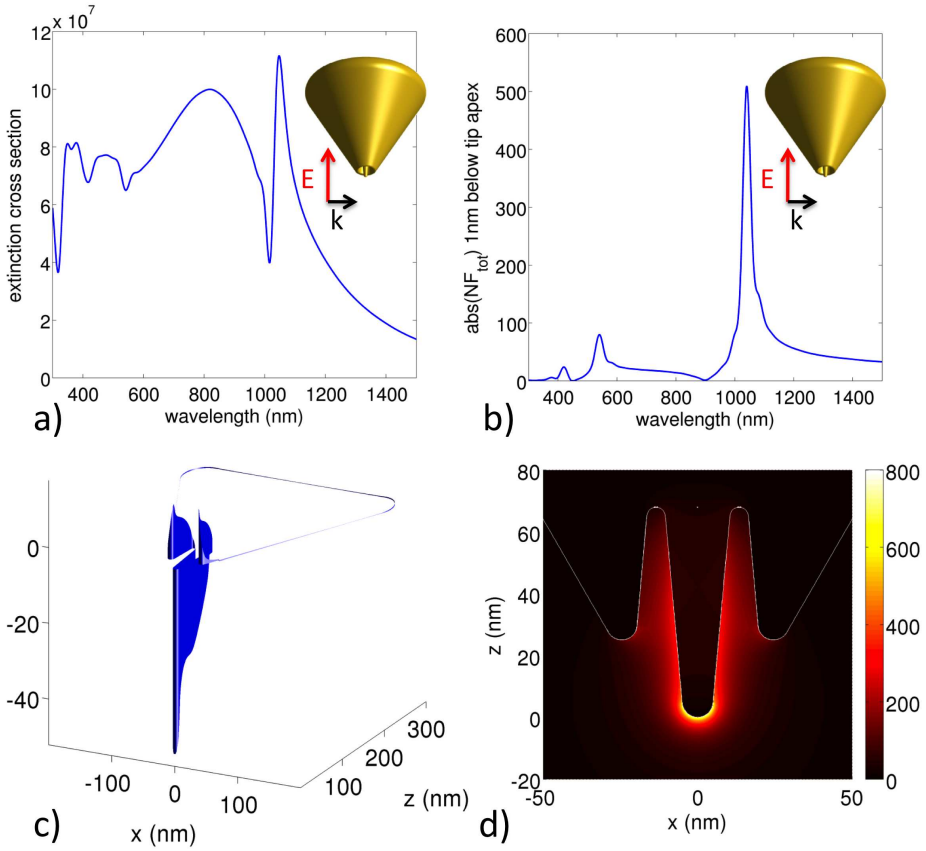


Figure 3.4: a) Extinction cross section of a silver indented nanocone. b) Near-field spectra of a silver indented nanocone calculated 1nm bellow the cone appex. c) Surface charge density profile of the indented nanocone for $\lambda = 1040nm$ d) Near-field distribution of the cone for normal incident light of $\lambda = 1040nm$ polarized along the cone axis.

surface, forcing a change of sing of the surface charge density is a key element for the enhancement, as we will show below.

A situation of coupling of concave and convex surfaces in the same continuous structure can be realized in a indented nanocone structure as the one presented in the inset of Fig. 3.4a and Fig. 3.3. This structure presents a geometry that combines the three necessary ingredients to maximize the field enhancement: (i) a big surface charge reservoir, (ii) localization of the charge density at the edges and (iii) coupling of plasmons in close proximity.

We show in Fig. 3.4a the optical extinction cross section of a silver indented nanocone. The far-field spectrum of the indented nanocone cone shows similarities in the low range of wavelengths (between 500 nm and 1000 nm) with that corresponding to the smooth cone presented on the inset of Fig. 3.4a. However, a new mode emerging at the near infrared (IR) range of the spectrum appears a predominant feature. This new mode is very intense and narrow and it seems natural to assign its emergence to the presence of the geometrical features of the indented nanocone. To confirm the nature of this new intense peak, we calculate the surface charge density at the peak position ($\lambda = 1040$ nm) and show it in Fig. 3.4c. As expected, the surface charge density is piled up on the concave zone of the geometry (indented nanocone arm) therefore the local fields show maximum value and localization in this area. At the convex area, at the indented nanocone wedges, a zero in the surface charge density is induced, as explained above, forcing the charge density to change sign and effectively acting as a source of polarization of the system. The role of the convex part of the indented nanocone is thus crucial to change sign with respect to the surface charge density at the indented nanocone arms, and therefore allows for a larger oscillation of the surface charge density to occur. The resulting near-field map corresponding to this mode is shown in fig. 3.4d for the resonant wavelength. A field-enhancement at the amplitude maximum of 800 is achieved for reasonable parameters of the arm length and their curvatures.

The reason for this huge enhancement does not rely on the sharp curvature of the subtip of the indented nanocone, as one intuitively could think in a first approach. Interestingly, calculations of the field enhancement for the small subtip of the indented nanocone (same curvature) only reach enhancements of the order of one order of magnitude in amplitude. It is the combination of all the ingredients mentioned in this work what makes this structure a unique continuous structure providing such enhancement.

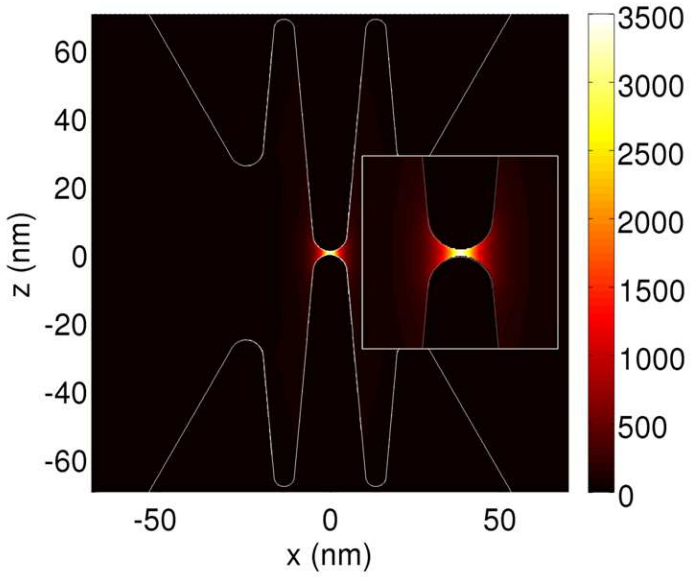


Figure 3.5: Near-field distribution of a system composed of two coupled indented nanocones separated by a distance of 2nm.

To some extent, this structure is the continuous analogous to a discrete plasmonic lense [50]. In a discrete case, we can find the presence of a relatively big particle (reservoir of surface charge density) together with the presence of a smaller particle (lighting rod effect) and finally the coupling of a third particle, providing a structure for the surface charge density to change sign, increasing the polarization and the surface charge density oscillation, thus the near-field associated. In the plasmonic lense, the presence of the third particle is key to provide the change of sign of the charge density. In our case, we unite the same ingredients in one single continuous structure where the reservoir of charge is provided by the cone, the concentration of charge is provided by the cone apex, and the polarization enhancement due to large oscillations and change of sing of the surface charge is due to the presence of concave/convex surfaces, the continuous analogous to the third particle in a plasmonic lense.

It is possible to go further in the enhancing strategy by providing an additional external coupling to this structure. To this end, we now locate two of these nanos-

tructures facing them with a small separation distance of 2 nm (Fig. 3.5). The extra coupling results in a final field enhancement of  3500.

In summary, we have reported key electromagnetic effects which can be used to optimize the near-field enhancement of a metallic nanostructure and applied these effects to design a single geometry where the field enhancement reaches easily the largest values reported in the literature, with field enhancement of 3 orders of magnitude in amplitude. Further modifications of this concept may lead to even larger factors. To obtain these enhancing factors appropriate values for the dielectric response and damping of the metals have been used as well as realistic parameters for the cone legths, curvatures and indentations. Therefore this type of structures could be experimentally realized in principle.

# CHAPTER 4

# NEAR-FIELD IMAGING OF PLASMONIC ANTENNAS

As it has been shown along this thesis, visible and IR resonant nanoantennas, being able to engineer the optical fields at the nanoscale, offer a basis for the development of a wide variety of new applications such as ultrasensitive molecular spectroscopy, high resolution microscopy or nanoscale optical circuitry. For the correct understanding and development of such technologies, it is crucial to achieve an adequate theoretical and experimental knowledge of the optical far-field and near-field response of the supporting devices. Experimentally, in spite of the general and straightforward techniques available to obtain information on the far-field radiation of nanoscale systems such as dark-field optical spectroscopy [60], the amplitude and phase of the near-field is still more than a challenge to access.

There exist several experimental methods such as two-photon induced luminescence (TPL) microscopy [34, 61, 62], electron energy loss spectroscopy (EELS) [63] and photoemission electron microscopy (PEEM) [64] that enable the mapping of near-fields with nanoscale resolution, but they provide only information about the amplitude of the local fields. However, in nanophotonics it is often the local near-field phase

that is of extreme importance, as for example in coherent control applications [65], in nanoantenna-assisted molecular emission [66] and spectroscopy [20], and in plasmon dynamics of complex metallic systems [67]. Scattering-type scanning near-field optical microscopy (s-SNOM) [21] has managed to map both the local amplitude and phase with wavelength-independent spatial resolution by interferometric detection of the antenna fields scattered by a scanning atomic force microscope tip [68–70].

This section aims to introduce a basic modeling for the scattering-type near-field microscopy technique. First, a simple and approximated theoretical model for the scanning process will be assumed to introduce the basic working principles. The limitations of the model will be discussed, and some of the details will be sophisticated as required by the complexity of the experimental configuration (background subtraction, tip geometry, tip-sample interaction, etc.).

The objective is to deduce the electric near-fields produced by an arbitrary object from the information extracted from the far-field. Experimentally, an Atomic Force Microscope (AFM) tip is employed as probe. Theoretically, we will describe the tip as a point electric dipole $\mathbf{p}$. As a first approach, we will assume that the probing dipole $\mathbf{p}$ acts as a passive scatterer and does not modify the optical response of the sample under study. The effects of the probe-sample interaction will be further studied in Section 4.2. On the other hand, in this first approximation, we will assume that it is possible to measure the far-field scattered exclusively of the dipole $\mathbf{p}$. Fig. 4.1 shows the main aspects of this framework.

In such an scenario, we can express this dipolar moment $\mathbf{p}$ as:

$$\mathbf{p} = p_x\hat{u_x} + p_y\hat{u_y} + p_z\hat{u_z} = [\alpha]\mathbf{E} = \begin{bmatrix} \alpha_x & 0 & 0 \\ 0 & \alpha_y & 0 \\ 0 & 0 & \alpha_z \end{bmatrix} \begin{bmatrix} E_x \\ E_y \\ E_z \end{bmatrix} = \alpha_x E_x\hat{u_x} + \alpha_y E_y\hat{u_y} + \alpha_z E_z\hat{u_z} \tag{4.1}$$

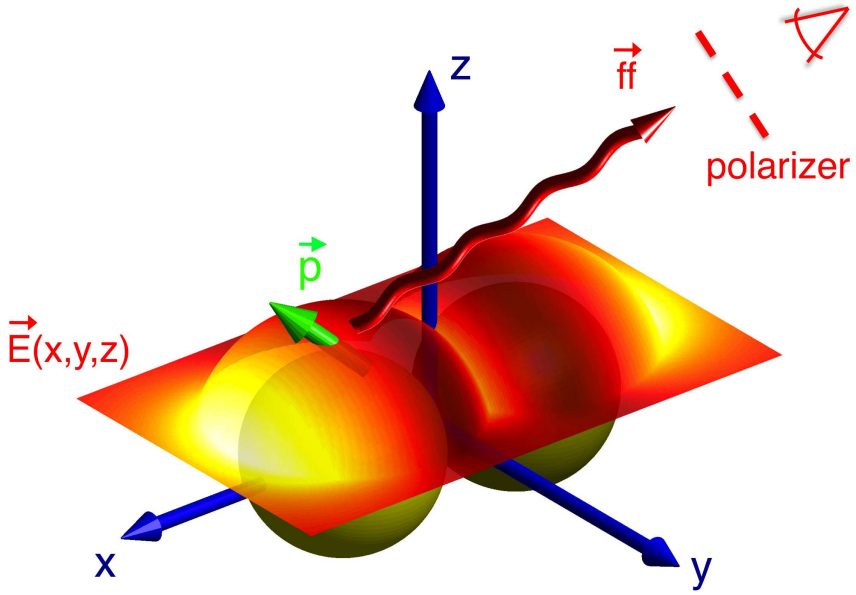


Figure 4.1: A weak electric point dipole of dipolar moment $\vec{p} \equiv \mathbf{p}$ scans the local electric fields $\vec{E}(x, y, z) \equiv \mathbf{E}(x, y, z)$ induced by an arbitrary sample. The dipole follows the topography of the system at a certain height. The far-field radiation of this dipole $\mathbf{f}f$ is collected in a certain direction after passing through a linear polarizer. Each polarization of $\vec{ff} \equiv \mathbf{f}f$ ($ff_\theta$ and $ff_\varphi$) contain the necessary information to reconstruct the near-field components of $\mathbf{E}(x, y, z)$ at the plane scanned by $\mathbf{p}$, under the assumption of weak interaction between the probing tip and sample.

where $\mathbf{E}$ is the vectorial local electric field induced by the sample at a certain position, $E_x$, $E_y$ and $E_z$ are the cartesian components of this field and $\alpha_x$, $\alpha_y$ and $\alpha_z$ are the components of the tip polarizability along the corresponding directions. $p_x$, $p_y$ and $p_z$ are the cartesian components of $\mathbf{p}$. $\hat{u}_x$, $\hat{u}_y$ and $\hat{u}_z$ are the unitary cartesian vectors.

The far-field amplitude $\mathbf{f}f$ of such a dipolar emitter can be expressed as [10]:

$$\mathbf{f}f \propto k \times \mathbf{p} \times \mathbf{k} \tag{4.2}$$

where $\mathbf{k}$ is the wavevector of the far-field radiation. If we express this far-field amplitude in spherical coordinates $(r, \theta, \varphi)$ we obtain:

$$ff_r = 0 \tag{4.3}$$

$$ff_\theta \propto p_x cos(\theta)cos(\varphi) + p_y cos(\theta)sin(\varphi) + p_z sin(\theta) \tag{4.4}$$

$$ff_\varphi \propto -p_x sin(\varphi) + p_y cos(\varphi) \tag{4.5}$$

Fig 4.2 presents a three-dimensional graphical representation of these equations in spherical coordinates for $\mathbf{p} = p_x\hat{u}_x$, $\mathbf{p} = p_y\hat{u}_y$ and $\mathbf{p} = p_z\hat{u}_z$. From this radiation patterns, it is possible to deduce how it would be possible to visualize the vectorial components of near-field from the far-field radiation of the probing dipole at certain directions.

For example, analyzing the far-field radiation of the dipoles for ($\theta = 90^o$, $\varphi = 0^o$) direction, we can deduce how the $ff_\theta$ polarization is only produced by the $p_z$ component of the dipole induced at the probe. Being $p_z = \alpha_z E_z$ and $\alpha_z$ a constant for the measuring process, the far-field radiation of the probe in this direction will be proportional to the $E_z$ component of the near-field. Thus, it would be possible to visualize the near-field pattern of this component by scanning the probing dipole over

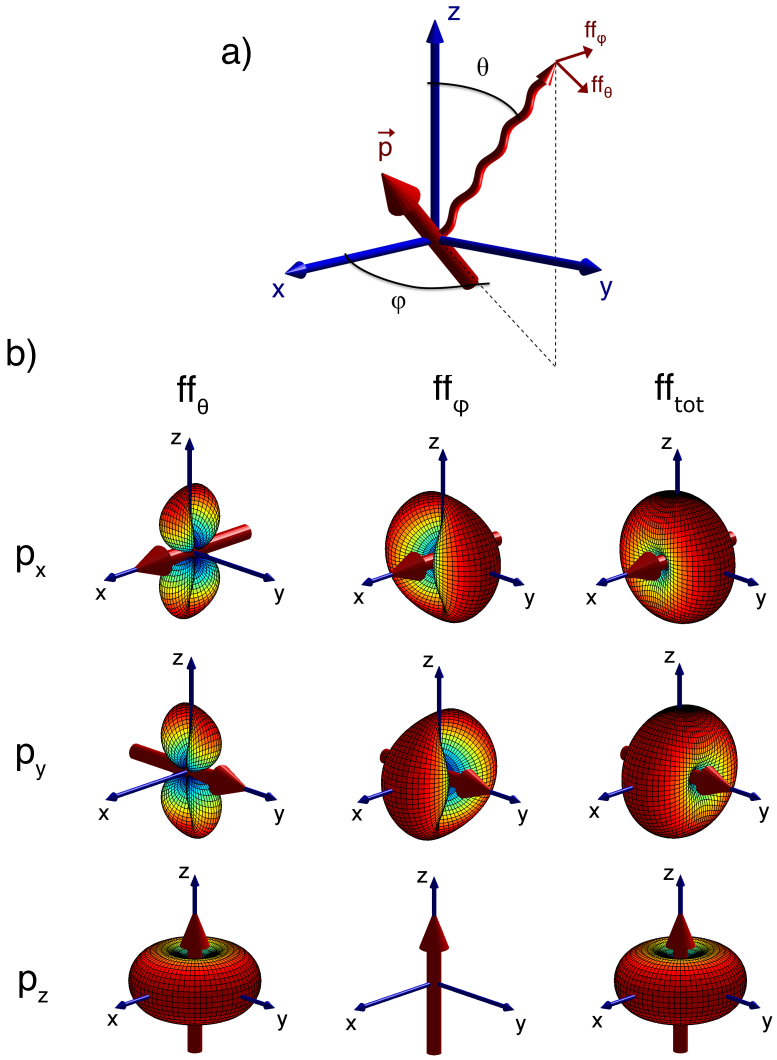


Figure 4.2: a) Scheme of the cartesian and spherical coordinates system employed for the plotting of Fig.4.2. A dipole $\mathbf{p}$ is located at the center of coordinates and the field components $ff_\theta$ and $ff_\varphi$ of $\mathbf{f}f$ are plotted for $0 < \theta < \pi$ and $0 < \varphi < 2\pi$ b) Radiation produced by a point dipole oriented in the direction of the three cartesian components (one per each horizontal line). The red arrow represents the dipole. The first column is the projection of the $ff$ amplitude on the $\hat{u}_\theta$ spherical unit vector, second column is the projection on the $\hat{u}_\varphi$ spherical unit vector and the third column is the total $ff$ amplitude, showing the classical donut like pattern around the direction of the radiating dipole.

the sample and collecting the $ff_\theta$ polarization of its far-field amplitude in this direction of the space. The same analysis could be applied to the $ff_\varphi$ polarization of the far-field at this same direction. In this case, $ff_\varphi \propto p_y$ and thus this polarization will serve to map the $E_y$ component of the near-field.

We can reach the same conclussions by particularizing Eqs. 4.4 and 4.5. For this direction ($\theta = 90^o$, $\varphi = 0^o$), they read:

$$ff_\theta \propto p_z = E_z\alpha_z \tag{4.6}$$

$$ff_\varphi \propto p_y = E_y\alpha_y \tag{4.7}$$

We will now analyze what happens for a different radiation direction. Writing Eqs. 4.4 and 4.5 for $\theta = 90^o$ and $\varphi = 90^o$:

$$ff_\theta \propto p_z = E_z\alpha_z \tag{4.8}$$

$$ff_\varphi \propto -p_x = -E_x\alpha_x \tag{4.9}$$

Thus, the $E_x$ component of the near-field can also be measured on the orthogonal $\varphi$ angle detecting the $ff_\varphi$ polarization of the light. It is also possible to reach the same conclusion by analyzing Fig. 4.2.

For any angle $\theta \neq 90^o$, $ff_\theta$ will inevitably contain information involving both $E_z$ and/or $E_x$ and $E_y$. Nevertheless, as $E_x$ and $E_y$ can be unequivocally determined in $ff_\varphi$ polarization, it would still be possible to recover $E_z$ through an adequate post-processing of the collected signals.

Nevertheless, this theoretical framework is not experimentally sustainable because of two main reasons: It is not possible to discern the scattering produced by the tip from the one coming from the sample, and on the other hand the tip, being a

large object itself, scatters asubstantial amount of light. Summarizing, there is a lot of background signal coming from the tip and the sample that masks the near-field information contained in the $ff$ radiation that would be desirable to measure.

The experimental solution to this problem was proposed by R. hillenbrand *et.at* in 2000 [71]. In order to get rid of the background signal, they processed interferometrically the far-field signal scattered by an oscillating AFM tip. We will assume that the sample lays on the $(x, y)$ plane and that the oscillation of the tip is on the $z$ direction. Being the background signal coming from the tip and the sample constant respect to the $z$ position of the tip, on a Fourier analysis of the detected signal, its $0^{th}$ harmonic would collect all the background signal, and the $z$-dependent scattering would be distributed over the $n > 0$ harmonics. The only signal that produces a $z$-dependent scattering is the radiation of the tip induced by the near-fields of the sample. The interferometrically processed $n^{th}$ harmonic of the scattering of the system will contain the information about the components of the near-field. This experimental setup has extensively proved its capabilities to measure the vectorial near-fields of different types of samples [8, 69, 72–75].

## 4.1 Vectorial mapping of the plasmonic near-field produced by nanoantennas

In order to clarify the concepts introduced above, we present an example of mapping of the near-fields induced in a plasmonic particle antenna acting as an antenna: a gold nanodisk . We will reproduce theoretically the experimental SNOM technique. The disk (90 nm diameter and 20 nm height) is laying on a $SiO_2$ substrate. We will excite the system at its dipolar resonance with a plane wave of 633 nm wavelength. The

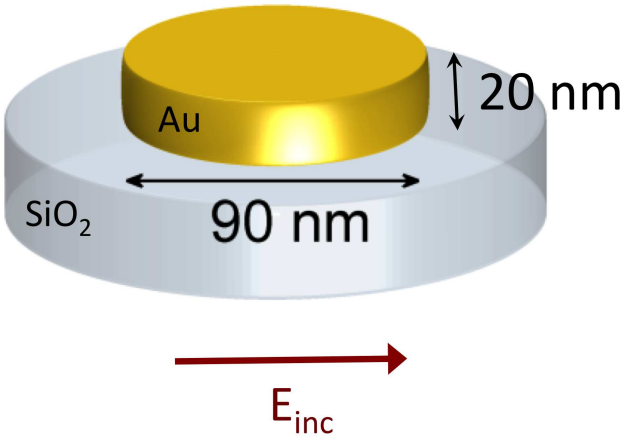


Figure 4.3: A gold disk of 90 nm diameter and 20 nm height on a $SiO_2$ substrate is illuminated with a 633 nm wavelength planewave under normal incidence (from below)

incidence is normal to the disk coming from below. Fig. 4.3 shows an scheme of the system under study.

Fig. 4.4, shows the vectorial components of the near-field induced at the nanoantenna over the $(x, y)$ plane at a height of z=15 nm above the surface of the disk. The dipolar nature of the electromagnetic response of the system is evident on the $E_z$ component of the near-field (left-hand side).

In order to simplify the problem, as introduced above, we will describe the probing tip as a point electric dipole with a polarizability associated to the optical response of a virtual sphere of radius $R = 32nm$ and dielectric constant $\varepsilon_{probe}$. The polarizability of such a dipole can be expressed as a diagonal 3x3 matrix $[\alpha_{probe}]$ whith diagonal elements defined as:

$$\alpha_{probe} = 4\pi \frac{\varepsilon_{probe} - 1}{\varepsilon_{probe} + 2} \tag{4.10}$$

We will use a low dielectric value for the probe of $\varepsilon_{probe} = 1.5$ in order to avoid strong interaction effects between the probe and the sample. This interaction effects

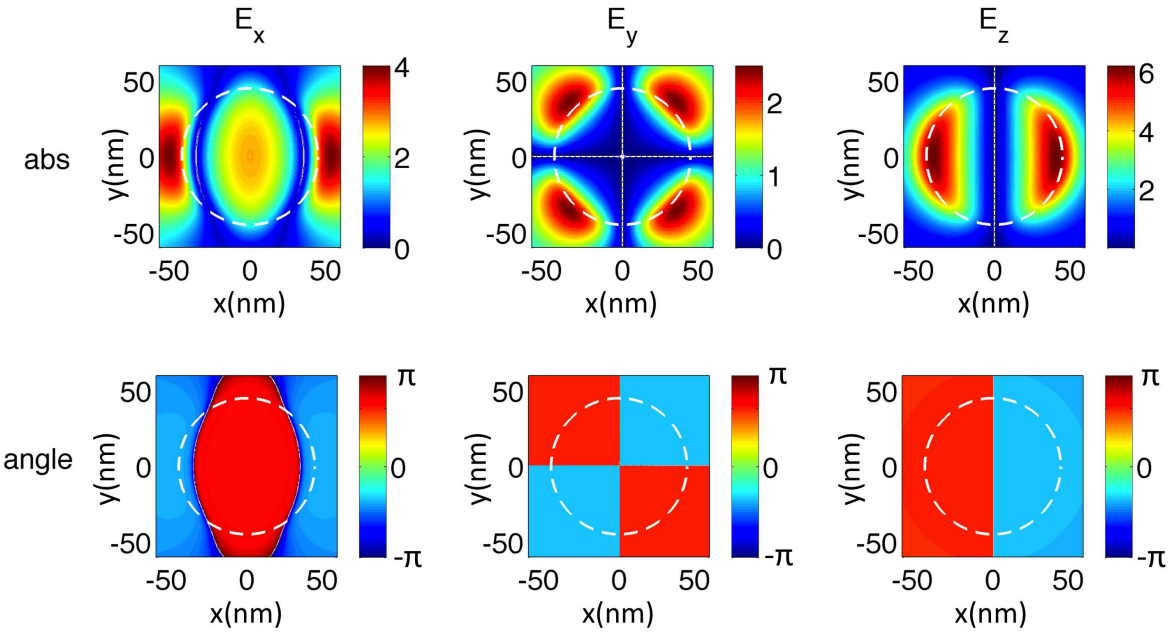


Figure 4.4: Amplitude and phase of the vectorial (x,y,z) components of the near-field induced over the disk sketched on Fig.4.3. The near-fields are calculated on the $(x, y)$ plane over a distance of 15 nm above the surface of the disk.

will be further studied in Section. 4.2.

Far-field detection will be performed at angles $\theta = 135^o$ and $\varphi = 180^o$. This incidence and detection polarization scheme receives the name of transmission mode SNOM [76]. In order to calculate the far-field scattering of the system, it will be necessary to calculate the self-consistent scattering produced by both the disk and the probe. We will employ the BEM to calculate both contributions. The radiation of the disk can be calculated on a straight-forward way. In order to calculate the scattering of the probe, it is first necessary to calculate the position dependent self-consistent dipolar moment of the probing dipole $\mathbf{p}_{probe}$. We calculate it with us of the following expression:

$$\mathbf{p}_{probe} = \frac{[\alpha_{probe}]}{1 - [\alpha_{probe}]\,[A]}\mathbf{E}_{ext} \tag{4.11}$$

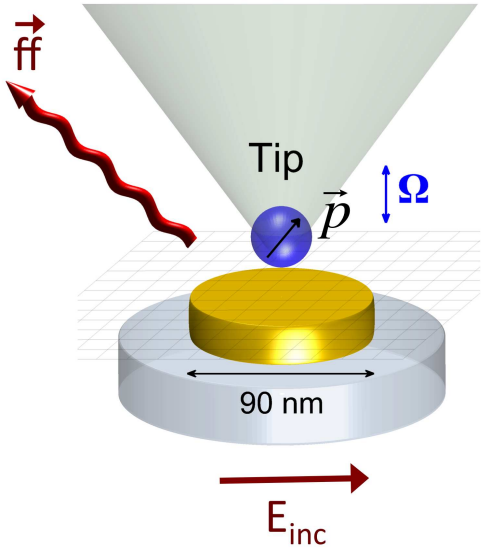


Figure 4.5: Sketch summarizing the theoretical framework that will be employed to calculate the self-consistent response of the system. The probing tip is modeled by a point dipole of dipolar moment $\mathbf{p}_{probe} = \mathbf{E}\alpha_{probe}$.

where $[A]$ is a 3x3 near-field self interaction matrix containing the vectorial near-field components induced at the position of the dipole by an unitary electric point dipole oriented on the 3 cartesian directions. $\mathbf{E}_{ext}$ is the total near-field induced by the disk at the position of the dipole under the plane wave illumination. Fig. 4.5 presents an schematic sketch of the employed theoretical framework.

First we calculate the near-fields induced at the disk while scanning the point electric dipole at a certain distance over the surface of the disk and analyzing the total far-field signal scattered by the system (disc + dipole) in the direction given by the angles $\theta = 45^o$, $\varphi = 180^o$. For simplicity, in this case, only the $ff_\theta$ component of the far-field will be analyzed. Fig. 4.6.a shows the direct result of this calculation. As observed, the constant background signal is too large to obtain information about any near-field pattern of the disk. Nevertheless, if we modify the color scheme to focus the attention on the slight variations of the detected signal (Fig. 4.6.b), surprisingly, no direct

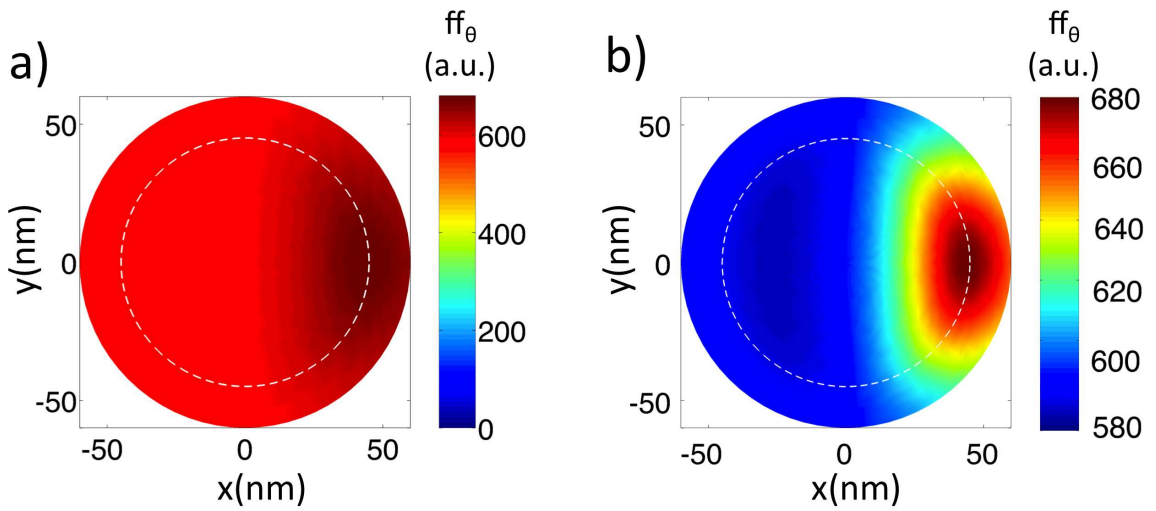


Figure 4.6: a) Map of the $ff_\theta$ radiation of the gold nanodisk as a function of the (x,y) position of the probing dipole $\mathbf{p}_{probe}$ with color scheme going from 0 to maximum value of the radiation. b) Same figure with color scheme raging from the minimum value of radiation to its maximum value.

correspondence can be established between this result and any of the near-field patterns obtained in Fig. 4.4. Being the scattering of the sample constant and the scattering of the tip proportional to the near-field, some correlation could be expected. This lack of correlation can be attributed to the phase interaction between the background far-field and the near-field signal. As a conclusion, total background suppression is necessary in order to distinguish any near-field signal from the far-field radiation of the whole system (tip + disk).

In order to overcome this problem, we will follow the procedure explained at the end of the previous section: For each $(x, y)$ scanning position of $\mathbf{p}_{probe}$, we will modulate the $z$ position of the dipole with a tapping amplitude of 20 nm and tapping frequency of $\Omega \approx 300$ kHz, corresponding to the experimental values of the mechanical oscillation of a model AFM tip. We then apply a Fourier-transform to the time dependent periodic far-field complex signal and then select a higher $n^{th}$ harmonic of this demodulated signal.

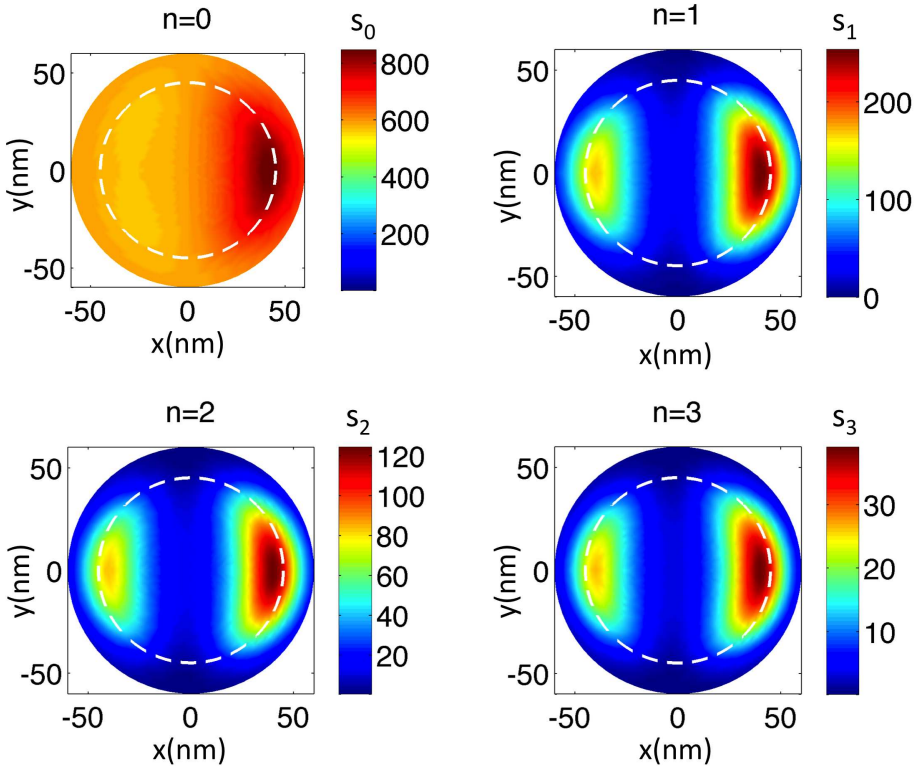


Figure 4.7: Magnitude of the demodulated maps of the modulus of the $ff_\theta$ component of the radiation for the same system (tip+disk) as in Fig. 4.6. $n$ indicates the demodulation order of each of the maps. $0^{th}$ order collects all the background signal since the it is constant with respect to the modulation variable $z$. Higher demodulation orders show a clear correlation with the characteristics of the $E_z$ component of the induced near-field (see right hand side of Fig. 4.4).

Fig. 4.7 presents the result of such a procedure for the magnitude of the $ff_\theta$ component of the far-field radiation of the disk-tip system. As it can be observed, the background signal is clearly obtained at the $0^{th}$ harmonic of the demodulated signal and higher harmonics present a pattern that clearly corresponds with the characteristics of the $E_z$ component of the near-field (see right hand side of Fig. 4.4), as expected.

Finally, Fig. 4.8 presents the demodulated maps in magnitude and phase of both $ff_\theta$ and $ff_\varphi$ components of the far-field for $n = 3$, which is a typical demodulation order chosen experimentally. As already mentioned, the demodulated $ff_\theta$ presents a strong

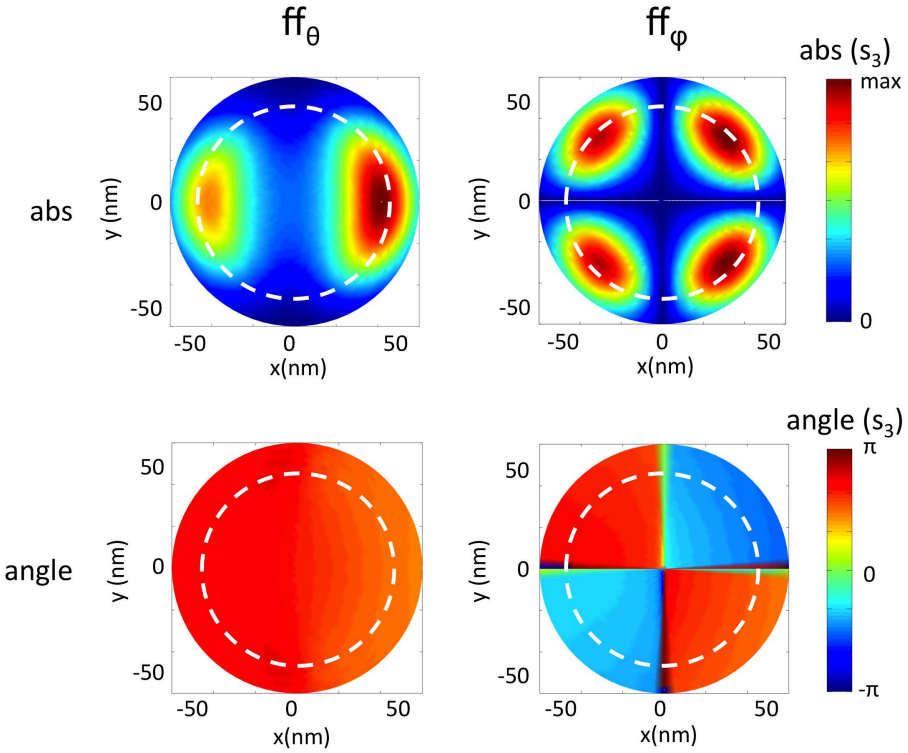


Figure 4.8: Magnitude and phase of the n=3 demodulation order of the far-field for the $ff_\theta$ (left) and $ff_\varphi$ (right) components. $ff_\theta$ presents a clear correspondence to the $E_z$ component of the near-field while $ff_\varphi$ corresponds to the $E_y$ component (see Fig. 4.4)

correlation with the $E_z$ component on the near-field (see Fig. 4.4). There is a slight asymmetry in the magnitude map and the phase difference is not $180^o$. This effect can be attributed to the fact that the detection is not performed at angle $\theta = 90^o$. As it is shown in Eq. 4.4, for such an angle of detection, the $ff_\theta$ component of the radiation of the probing dipole is not directly proportional to $E_z$. It also contains information from the local field $E_x$. Being $E_x$ not negligible, this distorts the measurement. On the other hand, the $n = 3$ demodulated amplitude and phase of the component $ff_\varphi$ are clearly equivalent to the ones of the $E_y$ component of the near-field. This was also already predicted by Eq. 4.5 for such a detection angle ($\varphi = 90^o$).

## 4.2 "Probe-sample" interaction in scattering-type near-field optical microscopy

Scattering-type scanning near-field optical microscopy (s-SNOM) [21] has managed to map both the local amplitude and phase of the near-field by interferometric detection of the antenna fields scattered by a scanning atomic force microscope tip [68–70] (see Fig. 4.9(a)). However, the antenna optical response is extremely sensitive to environmental changes, [19,75,77] thus the process of measurement of its near-field may result in the modification of the antenna modes, similar to probe-induced modifications in other nanophotonic systems [78–81]. In this section we address this issue, presenting a basic understanding of the near-field coupling between s-SNOM probes and plasmonic nanoantennas (here gold nanodisks). We find that weak dielectric probes allow for plasmon mode mapping, whereas metallic probes introduce substantial modification of the antenna modes due to strong probe-antenna coupling.

### 4.2.1 Experimental evidence of interacting regimes

First, we provide experimental evidence of weak and strong coupling regimes in near-field probing of plasmonic nanoantennas by s-SNOM mapping of gold nanodisks at their resonance wavelength $\lambda$ =633 nm [69]. The s-SNOM used in the experiment [Fig. 4.9(a)] is based on an atomic force microscope (AFM) with both disk and tip being illuminated from the side with P-polarized He-Ne laser light [71]. The measurement consists in the detection of light scattered from the tip that scans the nanodisk antennas. The AFM is operated in tapping mode where the tip is vibrating mechanically in the z-direction with frequency $\Omega \approx 300$ kHz and an amplitude of $\approx 20$ nm, thus demodulation of the scattered far-field allows for suppression of background scattering

and for recovering the near-field signal, as detailed in the previous section. Heterodyne interferometric detection yields amplitude $s_n$ and phase $\varphi_n$ signals with $n$ being the $n^{th}$ harmonic of the tapping frequency $\Omega$.

In Fig. 4.9c-f we show topography and background-free near-field amplitude images $s_3$ obtained with two different AFM tips: a carbon nanotube (CNT) Fig. 4.9c,d and a Pt-coated Si tip Fig. 4.9d,f. Using the CNT tip, the dipolar mode of the disk plasmon is clearly revealed in Fig. 4.9d. [69] The experimental image shows good agreement with the near-field amplitude calculated 21 nm above such a gold nanodisk in absence of the tip (Fig. 4.9b). Note that the slight asymmetry in the field pattern is due to the illumination geometry. In contrast, using a metallised AFM tip, the plasmon modes of the gold nanoatennas are strongly modified (Fig. 4.9f) and a clearly asymmetric pattern can be observed in the amplitude image: a bright spot appears in the far-edge of the disk with respect to the direction of the incoming radiation whereas a dark area is present in the near-edge. In light of these results, we can conclude that under the present illumination/detection scheme, a metal tip strongly disturbs the near-field modes of plasmonic nanoantennas, thus preventing near-field optical mode mapping. With use of the weak tip, however, mode mapping is possible.

### 4.2.2 Weak and strong coupling regimes

To understand the role of a probe in near-field imaging of plasmonic nanoantennas, we perform full electromagnetic calculations of the far-field amplitude $ff_\theta$ backscattered by the probe-nanodisk system as a function of probe position with use of the boundary element method (BEM) (See Appendix A) [40, 41]. For fundamental and straightforward insights into the interaction, we will employ the same theoretical framework described in the introduction of this chapter. We describe the probe as a point dipole with polarizability $\alpha_{probe}$ defined by Eq. 4.10. In this case, we will use dielectric values

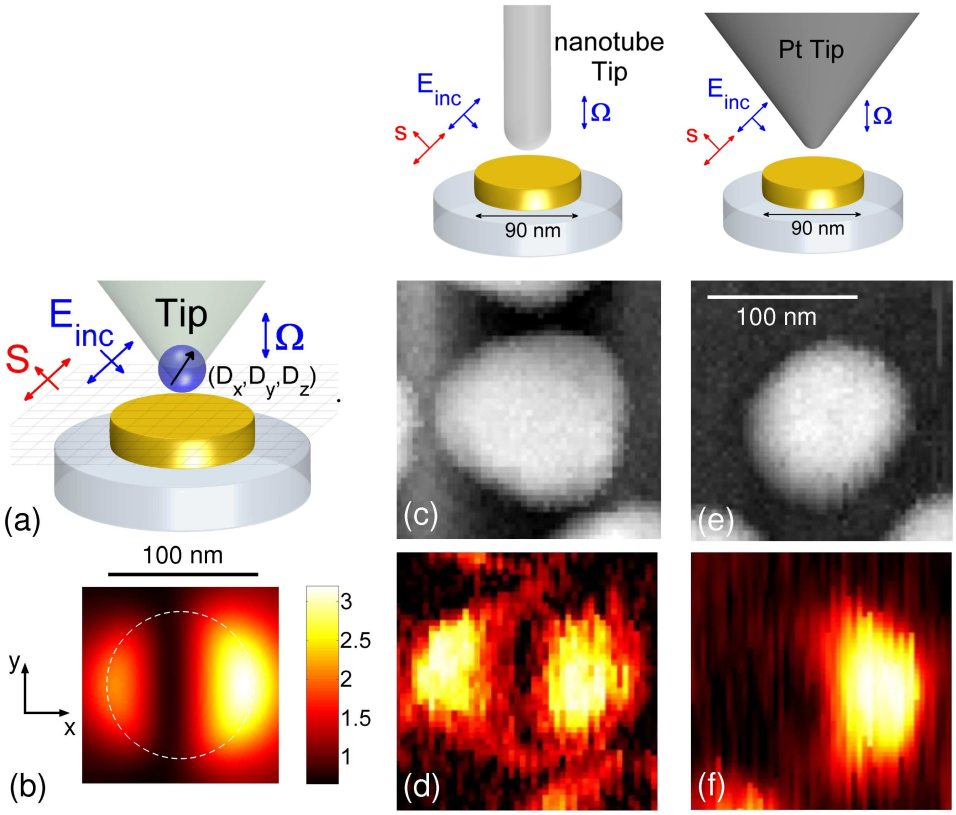


Figure 4.9: (a) Schematics of the near-field imaging process. A tip located at position $(D_x, D_y, D_z)$ scans the nanoantenna under study (gold nanodisk). We define $D_x = 0$, $D_y = 0$, $D_z = 0$ to be at the center of the disk on the top surface. Incident light $E_{inc}$ illuminates the tip-antenna system and backscattered far-field amplitude $s$ is recorded. (b) Calculated near-field amplitude on top of a gold nanodisk in absence of the tip. (c,d) Topography and near-field amplitude signal $s_3$ of a gold nanodisk obtained with use of a CNT tip. (e,f) Topography and near-field amplitude signal $s_3$ obtained with use of a Pt tip.

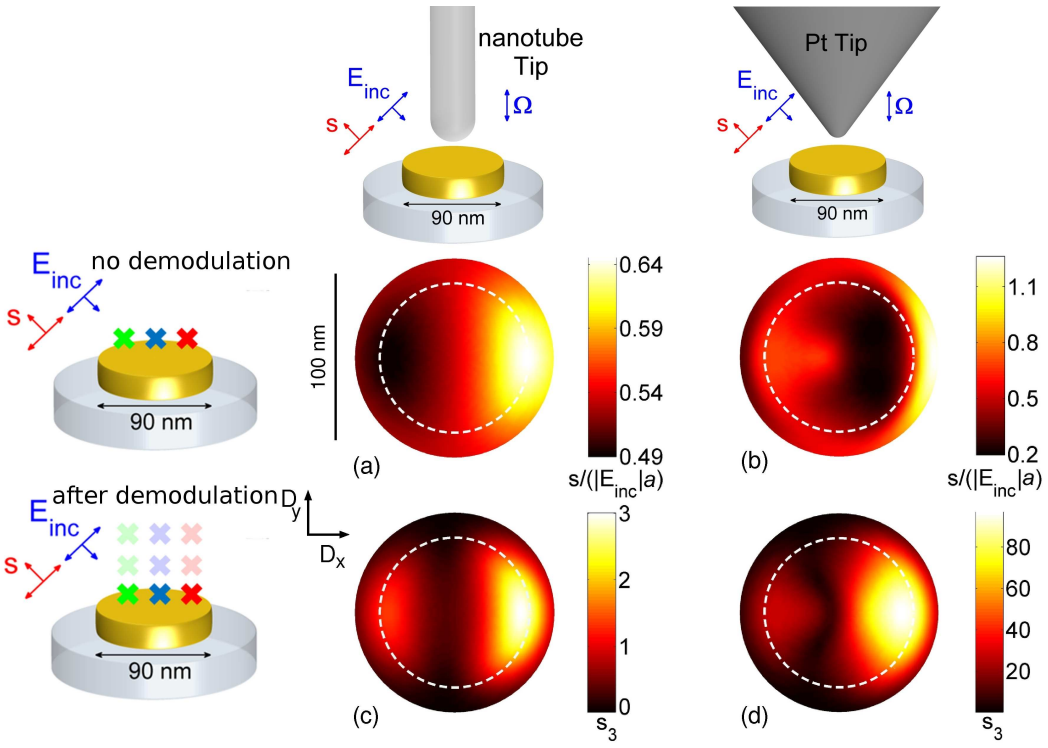


Figure 4.10: Calculated optical images of a 90 nm wide, 20 nm high gold nanodisk at a wavelength of $\lambda$ =633 nm. (a,b) Images showing the backscattered far-field amplitude $s$ normalized to the incident field $E_{inc}$ and the radius of the disk $a$, when the disk is scanned with (a) a weak dielectric probe and (b) a metallic probe. (c,d) Images showing the near-field signal $s_3$ when the disk is scanned with (c) a weak dielectric probe and (d) a metallic probe. The contour of the disks are marked by white dashed circles.

for the probe of $\varepsilon_{\text{probe}} = 1.5$ to resemble a weak dielectric probe (weak scatterer) and $\varepsilon_{\text{probe}} = -10 + 19i$ to resemble a metallic Pt probe (strong scatterer). The calculation is performed for the resonance wavelength of the disk, $\lambda$ =633 nm. P-polarized incident light and P-polarized detected light are considered under an incidence from the left of the disk (near-edge) of 45 degrees. In Fig. 4.10a,b we show the calculated images of $f f_\theta$ when scanning a probe dipole with low (Fig. 4.10a) and large (Fig. 4.10b) polarizabilities at constant height $D_z$ =21 nm.

The signal for a weak probing dipole (Fig. 4.10a) shows a nearly constant value with a slight increase at the far-edge of the nanodisk (variation of 20%). In this case,

the disk scatters a field which is much stronger than the field scattered by the probe dipole, and therefore the total far-field amplitude $ff_\theta$ is almost independent of the probe position. When scanning the probe, its weak far-field is added to the nearly constant scattering of the disk. For a strong probe dipole (Fig. 4.10b), the strong near-field coupling between probe and nanodisk produces a far-field scattering which is more complex and strongly dependent on the position of the probe, yielding a significantly different pattern and large contrast. It is interesting to note that none of the images based on the far-field scattering (Fig. 4.10a,b) reveal the near-field modes of the disk.

As pointed out in the introduction of this chapter, to describe the experimental near-field images in Fig. 4.9d,f we need to account in our calculations for the modulation of the tip-sample distance. For each horizontal position of the probe on the disk ($D_x$, $D_y$) we therefore calculate the backscattered far-field $s$ as a function of the height of the probe $D_z$. Assuming a sinusoidal vertical motion of the tip with an amplitude equal to the experimental tapping amplitude (20 nm), we demodulate $ff_\theta$ at the required order $n$. In our case we choose an order $n = 3$ but other demodulation orders give similar results. Interestingly, the calculated $s_3$ images obtained for a weakly scattering probe (Fig. 4.10c) clearly reveal the dipolar $E_z$ near-field component of the disk (Fig. 4.9b) in a similar fashion as obtained in the right hand side of Fig. 4.4. Obviously, it is the demodulation procedure that allows us to recover the near-field distribution of the disk, that would be otherwise masked by the strong antenna far-field scattering (Fig. 4.10a). Comparing now experiment and theory, we find a good agreement between the images $s_3$ recorded with a CNT tip (Fig. 4.9d) and the near-field signal calculated for a weakly scattering probe Fig. 4.10c). When we adopt a strongly scattering probe in our calculations, however, we find a much more pronounced bright spot in the far-edge of the disk (Fig. 4.10d) indicating a distorted near-field distribution. We actually find that the theoretical near-field images (Fig. 4.10d) exhibit a distortion resembling the

experimental maps obtained with a Pt tip (Fig. 4.9f), which do not reveal the antenna dipolar mode. We thus conclude the existence of both weak and strong coupling regimes between near-field probes and plasmonic nanoantennas.

### 4.2.3 Spectral analysis

To analyse the optical image contrasts in more detail, we study the spectral behavior of the backscattered amplitude $ff_\theta$ (Figs. 4.11a,b) and of the near-field signals $s_3$ (Figs. 4.11c,d) for three relevant positions of the probe on top of the disk. The far-edge ($D_x = +40$ nm), center ($D_x = 0$ nm), and near-edge ($D_x = -40$ nm) are selected as representative probe positions.

For a weakly scattering probe (Fig. 4.11a,c)), the position of the resonances in the backscattered amplitude $ff_\theta$ and the near-field signal $s_3$ match well with the plasmon resonance of the disk ($\lambda$ =633 nm). The presence of the tip obviously does not modify the spectral response of the nanoantenna, thus confirming weak coupling regime between the tip and the antenna. However, the amplitude $ff_\theta$ is mostly independent of the probe-position [see Fig. 4.11(a)], thus not revealing the dipolar near-field distribution when mapping the disk (see Fig. 4.10a). The $s_3$ signal, in contrast, clearly reveals the position-dependent spectral behavior of the nanoantenna near-field and thus allowing for plasmon mode mapping at $\lambda$ =633 nm (see Fig. 4.10c) . For a strongly scattering probe (Fig. 4.11b,d) we find considerable spectral shifts both in the far-field amplitude $ff_\theta$ and in the near-field signal $s_3$, depending on the probe position. These spectral shifts provide clear evidence of strong tip-antenna coupling modifying the plasmonic modes. The plasmon response is red-shifted when the probe is located at the far-edge of the disk (in red) whereas a slight blue-shift is observed at the near-edge position (in green).

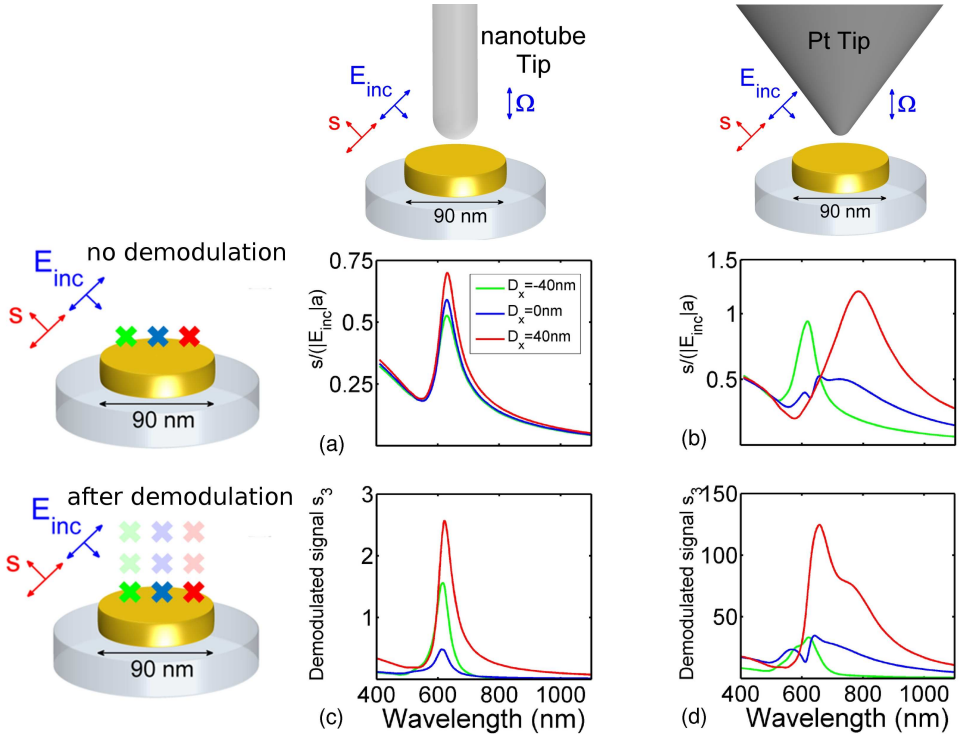


Figure 4.11: (a,b) Spectra of the backscattered far-field amplitude $s$ calculated for the probe-disk system normalized to the incident field $E_{inc}$ and the radius of the disk $a$. (a) Weak dielectric probe, (b) metallic probe. The vertical distance between probe and gold nanodisk is $D_z$ =21 nm. (c,d) Spectra of the near-field signal $s_3$ calculated for a weak dielectric probe (c) and for a metallic probe (d). Three different horizontal probe positions are considered in all calculations: far-edge $D_x = +40$ nm in red, center $D_x =$ 0 nm in blue and near-edge $D_x = -40$ nm in green.

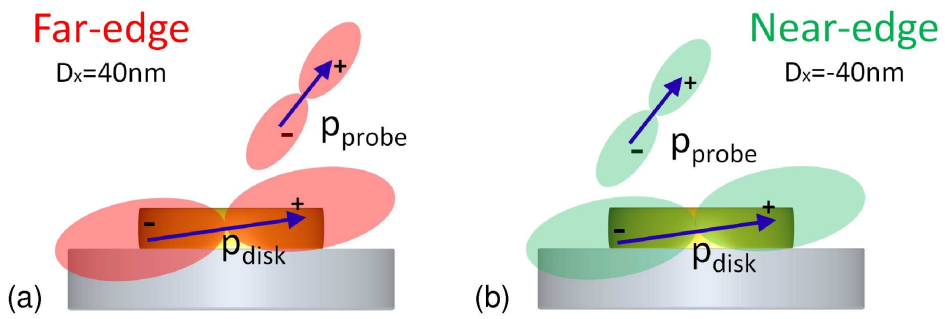


Figure 4.12: Schematics of the probe-disk coupling (a) Probe dipole located at the far-edge of a nanodisk basically yields longitudinal probe-disk coupling. (b) Probe dipole located at the near-edge of a nanodisk yielding transversal probe-disk coupling.

### 4.2.4 Simple model: dipole-dipole interaction

A simple understanding of the physics of such situations can be conceived in the schematics of Fig. 4.12a,b. The response of the disk and the tip can be interpreted as those corresponding to two dipoles characterized by different dipolar moments ($p_{\text{disk}}$ and $p_{\text{probe}}$). In the case of a weakly interacting probe, the dipole $p_{\text{probe}}$ hardly affects the strong field produced by the disk dipole ($p_{\text{disk}}$) and therefore the scattering is mainly given by the latter.

However, in the strongly-interacting regime, the polarizability of the scanning dipole $\alpha_{\text{probe}}$, and therefore its dipolar moment ($p_{\text{probe}}$) is similar in strength, or even larger, than the dipole of the disk ($p_{\text{disk}}$), therefore both dipoles interact very effectively, showing different spectral trends depending on their relative position. When the probe-dipole is on the far-edge of the disk ($D_x = +40$ nm in Fig. 4.12a), both dipoles are interacting mostly longitudinally, yielding a red shift of the response similar to the longitudinal interaction of two metallic nanoparticles [13, 14, 49]. When the tip is located at the near-edge of the disk ($D_x = -40$ nm in Fig. 4.12b), both dipoles can be considered to be coupled mostly transversally, therefore showing a decrease of the near field intensity with slight blue-shift (see green line in Fig. 4.11b), similar to the case

of transverse coupling of two nanoparticles. Essentially, for a strong probe dipole, it is this different probe-disk coupling scheme at the far-edge compared to the near-edge which is responsible for the spectral shifts and consequently for the distorted near-field images.

In summary, we have introduced the working principles of the scattering type Scanning near-field Scanning Optical Microscope (s-SNOM) and addressed quantitatively the influence of the tip response in near-field imaging of plasmonic structures establishing the weak and strong near-field coupling regimes between probe and antenna. An understanding of both weak and strong-coupling regimes is established and the limits to interpred near-field images are pointed out.

# CHAPTER 5

# CONTROL OF THE OPTICAL RESPONSE OF NANOANTENNAS

Optical and infrared antennas based on metal nanostructures allow for efficient conversion of propagating light into nanoscale confined and strongly enhanced optical fields, and vice versa [34, 66, 82–85]. This special capability, enables a variety of cutting-edge applications ranging from ultrafast photodetectors [86] to highly sensitive biosensors [4]. In order to maximize the benefits of optical antennas it is necessary to tailor them in order to satisfy the specific needs of each application. In that sense, the control over the localization of the areas where the near-field is maximum (hot-spots) and the tuning of the resonant frequencies of the antennas are central for many applications such as molecular fluorescence near optical antennas [66] and surface-enhanced spectroscopy [49].

In Chapter 2 we already introduced the importance of matching the resonance of an IR antenna with the vibrational lines of the molecules in order to get enhanced absorption signal from a small number of molecules. In that case, to tune the spectral response of the system, $\lambda/2$ antennas of different lengths were fabricated. Furthermore,

being able to control the resonant position of these dipole antennas without changing their length would be extremely beneficial for instance, for the technological implementation of the SEIRA technique. On the other hand, the measured signal proceed from the molecules laying on the caps of the antenna, which is the zone where the field is significantly enhanced. Having an extra control over the spatial distribution of this hot spots, would give extra capabilities to this technique, since it would permit the development of spatially resolved field enhanced spectroscopy experiments.

This chapter aims to introduce some possibilities to obtain control over the near-field spatial distribution and spectral response of nanoantennas. The first section presents a strategy to control the spatial position of the hot spots and the spectral response of plasmonic nanostructures by means of a probe-sample coupling mechanism. The second section of the chapter introduces a method to tune the resonances of gap antennas and their near-field distributions through the engineering of their load impedance.

## 5.1 Probe assisted opto-mechanical control of the optical response in plasmonic nanoantennas

The strong probe-sample interaction regime presented in Chapter 4.2 can serve as a tool to tune the optical response of plasmonic antennas, opening a new avenue for the probe to become an active opto-mechanical element to control the field distribution and spatially activate selected areas of the nanoantenna with sub-nanometer precision. [78]

We show in Fig. 5.1 a set of near-field maps of the gold disk studied in Chapter 4.2 when a strongly interacting tip is located at four different positions. The near-field is evaluated at 0.5 nm from the top surface of the nanodisk. The self consistent response of the system is calculated employing the same theoretical framework introduced in

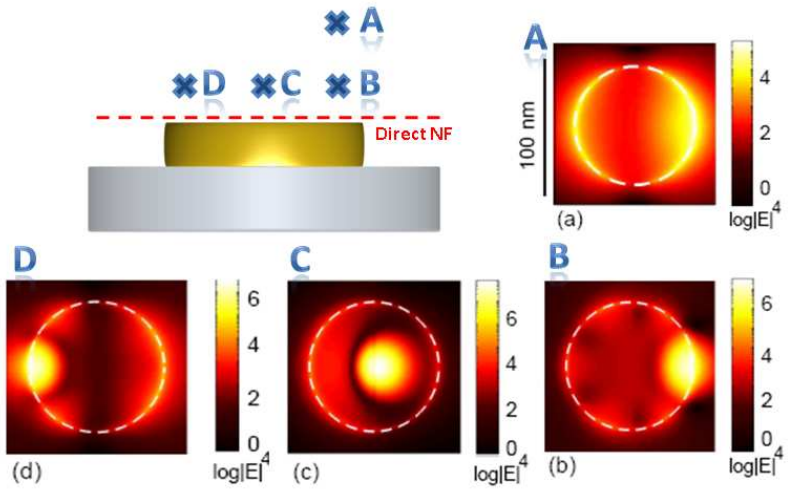


Figure 5.1: Fourth power of the calculated local field enhancement normalized to the incoming field on top of a gold nanodisk for four different positions of a strongly-interacting dipolar probe: (a) far edge at 41 nm on top of the disk, (b) far edge at 21 nm on top of the disk, (c) center at 21 nm on top of the disk and (d) near-edge at 21 nm on top of the disk.

Chapter 4.1. The fourth power of the field enhancement $E = E_{\mathrm{loc}}/E_{\mathrm{inc}}$ is displayed to emphasize the importance of local enhancement in inelastic molecular spectroscopy where the field intensity of both incoming and outgoing fields is relevant for increasing the signal, as pointed out in Chapter 2. Different vertical $D_x$ and horizontal $D_z$ probe positions generate very different near-field modes at the disk. When the probe is located at considerable vertical distance from the disk ($D_z$ =41 nm at the far-edge) the field pattern shows the dipolar mode of the disk (Fig. 5.1a), similar to the near-field distribution calculated in absence of the tip (Fig. 4.9b), which permits to conclude that only negligible probe-antenna coupling is present for such a distant positioning of the probe. As we get vertically closer to the disk (21 nm on top of the disk surface), moving along the horizontal from the far-edge (Fig. 5.1b), through the center (Fig. 5.1c), to the near edge (Fig. 5.1d), the bright spot reveals the localization of the near-field at the probe position. More interestingly, we find that higher order near-field modes are

generated on the disk depending on the position of the probe ($D_x$,$D_z$). Thus, the field-enhancement at different areas of the plasmonic nanoantenna can be activated or deactivated by nano-mechanical control of the tip-disk near-field interaction while the far-field response is simultaneously tuned as it was shown in Fig4.11a,b. This capability opens new perspectives for example in selective molecular light emission in the proximity of nanoantennas.

## 5.2 Controlling the response of plasmonic nanoantennas through gap-loading

We analyze in this section the use of gap antennas to obtain control of the near-field distributions spatially and spectrally. Antennas consisting of adjacent metallic segments (i.e. nanorods) separated by a nanoscopic gap (gap antennas) are particularly efficient for different applications on the field of nanophotonics [4,34,82,84,86–88]. The near-field coupling across the gap can generate extremely strong and localized fields which are essential for applications such as single-molecule surface-enhanced Raman spectroscopy (SERS) [4] or extreme-ultraviolet (EUV) generation [87]. However, the antenna response is very sensitive to small environmental changes at the gap [14,88,89]. Thus, the presence of molecules or semiconductors in the gap (as usually is the case in spectroscopy or detector applications) can dramatically affect the antennas far-field optical response with the possibility of degrading the antenna performance. On the other hand, we can take advantage of this effect for versatile tuning of the antenna response.

Recently, Al and Engheta [5,7] described this possibility in terms of antenna loading, a concept adapted from radio frequency (RF) technology. Following the RF design

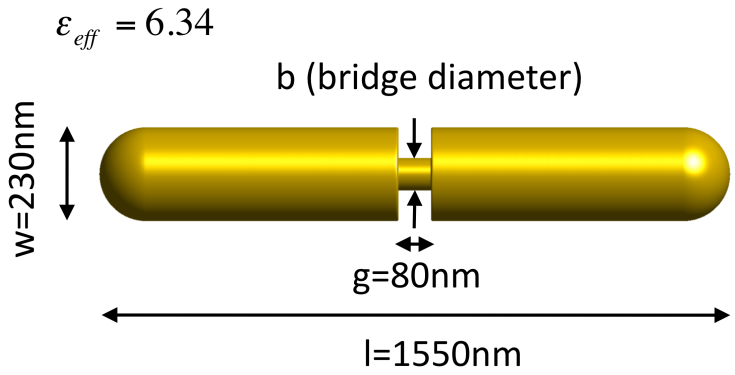


Figure 5.2: Sketch of the antennas that will be studied in this section. A $l = 1550nm$ length and $w = 230nm$ width gold antenna is divided in two sections by a gap of $g = 80nm$. The diameter of the gold bridge $b$ is the main varable of the study. The antennas are surrounded by an effective medium of dialectric constant $\varepsilon = 6.34$.

rules, it has been theoretically demonstrated that the scattering response and resonance frequency of optical antennas can be tuned by loading the antenna gap with either metals or dielectrics acting as inductors or capacitors, respectively. In this Section, we present a theoretical study of how loading of antenna gaps affects the far-field and near-field response of the system. By means of scattering type scanning near-field optical microscopy, it is possible to corroborate that the local near-field amplitude and phase response of gap nanoantennas can be controlled by antenna loading.

As a model system, we will study the far-field and near-field response of bridged gap antennas like the one sketched in Fig. 5.2. A gap gold IR antenna of length l=1550 nm, width w=230 nm and gap size g=80 nm is bridged by a gold bridge of arbitrary diameter $b$. The antenna is surrounded by an effective surrounding medium of $\varepsilon = 6.34$ in order to consider the effect of the Si substrate that further experimental measurements will require.

### 5.2.1 Control of the far-field response through gap loading

We first present the extinction spectra of the gap antennas calculated for bridge diameters between 0 nm and 100 nm which are summarized in the contour plot of Fig. 5.3. For large bridge diameter $b$, we observe a first-order dipolar mode (D1) of the antenna at around $\lambda$ ~10 $\mu$ m and a weaker second-order dipolar mode (D2) at $\lambda$ =3.5 $\mu$ m. With decreasing bridge diameter b, we observe a slight red shift of both modes. When the bridge reaches small diameters $b < 50$ nm, the behavior changes significantly. The first-order mode (D1) experiences a divergent red-shift at $b$ ~20 nm while being increasingly damped. This can be explained by the restriction of the charge flow across the gap that is necessary to build up a mode structure compatible with D1. Thus, in the limit of very small bridge diameters, the first-order mode (D1) cannot be excited anymore. The second-order mode (D2), in contrast, is enhanced with decreasing b and turns into the first-order mode of the coupled nanorods (C1), owing to the compatible structure of the dipole-dipole like mode both for the large and small bridges. If we consider now the antenna response at a fixed wavelength of $\lambda$=9.6 $\mu$ m (white dashed line in Fig. 5.3), we clearly observe a transition from the first-order dipolar mode (D1) of a continuous rod (large b) towards the mode of the coupled nanorods (C1) when b is decreasing.

### 5.2.2 Connection with circuit theory

In the radio frequency (RF) range, circuit theory is an essential tool for the efficient design of antenna devices. Adopting RF concepts at visible and infrared frequencies, we now show how the behavior of the loaded infrared antennas can be explained within the framework of optical circuit theory, which has been recently introduced by Engheta and collaborators. [5–7] We can describe the impedance of the antenna load $Z_{load}$ as a

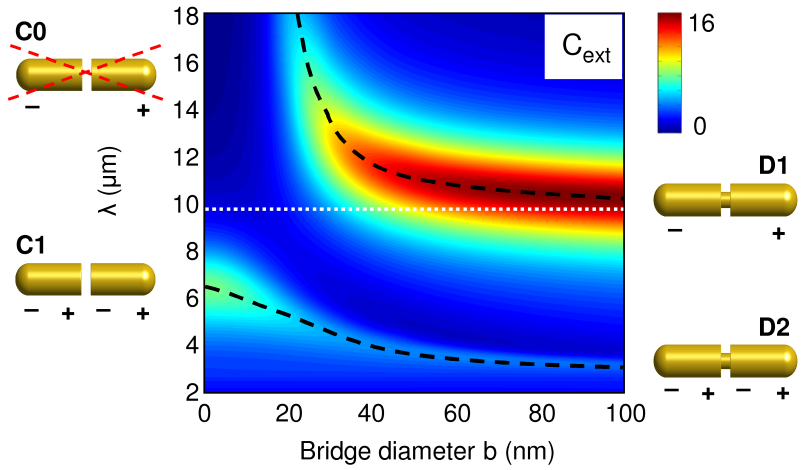


Figure 5.3: Extinction cross section calculated for the antennas considered in Fig. 5.2 as a function of the bridge diameter $b$, normalized to the projected area of the antenna. The dashed black lines trace the extinction resonances. The first-order and the second-order mode of the continuous rod are marked by D1 and D2, respectively. For antennas with $b = 0$ (capacitive gap), C1 is the first-order mode. The zero-order mode $C_0$ is unphysical because it would require finite net charge on each antenna segment separately [35].

parallel circuit composed of the inductive impedance of the metallic bridge $Z_{bridge}$ and the capacitive impedance of the effective medium filling the rest of the gap $Z_{gap}$ , given by

$$Z_{bridge} = \frac{ig}{\omega\varepsilon_{eff}\pi(\frac{b}{2})^2}, Z_{gap} = \frac{ig}{\omega\varepsilon_{eff}\pi(\frac{d}{2})^2 - (\frac{b}{2})^2} \tag{5.1}$$

and then,

$$Z_{load} = \frac{1}{Z_{bridge}} + \frac{1}{Z_{gap}} \tag{5.2}$$

Here, $g$ is the gap width (80 nm), $\omega$ the frequency, $\varepsilon_{Au}$ the dielectric value of gold and $\varepsilon_{eff}$ the dielectric value of the effective medium filling the gap of our model antenna considered in Fig. 5.2. In Fig. 5.4a we display a contour plot that shows the value of the load reactance $X_{load}$ (given by $Z_{load} = R_{load} - iX_{load}$) as a function of bridge diameter $b$ and wavelength $\lambda$, highlighting regions of inductive (blue) and capacitive (red) behavior of the load. Comparing the evolution of the antenna modes

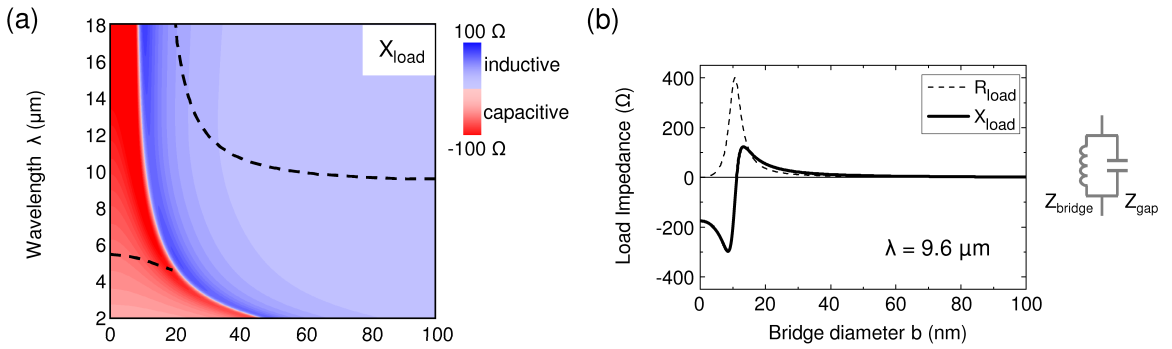


Figure 5.4: (a) Contour plot displaying the load reactance $X_{load}$as a function of $b$ and wavelength $\lambda$. Regions of capacitive reactance (negative $X_{load}$) are shown in red, regions of inductive reactance (positive $X_{load}$) in blue. The black dashed lines trace the first-order antenna resonances calculated by means of circuit theory. (b) Load resistance $R_{load}$ and load reactance $X_{load}$ displayed as a function of $b$, calculated for $\lambda = 9.6\mu m$.

(Fig. 5.3) with the behavior of $X_{load}$ (Fig. 5.4), we find an interesting connection: The first-order mode D1 strongly shifts to longer wavelengths when $X_{load}$ increases (more inductive, displayed in darker blue). The region of capacitive $X_{load}$, however, does not support the D1 mode. The intensity of the D2 mode in contrast strongly increases when the load becomes mainly capacitive. Within circuit theory, we can describe the load-induced spectral shifts of the antenna modes by modeling our infrared dipole antennas as a series combination of the dipole intrinsic impedance $Z_{dip} = R_{dip} - iX_{dip}$ (plotted in Fig. 5.5) and the load impedance $Z_{load}$ [5,6]. In this equivalent circuit, the antenna resonance occurs when the load reactance cancels the dipole intrinsic reactance, $X_{load} = -X_{dip}$. Evaluating this condition, we obtain the resonance wavelength as function of the bridge size $b$. The result is shown in Fig. 5.4 by dashed lines. For large $b$, the circuit resonance appears at about 9.3 $\mu$m wavelength, which is in good agreement with the resonance wavelength obtained from the extinction spectrum (Fig. 5.3). With decreasing $b$, still in the inductive region, we find that the circuit resonance is red-shifted owing to an increase of the load reactance $X_{load}$ (darker blue). Below the critical

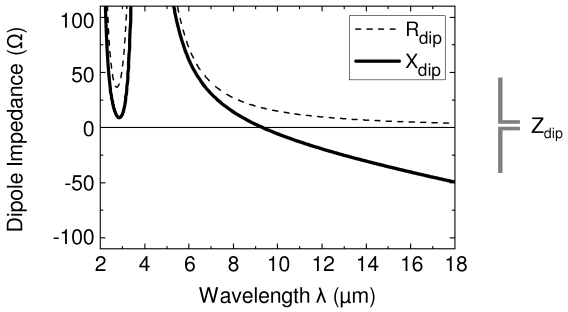


Figure 5.5: Intrinsic resistance $R_{dip}$ and reactance $X_{dip}$ of a cylindrical dipole antenna as a function of wavelength. The calculation is based on standard equations of antenna theory [1] and assumes a 1550 nm long antenna of 230 nm diameter embedded in an effective medium with $\varepsilon_{eff} = 6.34$.

bridge size $b_c$ which can be defined as the turning point where the load changes from inductive to capacitive nature, the circuit resonance suffers an abrupt change, shifting to shorter wavelengths owing to the change of sign of $X_{load}$, and correspondingly of $X_{dip}$. Comparing the evolution of the circuit resonances (dashed black lines in Fig. 5.4) with the spectral behavior of the antenna modes (dashed black lines in Fig. 5.3), we find a remarkable agreement considering the simplicity of the model based on classical antenna theory.

### 5.2.3 Controlling the near-field response of gap antennas

In order to analyze the behaviour of the near-field in loaded antennas, as those described in Fig. 5.2, we calculate the z-component of their near-field amplitude $|E_z|$ and phase $\varphi_z$ for a set of different bridge sizes.

Fig. 5.6a shows the near-field amplitude and phase images of a continuous (unmodified) nanorod. The images reveal strong amplitude signals at the rod extremities and a phase jump of about 180 at the rod center, providing a direct evidence of an anti-phase field oscillation as expected for the dipolar near-field mode. In Fig. 5.6d, we study a

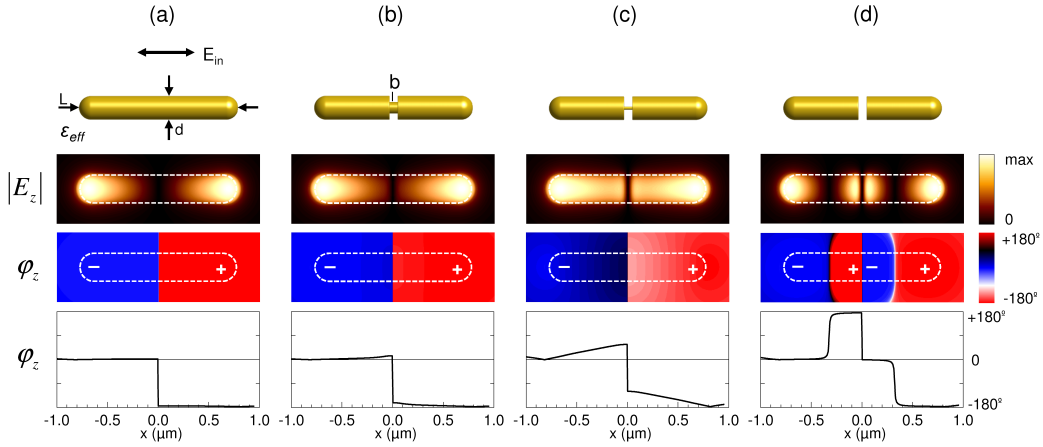


Figure 5.6: Theoretical near-field distribution of 1550 nm long Au antennas with d = 230 nm diameter and an 80 nm gap in its center, embedded in an effective medium of dielectric value $\varepsilon_e ff = 6.34$. The gap is bridged by gold disks of 80 nm length with diameter (a) b = 230 nm, (b) b = 80 nm, (c) b = 40 nm (amplitude image) and b = 30 nm (phase image), (d) b = 0 nm. The near-field images show the z-component of the electric field amplitude $|E_z|$ and phase $\varphi_z$ at a height of 50 nm above the rod surface. In all phase images, the phase is set to $0^o$ at the left antenna extremity.

nanorod that was fully cut in its center, representing an unloaded gap antenna. The near-field images show that each antenna segments oscillate in a dipolar-like mode, featuring high amplitude signals at the antenna extremities and near the gap, as well as a phase jump of 180 near the center of each segment and inside the gap. The near-field patterns of the gap antennas are completely changed when a metal bridge of diameter of 80 nm (representing the load) connects the two antenna segments (Fig. 5.6b). Near the gap, in contrast to the fully-cut rod (Fig. 5.6d), no significant near-fields are observed. Obviously, the small metal bridge suffices to restore the fundamental dipolar near-field mode of the continuous rod (Fig. 5.6a). This effect can be attributed to a current flow through the bridge that prevents charge pile up at the gap.

A highly interesting near-field distribution is observed in Fig. 5.6c where a much thinner metal bridge connects both nanorod segments. The bridge diameter is of $b = 30nm$, thus being significantly reduced compared to Fig. 5.6b. The near-field im-

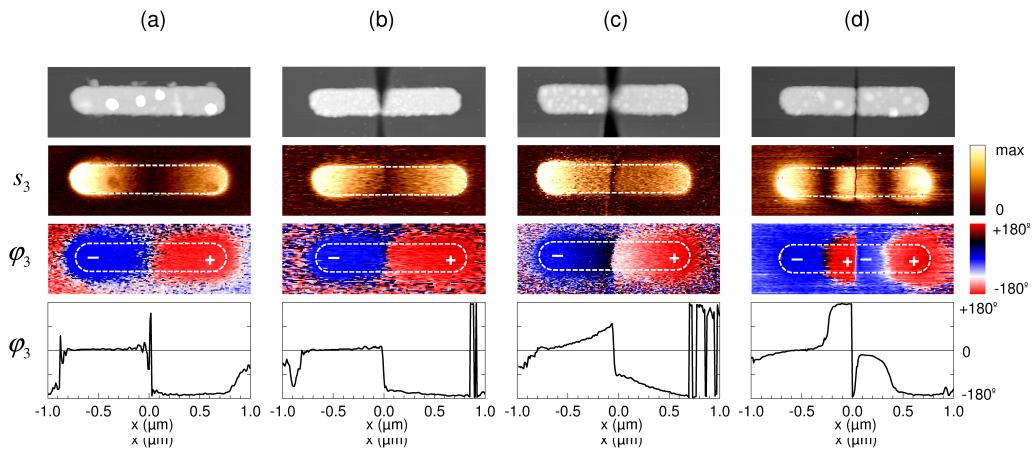


Figure 5.7: Top: Topography images of the antennas under study. Bottom: Experimental near-field images showing the near-field amplitude $s_3$ and phase $\varphi_3$ images of progressively loaded nanoantennas. The antennas have a total length of 1550 nm and are measured at a wavelength $\lambda$=9.6 $\mu$m. (a) Continuous rod antenna (b) Low-impedance loaded antenna where a thick metal bridge connects the two antenna segments. (c) High-impedance loaded antenna where a tiny metal bridge connects the two antenna segments. (d) Fully-cut antenna where the two antenna segments are completely separated. Experiments performed by M. Schnell at R. Hillenbrand's group at nanoGUNE, Donostia.

ages show striking differences to both the continuous and the fully-cut rod. We observe a significant amplitude signal along the total length of each segment and a considerable phase gradient of about 80. If we go back to Fig. 5.3, we can observe how this particular point of the chart ($b = 30nm$, $\lambda = 9600nm$) lies in between the two branches coming from D1 and D2. Thus, the near-field distribution of the antenna comprises contributions of both branches, yielding the strong phase shift on each antenna segment, an effect that we clearly identify in both the experimental and calculated near-field images.

To conclude, present an experimental study of this situation to corroborate how the progressive loading of an antenna gap affects the near-field distribution. The experiment presented in this section where performed by M. Schnell at R. Hillenbrand's group at nanoGUNE, in donostia. In order to to map the near-field amplitude and phase response of the rods a transmission-mode s-SNOM [21, 90] operating at a wavelength of $\lambda$=9.6 $\mu$m [76] is employed. The experiments are performed over antennas based on gold nanorods designed for fundamental dipolar resonance at mid-infrared frequencies, similar to the ones presented theoretically. The rods (1550 nm x 230 nm x 60 nm) were fabricated on a Si substrate by e-beam lithography and show a far-field resonance at a wavelength of $\lambda$ =9600 nm [83]. To create the loading bridges, focused ion beam (FIB) milling was used to prepare gaps of different shapes and sizes at the center of the rods.

Fig. 5.7 presents the topography of the fabricated antennas and the measured experimental near-field amplitude ($s_3$) and phase ($\varphi_3$) maps. In Fig. 5.7a the response of an unmodified fully resonant antenna is studied. Fig. 5.7d presents the results for a fully-cut antenna. The antennas studied on Fig. 5.7b and c present two intermediate cases with connecting bridges of two different sizes.

In order to correlate the fabricated samples with concrete bridge diameters, we

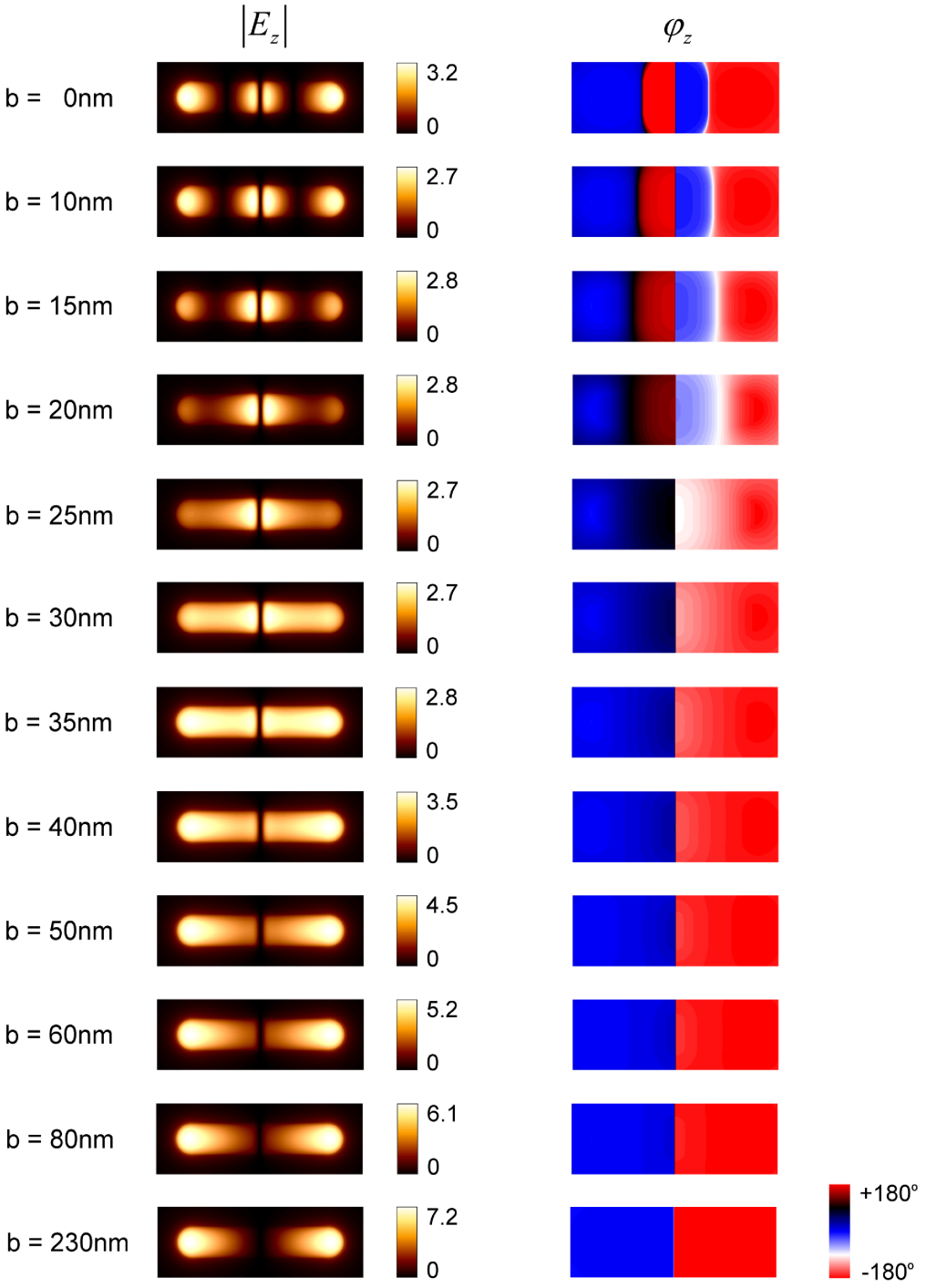


Figure 5.8: Near-field distribution of two Au rods with 230 nm diameter separated by an 80 nm gap. The gap is progressively loaded with 80 nm long Au disks of a diameter $b$ between 0 nm and 230 nm (antenna length $L = 1550$ nm, diameter $d = 230$ nm, effective medium $\varepsilon_{eff} = 6.34$). Amplitude $E_z$ and phase $\varphi_z$ of the z-component of the electric field are shown (normalized to the incident field).

perform a set of NF calculations for a complete set of bridge diameters. The results shown in Fig. 5.8 reveal that by progressive antenna loading (increasing bridge diameter b) the near-field pattern of the fully-cut rod ($b = 0$) evolves towards the fundamental dipolar mode of the continuous rod. By comparing experiment and theory, we can assign to each s-SNOM image in Fig. 5.7 a calculated near-field pattern of those shown in Fig. 5.8. For the antenna in Fig. 5.7b, we obtain good agreement for a bridge diameter of b = 80 nm which corresponds to 12% of the rods cross section. This is consistent with the bridge size estimated from the topography image. The s-SNOM images in Fig. 5.7c match well with calculated near-field patterns for b between 30 nm to 40 nm ( 2% of the rod cross sectional area), thus confirming that indeed a tiny metallic bridge is connecting the two segments in our experiment.

Finally, we address how the role of the load impedance affects the near-field distribution of the antennas. At the experimental wavelength of 9.6 $\mu$m the dipole intrinsic impedance amounts to $Z_{dip} = (17 + 2i)\Omega$ (Fig. 5.5). For large bridge diameters (b ¿ 80 nm) we find that the load impedance $Z_{load}$ is considerably smaller than $Z_{dip}$, thus facilitating current flow through the load. Consequently, accumulation of charges at the gap is very low, yielding negligible near-fields in its vicinity (Fig. 5.7b). Below the critical bridge size $b_c$, the load impedance is of capacitive nature. Therefore, charges are piled up at the gap, generating strong near-fields, as observed both in experiment and calculations (Fig. 5.7d and Fig. 5.6d respectively). Interestingly, the deviation of the near-field patterns from dipolar-like modes (Fig. 5.7c and Fig. 5.6c) occurs close to the critical bridge size (see also Fig. 5.8), thus confirming that the change of the near-field distribution is a consequence of the transition from inductive to capacitive load impedance.

In conclusion, the near-field images of gap antennas presented here provide an evidence that the local near-field amplitude and phase distribution can be controlled

by antenna loading. This opens the door for designing near-field patterns without the need to change antenna length or shape which could be highly valuable for the development of compact and integrated nanophotonic devices.

# APPENDIX A

# THE BOUNDARY ELEMENT METHOD (BEM)

Analytical exact solutions to Maxwell's equations only are known for some concrete geometries like spheres, spheroids, or infinite cylinders. This inability to derive exact analytical solutions for the electromagnetic response of realistic systems, makes the numerical solution of Maxwell's equations absolutely necessary in the field of nanophotonics.

There exist several techniques to afford this calculations. To mentions some, some of the most popular ones are the "Finite Difference Time Domain" (FDTD) method [refs], the Discrete Dipole Aproximation (DDA) [ref] or the Boundary Element Method (BEM).

All the theoretical simulations presented in this thesis were developed employing the Boundary Element Method. As a first step, this method expresses Maxwell's equations in terms of induced charges and currents at the interfaces of the objects under study. This way, the 3 dimensional problem of calculating the electric ($\mathbf{E}$) and magnetic ($\mathbf{H}$) fields across the domain of the problem is reduced to 2 dimensions. The boundary conditions for the electric and magnetic fields at the surfaces convert Maxwell's

equations into the following set of surface integral equations where the currents ($\mathbf{h_j}$) and the charges ($\sigma_j$) are the unknowns. For simplicity, in this case a system with a single boundary will be considered. Under scripts make reference to each side of the boundary. The resulting equations (expressed in atomic units) are:

$$G_1\sigma_1 - G_2\sigma_2 = -(\varphi_1 - \varphi_2) \tag{A.1}$$

$$G_1\mathbf{h_1} - G_2\mathbf{h_2} = -(\mathbf{g_1} - \mathbf{g_2}) \tag{A.2}$$

$$H_1\mathbf{h_1} - H_2\mathbf{h_2} + p\mathbf{n_s}G_1\sigma_1 = -\mathbf{q_1} + \mathbf{q_2} - p\mathbf{n_s}\varphi_1 \tag{A.3}$$

$$\frac{1}{ik}(\varepsilon_1 H_1\sigma_1 - \varepsilon_2 H_2\sigma_2) - \varepsilon_1\mathbf{n_s}G_1\cdot\mathbf{h_1} + \varepsilon_2\mathbf{n_s}G_2\cdot\mathbf{h_2} = \varepsilon_1\left(\mathbf{n_s}\cdot\mathbf{g_1} - \frac{f_1}{ik}\right) - \varepsilon_2\left(\mathbf{n_s}\cdot\mathbf{g_2} - \frac{f_2}{ik}\right) \tag{A.4}$$

with $G_j(r) = \exp(ik_j r)/r$ appropiate for each separate medium, where $k_j = k\sqrt{\varepsilon_j(\omega)}$ and the square root is chosen such that $k_j$ lies in the upper complex plane. $\varepsilon$ is the space and frequency dependent local dielectric funcion. $k = \omega/c$ and $\rho(\mathbf{r})$ is the external charge (current) density.

On the other hand, $H_j(\mathbf{s}-\mathbf{s}') = (n_s)\cdot\nabla_s G_j\left(|\mathbf{s}-\mathbf{r}|\right) \pm 2\pi\delta(\mathbf{s}-\mathbf{s}')$ (the sign is + for $j = 1$ and − for $j = 2$), $p = ik(\varepsilon_2 - \varepsilon_1)$,

$$\left[\begin{array}{c}\varphi_j(\mathbf{s})\\ f_j(\mathbf{s})\end{array}\right] = \int d\mathbf{r}\left[\begin{array}{c}\\ \mathbf{n_s}\cdot\nabla_s\\ \\ \end{array}\right] G_j\left(|\mathbf{s}-\mathbf{r}|\right)\frac{\rho(\mathbf{r})}{\varepsilon(\mathbf{r},\omega)} \tag{A.5}$$

and

$$\begin{bmatrix} \mathbf{g_j}(\mathbf{s}) \\ \mathbf{q_j}(\mathbf{s}) \end{bmatrix} = \frac{1}{c} \int d\mathbf{r} \begin{bmatrix} \mathbf{n_s} \cdot^1 \nabla_s \end{bmatrix} G_j \left( |\mathbf{s} - \mathbf{r}| \right) \mathbf{j}(\mathbf{r}) \tag{A.6}$$

Note that matrix notation has been adopted, in this way surface coordinates $\mathbf{s}$ are used as matrix and vector indices, and matrix and vector products like $G_j \sigma_j$ involve integration over the interface. Being N the number of discretization points of the surface of the object, the problem reduces to a set of 8N lineal equations (equations A.1 to A.4) that can be solved through algebraic matrix inversion techniques.

Once the boundary currents ($\mathbf{h_j}$) and the charges ($\sigma_j$) are calculated, the scalar and vector potentials $\phi(\mathbf{r})$ and $\mathbf{A}(\mathbf{r})$ can be calculated through the following formalism:

$$\begin{bmatrix} \phi(\mathbf{r}) \\ A(\mathbf{r}) \end{bmatrix} = \int d\mathbf{r}' G_j \left( |\mathbf{r} - \mathbf{r}'| \right) \begin{bmatrix} \rho(\mathbf{r}')/\varepsilon(\mathbf{r}', \omega) \\ \mathbf{j}(\mathbf{r}')/c \end{bmatrix} + \int_S d\mathbf{s} G_j \left( |\mathbf{r} - \mathbf{s}| \right) \begin{bmatrix} \sigma_j(\mathbf{s}) \\ \mathbf{h_j}(\mathbf{s}) \end{bmatrix} \tag{A.7}$$

From these potentials, the electric and magnetic fields can be calculated as:

$$\mathbf{E} = \frac{iw}{c} \mathbf{A} - \nabla \phi \tag{A.8}$$

$$\mathbf{H} = \nabla \times \mathbf{A} \tag{A.9}$$

The only assumption of this method is that the media defining the objects under study has to be described by frequency dependent homogeneous local dielectric functions. A more extensive description of this method and its generalization to an arbitrary number of different media can be found on References [40] and [41].

# SUMMARY

This thesis presents a set of contributions to the field of nanophotonics which are based on the potential of plasmonic nanoantennas to enhance spectroscopy and microscopy techniques.

The introductory chapter presents historical approach to electromagnetic antennas and the differences and new physical phenomena that arise when trying to adapt those resonant structures to the visible and infrared frequency range of the spectrum. The potential of these structures and several emerging applications are also introduced.

On Chapter 2 we demonstrate how infrared vibration signals of a small number of molecules can be enormously enhanced by 5 orders of magnitude through the resonant interaction of the vibration dipoles of the molecules with the broadband IR plasmonic antenna resonance of a gold nanowire. This interaction can be interpreted as classical analogy to the antiresonances produced in the Fano effect. This enhancement mechanism enables a new powerful technique for surface enhanced IR scattering with general importance for a variety of fields. By exploiting the resonant enhancement in the vibrational spectra, as shown in this work, it has been possible to detect and to study extremely small quantities of molecules, thus lowering the detection limit of

direct IR vibration spectroscopy considerably, establishing a new paradigm in SEIRA spectroscopy.

Chapter 3 summarizes the electromagnetic effects that can be used to optimize the near-field enhancement of metallic nanostructures. Furthermore, we show how it is possible to combine all these effects on a single nanostructure to design a single geometry where the field enhancement reaches the largest values reported in the literature. The designed structure presents a field enhancement of 3 orders of magnitude in amplitude at the near IR part of the spectrum. To obtain these factors realistic values for the dielectric response and damping of the metals have been used, therefore this type of factors could be reached experimentally in principle.

On Chapter 4, we introduce a theoretical approach to the scattering type scanning near field optical microscopy technique (s-SNOM) and we address quantitatively the influence of the tip in the near-field imaging of plasmonic structures, establishing the weak and strong near-field coupling regimes between probe and antennas. Based on rigorous numerical calculations and on a simple interaction scheme, we have interpreted correctly different near-field images of similar plasmonic disks.

Finally, Chapter 5 presents two methods to control the antenna response of plasmonic nanostructures. First, we show how the strong tip sample interaction regime presented on the previous chapter introduces the capability for a near-field probe to control the far field and near field response of a plasmonic antenna with a precision in the sub-nanometer range, which is otherwise not yet accessible with current fabrication technology. Moreover, we show how modifying the gap impedance of gap antennas allows to establish a control over their near field and far field response.

# BIBLIOGRAPHY


[1] C A. Balanis. *Antenna Theory*. John Wiley & Sons, 2005.

[2] Palash Bharadwaj, Bradley Deutsch, and Lukas Novotny. Optical Antennas. *Advances*, pages 438–483, 2009.

[3] Katrin Kneipp, Yang Wang, Harald Kneipp, Lev Perelman, Irving Itzkan, Ramachandra Dasari, and Michael Feld. Single Molecule Detection Using Surface-Enhanced Raman Scattering (SERS). *Physical Review Letters*, 78(9):1667–1670, 1997.

[4] Hongxing Xu, Erik Bjerneld, Mikael Käll, and Lars Börjesson. Spectroscopy of Single Hemoglobin Molecules by Surface Enhanced Raman Scattering. *Physical Review Letters*, 83(21):4357–4360, November 1999.

[5] Andrea Alù and Nader Engheta. Tuning the scattering response of optical nanoantennas with nanocircuit loads. *Nature Photonics*, 2(5):307–310, May 2008.

[6] Nader Engheta, Alessandro Salandrino, and Andrea Alù. Circuit Elements at Optical Frequencies: Nanoinductors, Nanocapacitors, and Nanoresistors. *Physical Review Letters*, 95(9):095504, August 2005.

[7] Andrea Alù and Nader Engheta. Input Impedance, Nanocircuit Loading, and Radiation Tuning of Optical Nanoantennas. *Physical Review Letters*, 101(4):043901, July 2008.

[8] M Schnell, A Garcia-Etxarri, A J Huber, K Crozier, J Aizpurua, and R Hillenbrand. Controlling the near-field oscillations of loaded plasmonic nanoantennas. *Time*, 3(April):287–291, 2009.

[9] A. C. Maxwell. *A Treatise on Electricity und Magnetism*. Number , A Treatise on Electricity und Magnetism. London, U.K.: Oxford Univ. Press, 1873, 1904. Oxford University Press, London, 1873.

[10] John David Jackson. *Classical Electrodynamics Third Edition*. Wiley, 1998.

[11] A. Garcia-Etxarri, R. Gomez-Medina, L. S. Froufe-Perez, C. Lopez, L. Chantada, F. Scheffold, J. Aizpurua, M. Nieto-Vesperinas, and J. J. Saenz. Strong magnetic response of submicron Silicon particles in the infrared. page 10, May 2010.

[12] S. Albaladejo, R. Gómez-Medina, L. S. Froufe-Pérez, H. Marinchio, R. Carminati, J. F. Torrado, G. Armelles, A. García-Martín, and J. J. Sáenz. Radiative corrections to the polarizability tensor of an electrically small anisotropic dielectric particle. *Optics Express*, 18(4):3556, February 2010.

[13] P. Nordlander, C. Oubre, E. Prodan, K. Li, and M. I. Stockman. Plasmon Hybridization in Nanoparticle Dimers. *Nano Letters*, 4(5):899–903, May 2004.

[14] Isabel Romero, Javier Aizpurua, Garnett W. Bryant, and F. Javier García De Abajo. Plasmons in nearly touching metallic nanoparticles: singular response in the limit of touching dimers. *Optics Express*, 14(21):9988, October 2006.

[15] Garnett W Bryant, F Javier García de Abajo, and Javier Aizpurua. Mapping the plasmon resonances of metallic nanoantennas. *Nano letters*, 8(2):631–6, February 2008.

[16] Edward D. Palik. *Handbook of optical constants of solids*. Academic press.

[17] Martin Moskovits. Surface-enhanced spectroscopy. *Reviews of Modern Physics*, 57(3):783–826, 1985.

[18] Frank Neubrech, Annemarie Pucci, Thomas Cornelius, Shafqat Karim, Aitzol García-Etxarri, and Javier Aizpurua. Resonant Plasmonic and Vibrational Coupling in a Tailored Nanoantenna for Infrared Detection. *Physical Review Letters*, 101(15):2–5, 2008.

[19] Surbhi Lal, Stephan Link, and Naomi J. Halas. Nano-optics from sensing to waveguiding. *Nature Photonics*, 1(11):641–648, November 2007.

[20] Javier Aizpurua, Thomas Taubner, F. Javier García de Abajo, Markus Brehm, and Rainer Hillenbrand. Substrate-enhanced infrared near-field spectroscopy. *Optics Express*, 16(3):1529, February 2008.

[21] Fritz Keilmann and Rainer Hillenbrand. Near-field microscopy by elastic light scattering from a tip. *Philosophical transactions. Series A, Mathematical, physical, and engineering sciences*, 362(1817):787–805, 2004.

[22] Elin M Larsson, Joan Alegret, Mikael Käll, and Duncan S Sutherland. Sensing characteristics of NIR localized surface plasmon resonances in gold nanorings for application as ultrasensitive biosensors. *Nano letters*, 7(5):1256–63, May 2007.

[23] A. Otto. Surface-enhanced Raman scattering of adsorbates. *Journal of Raman Spectroscopy*, 22(12):743–752, 1991.

[24] S. Nie and Steven R. Emory. Probing Single Molecules and Single Nanoparticles by Surface-Enhanced Raman Scattering. *Science*, 275(5303):1102–1106, 1997.

[25] Hui Wang, Janardan Kundu, and Naomi J Halas. Plasmonic nanoshell arrays combine surface-enhanced vibrational spectroscopies on a single substrate. *Angewandte Chemie (International ed. in English)*, 46(47):9040–4, 2007.

[26] D. Enders and A. Pucci. Surface enhanced infrared absorption of octadecanethiol on wet-chemically prepared Au nanoparticle films. *Applied Physics Letters*, 88(18):184104, 2006.

[27] Ricardo F. Aroca. *Surface-Enhanced Vibrational Spectroscopy*. ohn Wiley & Sons, Ltd., New York, 2006.

[28] Ricardo F. Aroca, Daniel J. Ross, and Concepción Domingo. Surface-Enhanced Infrared Spectroscopy. *Applied Spectroscopy*, 58(11):324A–338A, November 2004.

[29] Nikolay Goutev and Masayuki Futamata. Attenuated Total Reflection Surface-Enhanced Infrared Absorption Spectroscopy of Carboxyl Terminated Self-Assembled Monolayers on Gold. *Applied Spectroscopy*, 57(5):506–513, 2003.

[30] T. R. Jensen, R. P. Van Duyne, S. A. Johnson, and V. A. Maroni. Surface-Enhanced Infrared Spectroscopy: A Comparison of Metal Island Films with Discrete and Nondiscrete Surface Plasmons. *Applied Spectroscopy*, 54(3):371–377, 2000.

[31] Masatoshi Osawa and Masahiko Ikeda. Surface-enhanced infrared absorption of p-nitrobenzoic acid deposited on silver island films: contributions of electromagnetic and chemical mechanisms. *The Journal of Physical Chemistry*, 95(24):9914–9919, 1991.

[32] Masatoshi Osawa. *Near-Field Optics and Surface Plasmon Polaritons*, page 163187. Springer, 2001.

[33] F. Neubrech, T. Kolb, R. Lovrincic, G. Fahsold, A. Pucci, J. Aizpurua, T. W. Cornelius, M. E. Toimil-Molares, R. Neumann, and S. Karim. Resonances of individual metal nanowires in the infrared. *Applied Physics Letters*, 89(25):253104, 2006.

[34] P Mühlschlegel, H-J Eisler, O J F Martin, B Hecht, and D W Pohl. Resonant optical antennas. *Science (New York, N.Y.)*, 308(5728):1607–9, 2005.

[35] J. Aizpurua, Garnett Bryant, Lee Richter, F. García De Abajo, Brian Kelley, and T. Mallouk. Optical properties of coupled metallic nanorods for field-enhanced spectroscopy. *Physical Review B*, 71(23):235420, June 2005.

[36] Tim H Taminiau, Robert J Moerland, Frans B Segerink, Laurens Kuipers, and Niek F van Hulst. Lambda/4 resonance of an optical monopole antenna probed by single molecule fluorescence. *Nano letters*, 7(1):28–33, January 2007.

[37] F Schreiber. Structure and growth of self-assembling monolayers. *Progress in Surface Science*, 65(5-8):151–257, 2000.

[38] Eun K. Seo, Jung W. Lee, Hyung M. Sung-Suh, and Myung M. Sung. Atomic Layer Deposition of Titanium Oxide on Self-Assembled-Monolayer-Coated Gold. *Chemistry of Materials*, 16(10):1878–1883, May 2004.

[39] D. Lin-Vien, W. N. Colthup, W. G. Fateley, and J. G. Grasselli. *The Handbook of Infrared and Raman Frequencies of Organic Molecules*. John Wiley & Sons, Ltd., New York, 1991.

[40] F. García de Abajo and A. Howie. Relativistic Electron Energy Loss and Electron-Induced Photon Emission in Inhomogeneous Dielectrics. *Physical Review Letters*, 80(23):5180–5183, 1998.

[41] F. García de Abajo and A. Howie. Retarded field calculation of electron energy loss in inhomogeneous dielectrics. *Physical Review B*, 65(11), 2002.

[42] Scout. Scout - software package for optical spectroscopy, including dielectric function database, supplied by M. Theis Hard- and Software.

[43] Andreas Otto. The chemical (electronic) contribution to surface-enhanced Raman scattering. *Journal of Raman Spectroscopy*, 36(6-7):497–509, 2005.

[44] A Priebe, A Pucci, and A Otto. Infrared reflection-absorption spectra of C2H4 and C2H6 on Cu: effect of surface roughness. *The journal of physical chemistry. B*, 110(4):1673–9, February 2006.

[45] Amy E. Bjerke, Peter R. Griffiths, and Wolfgang Theiss. Surface-Enhanced Infrared Absorption of CO on Platinized Platinum. *Analytical Chemistry*, 71(10):1967–1974, May 1999.

[46] A. Priebe, M. Sinther, G. Fahsold, and A. Pucci. The correlation between film thickness and adsorbate line shape in surface enhanced infrared absorption. *The Journal of Chemical Physics*, 119(9):4887–4890, September 2003.

[47] U. Fano. Effects of Configuration Interaction on Intensities and Phase Shifts. *Physical Review*, 124(6):1866–1878, December 1961.

[48] S. Karim, M. E. Toimil-Molares, F. Maurer, G. Miehe, W. Ensinger, J. Liu, T. W. Cornelius, and R. Neumann. Synthesis of gold nanowires with controlled crystallographic characteristics. *Applied Physics A*, 84(4):403–407, 2006.

[49] H. Xu, J. Aizpurua, M. K\\"all, and P. Apell. Electromagnetic contributions to single-molecule sensitivity in surface-enhanced Raman scattering. *Physical Review E*, 62(3):43184324, 2000.

[50] Kuiru Li, Mark Stockman, and David Bergman. Self-Similar Chain of Metal Nanospheres as an Efficient Nanolens. *Physical Review Letters*, 91(22):1–4, 2003.

[51] Tomas Rindzevicius, Yury Alaverdyan, Andreas Dahlin, Fredrik Höök, Duncan S Sutherland, and Mikael Käll. Plasmonic sensing characteristics of single nanometric holes. *Nano letters*, 5(11):2335–9, November 2005.

[52] Alexandre Dmitriev, Carl Hägglund, Si Chen, Hans Fredriksson, Tavakol Pakizeh, Mikael Käll, and Duncan S Sutherland. Enhanced nanoplasmonic optical sensors with reduced substrate effect. *Nano letters*, 8(11):3893–8, November 2008.

[53] Craig F. Bohren and Donald R. Huffman. *Absorption and scattering of light by small particles*. Wiley, New York, 1983.

[54] Y. Kornyushin. Plasma oscillations in porous samples. *Science of Sintering*, 36(1):43–50, 2004.

[55] H. Xu, E.J. Bjerneld, J. Aizpurua, P. Apell, L. Gunnarsson, S. Petronis, B. Kasemo, C. Larsson, F. Hook, and M. Kall. Interparticle coupling effects in surface-enhanced Raman scattering. *Proc. SPIE*, 4258:3542, 2001.

[56] E Prodan, C Radloff, N J Halas, and P Nordlander. A hybridization model for the plasmon response of complex nanostructures. *Science (New York, N.Y.)*, 302(5644):419–22, October 2003.

[57] D.P. Fromm, A. Sundaramurthy, P.J. Schuck, G. Kino, and WE Moerner. Gap-dependent optical coupling of single bowtie nanoantennas resonant in the visible. *Nano letters*, 4(5):957961, 2004.

[58] J Aizpurua, S P Apell, and R Berndt. Role of tip shape in light emission from the scanning tunneling microscope. *Physical Review B*, 62(3):2065–2073, 2000.

[59] J Aizpurua, A Howie, and Abajo F J Garcia. Valence-electron energy loss near edges, truncated slabs, and junctions. *Physical Review B*, 60(15):149–162, 1999.

[60] C. Sönnichsen, T. Franzl, T. Wilk, G. von Plessen, J. Feldmann, O. Wilson, and P. Mulvaney. Drastic Reduction of Plasmon Damping in Gold Nanorods. *Physical Review Letters*, 88(7), 2002.

[61] Giorgio Volpe, Sudhir Cherukulappurath, Roser Juanola Parramon, Gabriel Molina-Terriza, and Romain Quidant. Controlling the optical near field of nanoantennas with spatial phase-shaped beams. *Nano letters*, 9(10):3608–11, October 2009.

[62] Petru Ghenuche, Sudhir Cherukulappurath, Tim Taminiau, Niek van Hulst, and Romain Quidant. Spectroscopic Mode Mapping of Resonant Plasmon Nanoantennas. *Physical Review Letters*, 101(11), September 2008.

[63] Jaysen Nelayah, Mathieu Kociak, Odile Stéphan, F. Javier García De Abajo, Marcel Tencé, Luc Henrard, Dario Taverna, Isabel Pastoriza-Santos, Luis M. Liz-Marzán, and Christian Colliex. Mapping surface plasmons on a single metallic nanoparticle. *Nature Physics*, 3(5):348–353, May 2007.

[64] Martin Aeschlimann, Michael Bauer, Daniela Bayer, Tobias Brixner, F Javier García De Abajo, Walter Pfeiffer, Martin Rohmer, Christian Spindler, and

Felix Steeb. Adaptive subwavelength control of nano-optical fields. *Nature*, 446(7133):301–4, March 2007.

[65] Mark Stockman, Sergey Faleev, and David Bergman. Coherent Control of Femtosecond Energy Localization in Nanosystems. *Physical Review Letters*, 88(6), 2002.

[66] T. H. Taminiau, F. D. Stefani, F. B. Segerink, and N. F. van Hulst. Optical antennas direct single-molecule emission. *Nature Photonics*, 2(4):234–237, April 2008.

[67] Atsushi Kubo, Ken Onda, Hrvoje Petek, Zhijun Sun, Yun S Jung, and Hong Koo Kim. Femtosecond imaging of surface plasmon dynamics in a nanostructured silver film. *Nano letters*, 5(6):1123–7, June 2005.

[68] R. Hillenbrand and F. Keilmann. Optical oscillation modes of plasmon particles observed in direct space by phase-contrast near-field microscopy. *Applied Physics B: Lasers and Optics*, 73(3):239–243, September 2001.

[69] R. Hillenbrand, F. Keilmann, P. Hanarp, D. S. Sutherland, and J. Aizpurua. Coherent imaging of nanoscale plasmon patterns with a carbon nanotube optical probe. *Applied Physics Letters*, 83(2):368, 2003.

[70] Zee Hwan Kim and Stephen R. Leone. Polarization-selective mapping of near-field intensity and phase around gold nanoparticles using apertureless near-field microscopy. *Optics Express*, 16(3):1733, February 2008.

[71] R. Hillenbrand and F. Keilmann. Complex Optical Constants on a Subwavelength Scale. *Physical Review Letters*, 85(14):3029–3032, 2000.

[72] Aitzol Garcia-Etxarri, Isabel Romero, F. Javier García De Abajo, Rainer Hillenbrand, and Javier Aizpurua. Influence of the tip in near-field imaging of nanoparticle plasmonic modes: Weak and strong coupling regimes. *Physical Review B*, 79(12):125439 – 125439–5, 2009.

[73] R Esteban, R Vogelgesang, J Dorfmüller, A Dmitriev, C Rockstuhl, C Etrich, and K Kern. Direct near-field optical imaging of higher order plasmonic resonances. *Nano letters*, 8(10):3155–9, October 2008.

[74] Jens Dorfmüller, Ralf Vogelgesang, R Thomas Weitz, Carsten Rockstuhl, Christoph Etrich, Thomas Pertsch, Falk Lederer, and Klaus Kern. Fabry-Pérot resonances in one-dimensional plasmonic nanostructures. *Nano letters*, 9(6):2372–7, June 2009.

[75] G. Raschke, S. Kowarik, T. Franzl, C. Sönnichsen, T. A. Klar, J. Feldmann, A. Nichtl, and K. Kürzinger. Biomolecular Recognition Based on Single Gold Nanoparticle Light Scattering. *Nano Letters*, 3(7):935–938, July 2003.

[76] Martin Schnell, Aitzol Garcia-Etxarri, Andreas J. Huber, Kenneth B. Crozier, Andrei Borisov, Javier Aizpurua, and Rainer Hillenbrand. Amplitude- and Phase-Resolved Near-Field Mapping of Infrared Antenna Modes by Transmission-Mode Scattering-Type Near-Field Microscopy . *The Journal of Physical Chemistry C*, page 100112102717070, January 2010.

[77] Lukas Novotny and B. Hecht. *Principles of Nano-optics*. Cambridge University Press, Cambridge, 2006.

[78] A. Koenderink, Maria Kafesaki, Ben Buchler, and Vahid Sandoghdar. Controlling the Resonance of a Photonic Crystal Microcavity by a Near-Field Probe. *Physical Review Letters*, 95(15), 2005.

[79] W. C. L. Hopman, K. O. van der Werf, A. J. F. Hollink, W. Bogaerts, V. Subramaniam, and R. M. de Ridder. Nano-mechanical tuning and imaging of a photonic crystal micro-cavity resonance. *Optics Express*, 14(19):8745, September 2006.

[80] M. Achermann, K. L. Shuford, G. C. Schatz, D. H. Dahanayaka, L. A. Bumm, and V. I. Klimov. Near-field spectroscopy of surface plasmons in flat gold nanoparticles. *Optics Letters*, 32(15):2254, August 2007.

[81] Francesca Intonti, Silvia Vignolini, Francesco Riboli, Anna Vinattieri, Diederik Wiersma, Marcello Colocci, Laurent Balet, Christelle Monat, Carl Zinoni, Lianhe Li, Romuald Houdré, Marco Francardi, Annamaria Gerardino, Andrea Fiore, and Massimo Gurioli. Spectral tuning and near-field imaging of photonic crystal microcavities. *Physical Review B*, 78(4), 2008.

[82] Robert D. Grober, Robert J. Schoelkopf, and Daniel E. Prober. Optical antenna: Towards a unity efficiency near-field optical probe. *Applied Physics Letters*, 70(11):1354, 1997.

[83] K. B. Crozier, A. Sundaramurthy, G. S. Kino, and C. F. Quate. Optical antennas: Resonators for local field enhancement. *Journal of Applied Physics*, 94(7):4632, 2003.

[84] P. Schuck, D. Fromm, A. Sundaramurthy, G. Kino, and W. Moerner. Improving the Mismatch between Light and Nanoscale Objects with Gold Bowtie Nanoantennas. *Physical Review Letters*, 94(1):017402, January 2005.

[85] Lukas Novotny. Effective Wavelength Scaling for Optical Antennas. *Physical Review Letters*, 98(26):266802, June 2007.

[86] Liang Tang, Sukru Ekin Kocabas, Salman Latif, Ali K. Okyay, Dany-Sebastien Ly-Gagnon, Krishna C. Saraswat, and David A. B. Miller. Nanometre-scale germanium photodetector enhanced by a near-infrared dipole antenna. *Nature Photonics*, 2(4):226–229, April 2008.

[87] Seungchul Kim, Jonghan Jin, Young-Jin Kim, In-Yong Park, Yunseok Kim, and Seung-Woo Kim. High-harmonic generation by resonant plasmon field enhancement. *Nature*, 453(7196):757–60, June 2008.

[88] Tolga Atay, Jung-Hoon Song, and Arto V. Nurmikko. Strongly Interacting Plasmon Nanoparticle Pairs: From DipoleDipole Interaction to Conductively Coupled Regime. *Nano Letters*, 4(9):1627–1631, September 2004.

[89] J Britt Lassiter, Javier Aizpurua, Luis I Hernandez, Daniel W Brandl, Isabel Romero, Surbhi Lal, Jason H Hafner, Peter Nordlander, and Naomi J Halas. Close encounters between two nanoshells. *Nano letters*, 8(4):1212–8, April 2008.

[90] Nenad Ocelic, Andreas Huber, and Rainer Hillenbrand. Pseudoheterodyne detection for background-free near-field spectroscopy. *Applied Physics Letters*, 89(10):101124, 2006.